



**Development of an Integrated BEM Approach
for Hot Fluid Structure Interaction**

Annual Report

November 1989 - November 1990

Grant # NAG3-712

Prepared by:

G.F. Dargush
P.K. Banerjee
Y. Shi

Department of Civil Engineering
State University of New York at Buffalo

Prepared for:

National Aeronautics and Space Administration
Lewis Research Center
21000 Brookpark Road
Cleveland, Ohio 44135

LIST OF CONTENTS

	Page
1. Introduction	1
2. Literature Review	4
3. Integral Formulation for Solids	6
3.1 Introduction	6
3.2 Governing Equations	6
3.3 Integral Representations	7
3.4 Numerical Implementation.....	8
3.5 Numerical Examples	21
3.6 Summary	23
4. Integral Formulation for Fluids	28
4.1 Introduction	28
4.2 Incompressible Thermoviscous Flow	28
4.2.1 Introduction	28
4.2.2 Governing Equations.....	29
4.2.3 Integral Representations.....	30
4.2.4 Numerical Implementation	32
4.2.5 Numerical Examples	42
4.2.6 Summary	50
4.3 Convective Incompressible Thermoviscous Flow.....	50
4.3.1 Introduction	50
4.3.2 Governing Equations.....	51
4.3.3 Fundamental Solutions.....	51
4.3.4 Integral Representations.....	53
4.3.5 Numerical Implementation	54
4.3.6 Numerical Examples	56
4.3.7 Summary	60
4.4 Convective Compressible Thermoviscous Flow	61
4.4.1 Introduction	61
4.4.2 Governing Equations	62
4.4.3 Fundamental Solutions.....	63
4.4.4 Integral Representations.....	64
4.4.5 Summary	65
5. Fluid-Structure Interaction	114
5.1 Introduction	114
5.2 Formulation	114
5.3 Numerical Implementation.....	116
5.4 Numerical Examples	116
6. BEM for Related Physical Phenomena	138

7. Summary	140
8. Future Direction	142

APPENDIX A - References	
APPENDIX B.1 - Kernels for Thermoelasticity	
APPENDIX B.2 - Kernels for Steady Incompressible Thermoviscous Flow	
APPENDIX B.3 - Kernels for Unsteady Incompressible Viscous Flow	
APPENDIX B.4 - Kernels for Steady Convective Incompressible Viscous Flow	
APPENDIX B.5 - Kernels for Steady Convective Compressible Thermoviscous Flow	

1. INTRODUCTION

As part of the continuing effort at NASA/Lewis to improve both the durability and reliability of hot section Earth-to-Orbit engine components, significant enhancements must be made in existing finite element and finite difference methods, and advanced techniques, such as the boundary element method, must be explored. Despite this considerable effort, the accurate determination of transient thermal stresses in these hot section components remains one of the most difficult problems facing engine design/analysts. For these problems, the temperature distribution is strongly influenced by the external hot gas flow, the internal cooling system, and the structural deformation. Currently, experimentally-determined film coefficients and ambient temperatures are required for use as boundary conditions for the thermal stress analysis of the structural component. The determination of these coefficients is obviously an expensive and time-consuming task. Recently an attempt was made by Gladden (1989) to use a finite difference-based Navier-Stokes code to approximate the thermal boundary conditions, and to then input these into a finite element structural analysis package. However, the most effective way to deal with this problem is to develop a completely integrated solid mechanics, fluid mechanics, and heat transfer approach.

In the present work, the boundary element method (BEM) is chosen as the basic analysis tool principally because the critical surface variables (i.e., temperature, flux, displacement, traction) can be very precisely determined with a boundary-based discretization scheme. Additionally, model preparation is considerably simplified compared to the more familiar domain-based methods. Furthermore, the hyperbolic character of high speed flow is captured through the use of an analytical fundamental solution, eliminating the dependence of the solution on the discretization pattern. The price that must be paid in order to realize these advantages is that any BEM formulation requires a considerable amount of analytical work, which is typically absent in the other numerical methods.

This report details all of the research accomplishments of a multi-year program, commencing in March 1986, aimed toward the development of a boundary element formulation for the study of hot fluid-structure interaction in Earth-to-Orbit engine hot section components. It should be noted that this work represents approximately four man-years of funding from NASA/Lewis. Most of that effort expended under this program has been directed toward the examination of fluid flow, since boundary element methods for fluids are at a much less developed state. Recently, however, significant strides have been made, not only in the analysis of thermoviscous fluids, but also in the solution of the fluid-structure interaction problem.

Early in the research program, a two-dimensional boundary element formulation was developed for the time-dependent response of a thermoelastic solid. This effort resulted in the first time domain, boundary-only implementation for this class of problems. Since volume discretization is completely eliminated and surface transient thermal stresses can be captured very accurately, the new approach provides distinct advantages over standard finite element methods.

Meanwhile, the initial fluid formulations that were developed, based upon Stokes fundamental solutions, provided solutions in the low-to-moderate Reynolds number range. For creeping flow, these reduce to boundary-only techniques. As the fluid velocities are increased, volume discretization is required, however the solutions are typically very precise, particularly in the determination of surface quantities. At very high speed, these formulations are less effective, because the Stokes fundamental solutions no longer embody the character of the flow field which becomes dominated by convection.

This led to the development of convective viscous integral formulations based upon Oseen fundamental solutions. Since the new convective kernel functions, that were developed as a part of this effort, contain more of the physics of the problem, boundary element solutions can now be obtained at very high Reynolds number. Flow around obstacles can be solved approximately with an efficient linearized boundary-only analysis or more exactly

by including all of the nonlinearities present in the neighborhood of the obstacle. This perhaps represents the major accomplishment of the present program.

The other significant development has been the creation of a comprehensive fluid-structure interaction capability within a boundary element computer code. This new facility is implemented in a completely general manner, so that quite arbitrary geometry, material properties and boundary conditions may be specified. Thus, a single analysis code can be used to run structures-only problems, fluids-only problems, or the combined fluid-structure problem. In all three cases, steady or transient conditions can be selected, with or without thermal effects. Nonlinear analyses can be solved via direct iteration or by employing a modified Newton-Raphson approach. However, it should be emphasized that the existing program is primarily a research code. Significant additional effort is needed to develop a practical engineering analysis tool.

In the next section, a brief review of the recent applicable boundary element literature is presented. This is followed by the development of integral formulations for the thermoelastic solid in Section 3 and for the thermoviscous fluid in Section 4. A number of detailed numerical examples are included at the end of these two sections to validate the formulations and to emphasize both the accuracy and generality of the implementation. Then, in Section 5, the fluid-structure interaction facility is discussed. Once again, several examples are provided to highlight this unique capability. It should be noted that all of the results presented in this report were run on a desktop SUN SPARCstation 1. Section 6 contains a collection of potential boundary element applications that have been uncovered as a result of work related to the present grant. For most of those problems, satisfactory analysis techniques do not currently exist. The remaining sections summarize the progress achieved to date, and specify the future direction. Tables and figures appear at the end of each section, while references are provided in Appendix A.

2. LITERATURE REVIEW

Very little has appeared in the literature on the analysis of coupled thermoviscous fluid-structure problems via the boundary element method. However, a number of publications have addressed the fluid and structure separately.

In general, the solid portion of the problem has been addressed to a much greater degree. For example, a boundary-only steady-state thermoelastic formulation was initially presented by Cruse et al (1977) and Rizzo and Shippy (1977). Recently, the present authors developed and implemented the quasistatic counterpart (Dargush, 1987; Dargush and Banerjee, 1989b, 1990a, 1990b), which is presented in detail in Section 3. Others, notably Sharp and Crouch (1986) and Chaudouet (1987), introduce volume integrals, to represent the equivalent thermal body forces. A similar domain based approach was taken earlier by Banerjee and Butterfield (1981) in the context of the analogous geomechanical problem.

An extensive review of the applications of integral formulations to viscous flow problems was included in a previous annual report (Dargush et al, 1987), and will not be repeated here. Interestingly, only a few groups of researchers are actively pursuing the further development of boundary elements for the analysis of viscous fluids. The work reported in Piva and Morino (1987) and Piva et al (1987) focuses heavily on the development of fundamental solutions and integral formulations with little emphasis on implementation. On the other hand, Tosaka and Kakuda (1986, 1987), Tosaka and Onishi (1986) have implemented single region boundary element formulations using approximate incompressible fundamental solutions. This latter group has developed sophisticated non-linear solution algorithms, and consequently, are able to demonstrate moderately high Reynolds number solutions. Meanwhile, Dargush and Banerjee (1991a, 1991b) present general purpose steady and time-dependent boundary element methods for moderate Reynolds number flows.

The most recent work from the above researchers has been collected into a volume entitled Developments in BEM - Volume 6: Nonlinear Problems of Fluid Dynamics, edited by Banerjee and Morino. Contributions from Wu and Wang, and Bush and Tanner are also included, along with two chapters from the present co-authors. The volume, published by Elsevier Applied Science Publishers became available in mid-1990, and provides a state-of-the-art review of boundary element fluid dynamics. However, it should be noted that the convective thermoviscous formulations of Section 4 are not included. These represent a significant further advancement which permit solutions for high Reynolds number flows. Interestingly, the basis for much of this latter development is actually work done early in this century by Oseen (1911, 1927).

For analysis of the interaction problem, a boundary element thermoelastic solid representation must be coupled with a suitable thermoviscous fluid formulation. Only Dargush and Banerjee (1988,1989a) have tackled this problem. These two papers provide a summary of the early work performed under this grant.

3. INTEGRAL FORMULATION FOR SOLIDS

3.1 Introduction

In the current section, a surface only time domain boundary element method (BEM) will be described for a thermoelastic body under quasistatic loading. Thus, transient heat conduction is included, but inertial effects are ignored. This BEM was first developed as part of the work performed during the second year (1987) of this grant. Since that time a number of improvements and extensions have been incorporated. During 1989, the algorithms for numerical integration have been made more efficient as well as more accurate, and a comprehensive PATRAN interface has been added to aid in the post-processing of the boundary element results. Additionally, a streamlined approach for uncoupled thermoelasticity was introduced (Dargush and Banerjee, 1989b). In 1990, boundary elements with a quartic variation of the field variables were implemented. These elements are particularly well suited for problems involving the bending of components (Deb and Banerjee, 1989).

Details of the integral formulation for 2D plane strain is presented below. (Problems of plane stress can be handled via a simple change in material parameters.) Separate subsections present the governing differential equations, the integral equations, an overview of the numerical implementation, and a couple of simple examples. Similar formulations have also been developed for three-dimensional (Dargush and Banerjee, 1990a) and axisymmetric problems (Dargush and Banerjee, 1990b).

3.2 Governing Equations

With the solid assumed to be a linear thermoelastic medium, the governing differential equations for transient thermoelasticity can be written

$$(\lambda + \mu) \frac{\partial^2 u_j}{\partial x_i \partial x_j} + \mu \frac{\partial^2 u_i}{\partial x_j \partial x_j} - (3\lambda + 2\mu)\alpha \frac{\partial \theta}{\partial x_i} = 0 \quad (3.1a)$$

$$\rho c_e \frac{\partial \theta}{\partial t} = k \frac{\partial^2 \theta}{\partial x_j \partial x_j} \quad (3.1b)$$

where

u_i displacement vector

θ temperature

t time

x_i Lagrangian coordinate

k thermal conductivity

ρ mass density

c_e specific heat at constant deformation

λ, μ Lamé constants

α coefficient of thermal expansion

Standard indicial notation has been employed with summations indicated by repeated indices. For two-dimensional problems considered herein, the Latin indices i and j vary from one to two.

Note that (3.1b) is the energy equation and that (3.1a) represents the momentum balance in terms of displacements and temperature. The theory portrayed by the above set of equations, formally labeled uncoupled quasistatic thermoelasticity, can be derived from thermodynamic principles. (See Boley and Weiner (1960) for details.) In developing (3.1), the dynamics effects of interia have been ignored.

3.3 Integral Representations

Utilizing equation (3.1) for the solid along with a generalized form of the reciprocal theorem, permits one to develop the following boundary integral equation:

$$c_{\beta\alpha}(\xi)u_\beta(\xi, t) = \int_S [g_{\beta\alpha} * t_\beta(X, t) - f_{\beta\alpha} * u_\beta(X, t)] dS(X). \quad (3.2)$$

where

α, β indices varying from 1 to 3

s surface of solid

u_α, t_α generalized displacement and traction

$$u_\alpha = [u_1 \ u_2 \ \theta]^T$$

$$t_\alpha = [t_1 \ t_2 \ q]^T$$

θ, q temperature, heat flux

$g_{\alpha\beta}, f_{\alpha\beta}$ generalized displacement and traction kernels

$c_{\alpha\beta}$ constants determined by the relative smoothness of s at ξ

and, for example

$$g_{\alpha\beta} * t_\alpha = \int_0^t g_{\alpha\beta}(x, t; \xi, \tau) t_\alpha(x, \tau) d\tau$$

denotes a Riemann convolution integral. The kernel functions $g_{\alpha\beta}$ and $f_{\alpha\beta}$ are derived from the fundamental infinite space solutions of (3.1).

In principle, at each instant of time progressing from time zero, this equation can be written at every point on the boundary. The collection of the resulting equations could then be solved simultaneously, producing exact values for all the unknown boundary quantities. In reality, of course, discretization is needed to limit this process to a finite number of equations and unknowns. Techniques useful for the discretization of (3.2) are the subject of the following section.

3.4 Numerical Implementation

3.4.1 Introduction

The boundary integral equation (3.2), developed in the last section, is an exact statement. No approximations have been introduced other than those used to formulate the boundary value problem. However, in order to apply (3.2) for the solution of practical engineering problems, approximations are required in both time and space. In this section, an overview of a general-purpose, state-of-the-art numerical implementation is presented. Many of the features and techniques to be discussed, in this section, were developed previously for elastostatics (e.g., Banerjee et al, 1985, 1988), and elastodynamics (e.g., Banerjee et al, 1986; Ahmad and Banerjee, 1988), but are here adapted for thermoelastic analysis.

3.4.2 Temporal Discretization

Consider, first, the time integrals represented in (3.2) as convolutions. Clearly, without any loss of precision, the time interval from zero to t can be divided into N equal increments of duration Δt .

By assuming that the primary field variables, t_β and u_β , are constant within each Δt time increment, these quantities can be brought outside of the time integral. That is,

$$g_{\beta\alpha} * t_\beta(X, t) = \sum_{n=1}^N t_\beta^n(X) \int_{(n-1)\Delta t}^{n\Delta t} g_{\beta\alpha}(X - \xi, t - \tau) d\tau \quad (3.3a)$$

$$f_{\beta\alpha} * u_\beta(X, t) = \sum_{n=1}^N u_\beta^n(X) \int_{(n-1)\Delta t}^{n\Delta t} f_{\beta\alpha}(X - \xi, t - \tau) d\tau \quad (3.3b)$$

where the superscript on the generalized tractions and displacements, obviously, represents the time increment number. Notice, also, that, within an increment, these primary field variables are now functions of position only. Next, since the integrands remaining in (3.3) are known in explicit form from the fundamental solutions, the required temporal integration can be performed analytically, and written as

$$G_{\beta\alpha}^{N+1-n}(X - \xi) = \int_{(n-1)\Delta t}^{n\Delta t} g_{\beta\alpha}(X - \xi, t - \tau) d\tau \quad (3.4a)$$

$$F_{\beta\alpha}^{N+1-n}(X - \xi) = \int_{(n-1)\Delta t}^{n\Delta t} f_{\beta\alpha}(X - \xi, t - \tau) d\tau. \quad (3.4b)$$

These kernel functions, $G_{\beta\alpha}^n(X - \xi)$ and $F_{\beta\alpha}^n(X - \xi)$, are detailed in Appendix B.1. Combining (3.3) and (3.4) with (3.2) produces

$$c_{\beta\alpha}(\xi) u_\beta^N(\xi) = \sum_{n=1}^N \int_S \left[G_{\beta\alpha}^{N+1-n}(X - \xi) t_\beta^n(X) - F_{\beta\alpha}^{N+1-n}(X - \xi) u_\beta^n(X) \right] dS(X), \quad (3.5)$$

which is the boundary integral statement after the application of the temporal discretization.

3.4.3 Spatial Discretization

With the use of generalized primary variables and the incorporation of a piecewise constant time stepping algorithm, the boundary integral equation (3.5) begins to show a strong resemblance to that of elastostatics, particularly for the initial time step (i.e., $N = 1$). In this subsection, those similarities will be exploited to develop the spatial discretization for the uncoupled quasistatic problem with two-dimensional geometry. This approximate spatial representation will, subsequently, permit numerical evaluation of the surface integrals appearing in (3.5). The techniques described here, actually, originated in the finite element literature, but were later applied to boundary elements by Lachat and Watson (1976).

The process begins by subdividing the entire surface of the body into individual elements of relatively simple shape. The geometry of each element is, then, completely defined by the coordinates of the nodal points and associated interpolation functions. That is,

$$X(\zeta) = \mathbf{x}_i(\zeta) = N_w(\zeta) \mathbf{x}_{iw} \quad (3.6)$$

with

ζ intrinsic coordinates

N_w shape functions

\mathbf{x}_{iw} nodal coordinates

and where w is an integer varying from one to W , the number of geometric nodes in the element. Next, the same type of representation is used, within the element, to describe the primary variables. Thus,

$$u_\alpha^n(\zeta) = N_w(\zeta) u_{\alpha w}^n \quad (3.7a)$$

$$t_\alpha^n(\zeta) = N_w(\zeta) t_{\alpha w}^n \quad (3.7b)$$

in which $u_{\alpha w}^n$ and $t_{\alpha w}^n$ are the nodal values of the generalized displacement and tractions, respectively, for time step n . Also, in (3.7), the integer w varies from one to Ω , the total

number of functional nodes in the element. From the above, note that the same number of nodes, and consequently shape functions, are not necessarily used to describe both the geometric and functional variations. Specifically, in the present work, the geometry is exclusively defined by quadratic shape functions. In two-dimensions, this requires the use of three-noded line elements. On the other hand, the variation of the primary quantities can be described, within an element, by linear, quadratic or quartic shape functions. For each quartic element, two additional quarter-point nodes are automatically generated by the program. It should be noted that the introduction of quartic elements this past year, also provides the foundation for the development of a p -adaptive boundary element capability.

Once the spatial discretization has been accomplished and the body has been subdivided into M elements, the boundary integral equation can be rewritten as

$$c_{\beta\alpha}(\xi)u_{\beta}^N(\xi) = \sum_{n=1}^N \left\{ \sum_{m=1}^M \int_{S_m} \left[G_{\beta\alpha}^{N+1-n}(X(\zeta) - \xi)N_{\omega}(\zeta)t_{\beta\omega}^n - F_{\beta\alpha}^{N+1-n}(X(\zeta) - \xi)N_{\omega}(\xi)u_{\beta\omega}^n \right] dS(X(\zeta)) \right\} \quad (3.8)$$

where

$$S = \sum_{m=1}^M S_m.$$

In the above equation, $t_{\beta\omega}^n$ and $u_{\beta\omega}^n$ are nodal quantities which can be brought outside the surface integrals. Thus,

$$c_{\beta\alpha}(\xi)u_{\beta}^N(\xi) = \sum_{n=1}^N \left\{ \sum_{m=1}^M t_{\beta\omega}^n \int_{S_m} G_{\beta\alpha}^{N+1-n}(X(\zeta) - \xi)N_{\omega}(\zeta)dS(X(\zeta)) - u_{\beta\omega}^n \int_{S_m} F_{\beta\alpha}^{N+1-n}(X(\zeta) - \xi)N_{\omega}(\zeta)dS(X(\zeta)) \right\} \quad (3.9)$$

The positioning of the nodal primary variables outside the integrals is, of course, a key step since now the integrands contain only known functions. However, before discussing the techniques used to numerically evaluate these integrals, a brief discussion of the singularities present in the kernels $G_{\beta\alpha}^n$ and $F_{\beta\alpha}^n$ is in order.

The fundamental solutions to the uncoupled quasistatic problem contain singularities when the load point and field point coincide, that is, when $r = 0$. The same is true of $G_{\beta\alpha}^n$

and $F_{\beta\alpha}^n$, since these kernels are derived directly from the fundamental solutions. Series expansions of terms present in the evolution functions can be used to deduce the level of singularities existing in the kernels.

A number of observations concerning the results of these expansions should be mentioned. First, as would be expected $F_{\alpha\beta}^1$ has a stronger level of singularity than does the corresponding $G_{\alpha\beta}^1$, since an additional derivative is involved in obtaining $F_{\alpha\beta}^1$ from $G_{\alpha\beta}^1$. Second, the coupling terms do not have as a high degree of singularity as do the corresponding non-coupling terms. Third, all of the kernel functions for the first time step could actually be rewritten as a sum of steady-state and transient components. That is,

$$G_{\alpha\beta}^1 = ^{ss}G_{\alpha\beta} + ^{tr}G_{\alpha\beta}^1$$

$$F_{\alpha\beta}^1 = ^{ss}F_{\alpha\beta} + ^{tr}F_{\alpha\beta}^1.$$

Then, the singularity is completely contained in the steady-state portion. Furthermore, the singularity in G_{ij}^1 and F_{ij}^1 is precisely equal to that for elastostatics, while $G_{\theta\theta}^1$ and $F_{\theta\theta}^1$ singularities are identical to those for potential flow. (For two-dimensions, the subscript θ equals three.) This observation is critical in the numerical integration of the $F_{\alpha\beta}$ kernel to be discussed in the next subsection. However, from a physical standpoint, this means that, at any time t , the nearer one moves toward the load point, the closer the quasistatic response field corresponds with a steady-state field. Eventually, when the sampling and load points coincide, the quasistatic and steady-state responses are indistinguishable. As a final item, after careful examination of Appendix B.1, it is evident that the steady-state components in the kernels $G_{\alpha\beta}^n$ and $F_{\alpha\beta}^n$, with $n > 1$, vanish. In that case, all that remains is a transient portion that contains no singularities. Thus, all singularities reside in the $^{ss}G_{\alpha\beta}$ and $^{ss}F_{\alpha\beta}$ components of $G_{\alpha\beta}^1$ and $F_{\alpha\beta}^1$, respectively.

3.4.4 Numerical Integration

Having clarified the potential singularities present in the coupled kernels, it is now possible to consider the evaluation of the integrals in equation (3.9). That is, for any

element m , the integrals

$$\int_{S_m} G^{N+1-n}(X(\zeta) - \xi) N_\omega(\zeta) dS(X(\zeta)) \quad (3.10a)$$

$$\int_{S_m} F^{N+1-n}(X(\zeta) - \xi) N_\omega(\zeta) dS(X(\zeta)) \quad (3.10b)$$

will be examined. To assist in this endeavor, the following three distinct categories can be identified.

- (1) The point ξ does not lie on the element m .
- (2) The point ξ lies on the element m , but only non-singular or weakly singular integrals are involved.
- (3) The point ξ lies on the element m , and the integral is strongly singular.

In practical problems involving many elements, it is evident that most of the integration occurring in equation (3.9) will be of the category (1) variety. In this case, the integrand is always non-singular, and standard Gaussian quadrature formulas can be employed. Sophisticated error control routines are needed, however, to minimize the computational effort for a certain level of accuracy. This non-singular integration is the most expensive part of a boundary element analysis, and, consequently, must be optimized to achieve an efficient solution. In the present implementation, error estimates, based upon the work of Stroud and Secrest (1966), are employed to automatically select the proper order of the quadrature rule. Additionally, to improve accuracy in a cost-effective manner, a graded subdivision of the element is incorporated, especially when ξ is nearby. For two-dimensional problems, the integration order varies from two to twelve, within each of up to four element subdivisions.

Turning next to category (2), one finds that again Gaussian quadrature is applicable, however, a somewhat modified scheme must be utilized to evaluate the weakly singular integrals. This is accomplished in two-dimensional elements via suitable subsegmentation along the length of the element so that the product of shape function, Jacobian and kernel remains well behaved.

Unfortunately, the remaining strongly singular integrals of category (3) exist only in the Cauchy principal value sense and cannot, in general, be evaluated numerically, with sufficient precision. It should be noted that this apparent stumbling block is limited to the strongly singular portions, $^{ss}F_{ij}$ and $^{ss}F_{\theta\theta}$, of the $F_{\alpha\beta}^1$ kernel. The remainder of $F_{\alpha\beta}^1$, including $^{tr}F_{ij}^1$ and $^{tr}F_{\theta\theta}^1$, can be computed using the procedures outlined for category (2). However, as will be discussed in the next subsection, even category (3) $^{ss}F_{ij}$ and $^{ss}F_{\theta\theta}$ kernels can be accurately determined by employing an indirect ‘rigid body’ method originally developed by Cruse (1974).

3.4.5 Assembly

The complete discretization of the boundary integral equation, in both time and space, has been described, along with the techniques required for numerical integration of the kernels. Now, a system of algebraic equations can be developed to permit the approximate solution of the original quasistatic problem. This is accomplished by systematically writing (3.9) at each global boundary node. The ensuing nodal collocation process, then, produces a global set of equations of the form

$$\sum_{n=1}^N \left(\left[G^{N+1-n} \right] \{t^n\} - \left[F^{N+1-n} \right] \{u^n\} \right) = \{0\}, \quad (3.11)$$

where

$[G^{N+1-n}]$ unassembled matrix of size $(d+1)P \times (d+1)Q$, with coefficients determined from (3.10a)

$[F^{N+1-n}]$ assembled matrix of size $(d+1)P \times (d+1)P$, with coefficients determined from (3.10b) and $c_{\beta\alpha}$ included in the diagonal blocks

$\{t^n\}$ global generalized nodal traction vector with $(d+1)Q$ components

$\{u^n\}$ global generalized nodal displacement vector with $(d+1)P$ components

$\{0\}$ null vector with $(d+1)P$ components

P total number of global functional nodes

$$Q = \sum_{m=1}^M A_m$$

A_m number of functional nodes in element m

d dimensionality of the problem.

In the above, recall that the terms generalized displacement and traction refer to the inclusion of the temperature and flux, respectively, as the $(d+1)$ component at any point.

Consider, now, the first step. Thus, for $N = 1$, equation (3.11) becomes

$$[G^1]\{t^1\} - [F^1]\{u^1\} = \{0\}. \quad (3.12)$$

However, at this point the diagonal block of $[F^1]$ has not been completely determined due to the strongly singular nature of $^{ss}F_{ij}$ and $^{ss}F_{\theta\theta}$. Following Cruse (1974) and, later, Banerjee et al (1986) in elastodynamics, these diagonal contributions can be calculated indirectly by imposing a uniform ‘rigid body’ generalized displacement field on the same body, but under steady-state conditions. Then, obviously, the generalized tractions must be zero, and

$$[^{ss}F]\{1\} = \{0\}, \quad (3.13)$$

where $\{1\}$ is a vector symbolizing a unit uniform motion. Using (3.13), the desired diagonal blocks, $^{ss}F_{ij}$ and $^{ss}F_{\theta\theta}$, can be obtained from the summation of the off-diagonal terms of $[^{ss}F]$. The remaining transient portion of the diagonal block is non-singular, and hence can be evaluated to any desired precision. After summing the steady-state and transient contributions, (3.12) is once again written as

$$[G^1]\{t^1\} - [F^1]\{u^1\} = \{0\}, \quad (3.14)$$

but now the evaluation of $[F^1]$ is complete.

In a well-posed problem, at time Δt , the set of global generalized nodal displacements and tractions will contain exactly $(d+1)P$ unknown components. Then, as the final stage in the assembly process, equation (3.14) can be rearranged to form

$$[A^1]\{x^1\} = [B^1]\{y^1\}, \quad (3.15)$$

in which

$\{x^1\}$ unknown components of $\{u^1\}$ and $\{t^1\}$

$\{y^1\}$ known components of $\{u^1\}$ and $\{t^1\}$

$[A^1], [B^1]$ associated matrices

3.4.6 Solution

To obtain a solution of (3.15) for the unknown nodal quantities, a decomposition of matrix $[A^1]$ is required. In general, $[A^1]$ is a densely populated, unsymmetric matrix. The out-of-core solver, utilized here, was developed originally for elastostatics from the LINPACK software package (Dongarra et al, 1979) and operates on a submatrix level. Within each submatrix, Gaussian elimination with single pivoting reduces the block to upper triangular form. The final decomposed form of $[A^1]$ is stored in a direct-access file for reuse in subsequent time steps. Backsubstitution then completes the determination of $\{x^1\}$. Additional information on this solver is available in Banerjee et al (1985).

After turning from the solver routines, the entire nodal response vectors, $\{u^1\}$ and $\{t^1\}$, at time Δt are known. For solutions at later times, a simple marching algorithm is employed. Thus, from (3.11) with $N = 2$,

$$[G^1]\{t^1\} - [F^1]\{u^1\} + [G^1]\{t^2\} - [F^1]\{u^2\} = \{0\}. \quad (3.16)$$

Assuming that the same set of nodal components are unknown as in (3.14) for the first time step, equation (3.16) is reformulated as

$$[A^1]\{x^2\} = [B^1]\{y^2\} - [G^2]\{t^1\} + [F^2]\{u^1\}. \quad (3.17)$$

Since, at this point, the right-hand side contains only known quantities, (3.17) can be solved for $\{x^2\}$. However, the decomposed form of $[A^1]$ already exists on a direct-access file, so only the relatively inexpensive backsubstitution phase is required for the solution.

The generalization of (3.17) to any time step N is simply

$$[A^1]\{x^N\} = [B^1]\{y^N\} - \sum_{n=1}^{N-1} \left([G^{N+1-n}]\{t^n\} - [F^{N+1-n}]\{u^n\} \right) \quad (3.18)$$

in which the summation represents the effect of past events. By systematically storing all of the matrices and nodal response vectors computed during the marching process, surprisingly little computing time is required at each new time step. In fact, for any time step beyond the first, the only major computational task is the integration needed to form $[G^N]$ and $[F^N]$. Even this process is somewhat simplified, since now the kernels are non-singular. As a result, reduced subsegmentation and gaussian integration order is appropriate. Also, as time marches on, the effect of events that occurred during the first time step diminishes. Consequently, the terms containing $[G^N]$ and $[F^N]$ will eventually become insignificant compared to those associated with recent events. Once that point is reached, further integration is unnecessary, and a significant reduction in the computing effort per time step can be achieved.

It should be emphasized that the entire boundary element method developed, in this section, has involved surface quantities exclusively. A complete solution to the well-posed linear uncoupled quasistatic problem, with homogeneous properties, can be obtained in terms of the nodal response vectors, without the need for any volume discretization. In many practical situations, however, additional information, such as, the temperature at interior locations or the stress at points on the boundary, is required. The next subsection discusses the calculations of these quantities.

3.4.7 Interior Quantities

Once equation (3.18) is solved, at any time step, the complete set of primary nodal quantities, $\{u^n\}$ and $\{t^n\}$, is known. Subsequently, the response at points within the body can be calculated in a straightforward manner. For any point ξ in the interior, the generalized displacement can be determined from (3.9) with $c_{\beta\alpha} = \delta_{\beta\alpha}$. That is,

$$u_\alpha^n(\xi) = \sum_{n=1}^N \left\{ \sum_{m=1}^M \left[t_{\beta\omega}^n \int_{S_m} G_{\beta\alpha}^{N+1-n}(X(\zeta) - \xi) N_\omega(\zeta) dS(X(\zeta)) \right. \right. \\ \left. \left. - u_{\beta\omega}^n \int_{S_m} F_{\beta\alpha}^{N+1-n}(X(\zeta) - \xi) N_\omega(\zeta) dS(X(\zeta)) \right] \right\}. \quad (3.19)$$

Now, all the nodal variables on the right-hand side are known, and, as long as, ξ is not on

the boundary, the kernel functions in (3.19) remain non-singular. However, when ξ is on the boundary, the strong singularity in ${}^{ss}F_{\beta\alpha}$ prohibits accurate evaluation of the generalized displacement via (3.19), and an alternate approach is required. The apparent dilemma is easily resolved by recalling that the variation of surface quantities is completely defined by the elemental shape functions. Thus, for boundary points, the desired relationship is simply

$$u_{\alpha}^N(\xi) = N_{\omega}(\zeta)u_{\alpha\omega}^N \quad (3.20)$$

where $N_{\omega}(\zeta)$ are the shape functions for the appropriate element and ζ are the intrinsic coordinates corresponding to ξ within that element. Obviously, from (3.20), neither integration nor the explicit contribution of past events are needed to evaluate generalized boundary displacements.

In many problems, additional quantities, such as heat flux and stress, are also important. The boundary integral equation for heat flux, can be written

$$q_i^N(\xi) = \sum_{n=1}^N \left\{ \sum_{m=1}^M \left[t_{\beta\omega}^n \int_{S_m} E_{\beta\theta i}^{N+1-n}(X(\zeta) - \xi) N_{\omega}(\zeta) dS(X(\zeta)) \right. \right. \\ \left. \left. - u_{\beta\omega}^n \int_{S_m} D_{\beta\theta i}^{N+1-n}(X(\zeta) - \xi) N_{\omega}(\zeta) dS(X(\zeta)) \right] \right\}. \quad (3.21)$$

where

$$E_{\beta\theta i}^n(X(\zeta) - \xi) = -k \frac{\partial G_{\beta\theta}^n(X(\zeta) - \xi)}{\partial \xi_i} \quad (3.21a)$$

$$D_{\beta\theta i}^n(X(\zeta) - \xi) = -k \frac{\partial F_{\beta\theta}^n(X(\zeta) - \xi)}{\partial \xi_i} \quad (3.21b)$$

This is valid for interior points, whereas, when ξ is on the boundary, the shape functions can again be used. In this latter case,

$$N_{\omega}(\zeta)q_i^N = n_i(\xi)q_i^N(\xi) \quad (3.22a)$$

$$\frac{\partial N_{\omega}(\zeta)}{\partial \zeta} \theta_{\omega}^N = -\frac{1}{k} \frac{\partial x_i}{\partial \zeta} q_i^N(\xi), \quad (3.22b)$$

which can be solved for boundary flux. Meanwhile, interior stresses can be evaluated from

$$\sigma_{ij}^N(\xi) = \sum_{n=1}^N \left\{ \sum_{m=1}^M \left[t_{\beta\omega}^n \int_{S_m} E_{\beta ij}^{N+1-n}(X(\zeta) - \xi) N_{\omega}(\zeta) dS(X(\zeta)) \right. \right. \\ \left. \left. - u_{\beta\omega}^n \int_{S_m} D_{\beta ij}^{N+1-n}(X(\zeta) - \xi) N_{\omega}(\zeta) dS(X(\zeta)) \right] \right\} \quad (3.23)$$

in which

$$E_{\beta ij}^n(X(\zeta) - \xi) = \frac{2\mu\nu}{1-2\nu} \delta_{ij} \frac{\partial G_{\beta\ell}^n}{\partial \xi_\ell} + \mu \left(\frac{\partial G_{\beta i}^N}{\partial \xi_j} + \frac{\partial G_{\beta j}^N}{\partial \xi_i} \right) - \beta \delta_{ij} G_{\beta\theta}^n \quad (3.23a)$$

$$D_{\beta ij}^n(X(\zeta) - \xi) = \frac{2\mu\nu}{1-2\nu} \delta_{ij} \frac{\partial F_{\beta\ell}^n}{\partial \xi_\ell} + \mu \left(\frac{\partial F_{\beta i}^N}{\partial \xi_j} + \frac{\partial F_{\beta j}^N}{\partial \xi_i} \right) - \beta \delta_{ij} F_{\beta\theta}^n, \quad (3.23b)$$

with ν representing the Poisson ratio and $\beta = (3\lambda + 2\mu)\alpha$. Equation (3.23) is, of course, developed from (3.19). Since strong kernel singularities appear when (3.23) is written for boundary points, once again an alternate procedure is needed to determine surface stress. This alternate scheme exploits the interrelationships between generalized displacement, traction, and stress and is the straightforward extension of the technique typically used in elastostatic implementation (Cruse and Van Buren, 1971). Specifically, the following can be obtained

$$n_j(\xi) \sigma_{ij}^N(\xi) = N_\omega(\zeta) t_{i\omega}^N \quad (3.24a)$$

$$\sigma_{ij}^N(\xi) - \frac{D_{ijkl}^e}{2} \left(u_{k,l}^N(\xi) + u_{l,k}^N(\xi) \right) = -\beta \delta_{ij} N_\omega(\zeta) u_{\theta\omega}^N \quad (3.24b)$$

$$\frac{\partial x_j}{\partial \zeta} u_{i,j}^N(\xi) = \frac{\partial N_\omega}{\partial \zeta} u_{i\omega}^N \quad (3.24c)$$

in which $u_{\theta\omega}^N$ is obviously the nodal temperatures, and,

$$D_{ijkl}^e = \lambda \delta_{ij} \delta_{kl} + 2\mu \delta_{ik} \delta_{jl}.$$

Equations (3.24) form an independent set that can be solved numerically for $\sigma_{ij}^N(\xi)$ and $u_{i,j}^N(\xi)$ completely in terms of known nodal quantities $u_{\alpha\omega}^N$ and $t_{\alpha\omega}^N$, without the need for kernel integration nor convolution. Notice, however, that shape function derivatives appear in (3.24c), thus constraining the representation of stress on the surface element to something less than full quadratic variation. The interior stress kernel functions, defined by (3.23), are also detailed in Appendix B.1.

3.4.8 Advanced Features

The thermoelastic formulation has been implemented as a segment of the state-of-the-art, general purpose boundary element computer program, GP-BEST. Consequently, many

additional features, beyond those detailed above, are available for the analysis of complex engineering problems. Perhaps, the most significant of these items, is the capability to analyze substructured problems. This, not only extends the analysis to bodies composed of several different materials, but also often provides computational efficiencies. An individual substructure or geometric modeling region (GMR) must contain a single material. During the integration process, each GMR remains a separate entity. The GMR's are then brought together at the assembly stage, where compatibility relationships are enforced on common boundaries between regions. Typically, compatibility ensures continuous displacement and temperature fields across an interface, however, recent enhancements to the code permit sliding between regions, spring contacts and interfacial thermal resistance to model air gaps or coating resistances. In the latter instances, discontinuities appear at the interface. In any case, the multi-GMR assembly process produces block-banded system matrices that are solved in an efficient manner.

As another feature, a high degree of flexibility is provided for the specification of boundary conditions. In general, time-dependent values can be defined in either global or local coordinates. Not only can generalized displacements and tractions be specified, but also spring and convection boundary conditions are available. Another recent addition permits time-dependent ambient temperatures. A final item, worthy of note, is the availability of a comprehensive symmetry capability which includes provisions for both planar and cyclic symmetry.

During the past two years, an interface to the well-known PATRAN graphics package was developed and enhanced. This interface allows the user an option to view deformed shapes, temperatures and stress boundary profiles or contours. A number of PATRAN-produced illustrations are included throughout this report. In the next section, a couple of examples are presented to demonstrate the validity and applicability of this boundary-only formulation.

3.5 Numerical Examples

3.5.1 Sudden Heating of Aluminum Block

As a first example, transient heating of an aluminum block is examined under plane strain conditions. The block, shown in Figure 3.1, initially rests in thermodynamic equilibrium at zero temperature. Then, suddenly, the face at $Y = 1.0$ in. is elevated to 100°F , while the remaining three faces are insulated and restrained against normal displacements. Thus, only axial deformation in the Y -direction is permitted. Naturally, as the diffusive process progresses, temperature builds along with the lateral stresses σ_{xx} and σ_{zz} . To complete the specification of the problem, the following standard set of material properties are used to characterize the aluminum:

$$E = 10 \times 10^6 \text{ psi}, \quad \nu = 0.33,$$

$$\alpha = 13 \times 10^{-6}/^{\circ}\text{F},$$

$$k = 25 \text{ in.lb./sec.in.}^{\circ}\text{F}, \quad \rho c_e = 200 \text{ in.lb./in.}^3\text{F.}$$

The two-dimensional boundary element idealization consists of the simple four element, eight node model included in Figure 3.1. A time step of 0.4 sec. is selected, corresponding to a non-dimensional time step of 0.5. Additionally, a finite element analysis of this same problem was conducted using a modified thermal version of the computer code CRISP (Gunn and Britto, 1984). The finite element model is also a two-dimensional plane strain representation, however, sixteen linear strain quadrilaterals are placed along the diffusion length. In the FE run, a time step of 0.2 sec. is employed.

Temperatures, displacements, and stresses are compared in Table 3.1. Notice that the boundary element analysis, with only one element in the flow direction, produces a better time-temperature history than does a sixteen element FE analysis with a smaller time step. Both methods exhibit greatest error during the initial stages of the process. This is the result of the imposition of a sudden temperature change. Meanwhile, the comparison of the overall axial displacement indicates agreement to within 3% for the BE analysis and 5% for the FE run. A steady-state analysis via both methods produces the exact

answer to three digit accuracy. The last comparison, in the table, involves lateral stresses at an integration point in the FE model. The boundary element results are quite good throughout the range, however, the FE stresses exhibit considerable error, particularly during the initial four seconds. Actually, these finite element stress variations are not unexpected in light of the errors present in the temperature and displacement response. Recall that in the standard finite element process, stresses are computed on the basis of numerical differentiation of the displacements, whereas in boundary elements, the stresses at interior points are obtained directly from a discretized version of an exact integral equation. Consequently, the BE interior stress solution more nearly coincides with the actual response.

3.5.2 Circular Disc

Next, transient thermal stresses in a circular disc are investigated. The disc of radius ' a ' initially rests at zero uniform temperature. The top and bottom surfaces are thermally insulated, and all boundaries are completely free of mechanical constraint. Then, suddenly, at time zero, the temperature of the entire outer edge (i.e., $r = a$) is elevated to unity and, subsequently, maintained at that level.

The boundary element model of the disc with unit radius is shown in Figure 3.2. Only four quadratic elements are employed, along with quarter symmetry. Ten interior points are also included strictly to monitor response. In addition, the following non-dimensionalized material properties are arbitrarily selected for the plane stress analysis:

$$E = 1.333 \quad \rho c_e = 1.0$$

$$\nu = 0.333 \quad k = 1.0$$

$$\alpha = 0.75$$

Results obtained under quasistatic conditions for a time step of 0.005 are compared, in Figures 3.3, 3.4 and 3.5, to the analytical solution presented in Timoshenko and Goodier (1970). Notice that temperatures, as well as radial and tangential stresses are accurately determined via the boundary element analysis. In particular from Figure 3.5, even the

tangential stress on the outer edge is faithfully reproduced. An extremely fine finite element mesh would be required to obtain a comparable level of accuracy, particularly, for the surface stresses.

3.6 Summary

A comprehensive boundary element method has been presented for transient thermoelastic analysis. This time-domain formulation requires discretization of only the surface of the component, and thus provides an attractive alternative to finite element analysis for this class of problems. In addition, steep thermal gradients, which often occur near the surface, can be captured more readily, since with a boundary element approach there are no shape functions to constrain the solution in the direction normal to the surface. For example, the circular disc analysis indicates the high level of accuracy that can be obtained. In fact, on the basis of reduced modeling effort and improved accuracy, it appears that the present boundary element method should be the preferred approach for general problems of transient thermoelasticity.

TABLE 3.1
SUDDEN HEATING OF A CUBE

Time (sec.)	Temperature ($^{\circ}$ F) at $Y = 0$			Axial Displacement (μ in.) at $Y = 1.0$			Lateral Stress (ksi) at $Y = 0.5312$		
	Exact	FE	BEM	Exact	FE	BEM	Exact	FE	BEM
0.8	4.7	3.4	3.8	910	860	920	-5.6	-3.9	-5.4
1.6	22.0	19.8	20.7	1290	1250	1320	-9.1	-7.7	-9.2
2.4	38.3	36.4	37.7	1570	1540	1610	-11.3	-10.3	-11.7
3.2	51.5	50.0	51.5	1780	1760	1840	-13.1	-12.2	-13.5
4.0	61.9	60.7	62.2	1950	1930	2000	-14.4	-13.8	-14.8
4.8	70.1	69.1	70.5	2090	2070	2130	-15.5	-15.0	-15.9
5.6	76.5	75.7	76.9	2200	2180	2230	-16.3	-15.9	-16.7
6.4	81.5	80.9	81.9	2280	2270	2310	-17.0	-16.7	-17.3
7.2	85.5	84.9	85.8	2340	2330	2370	-17.5	-17.2	-17.8
8.0	88.6	88.2	88.8	2400	2390	2410	-17.9	-17.7	-18.1

FIGURE 3.1

ALUMINUM BLOCK

Problem Definition

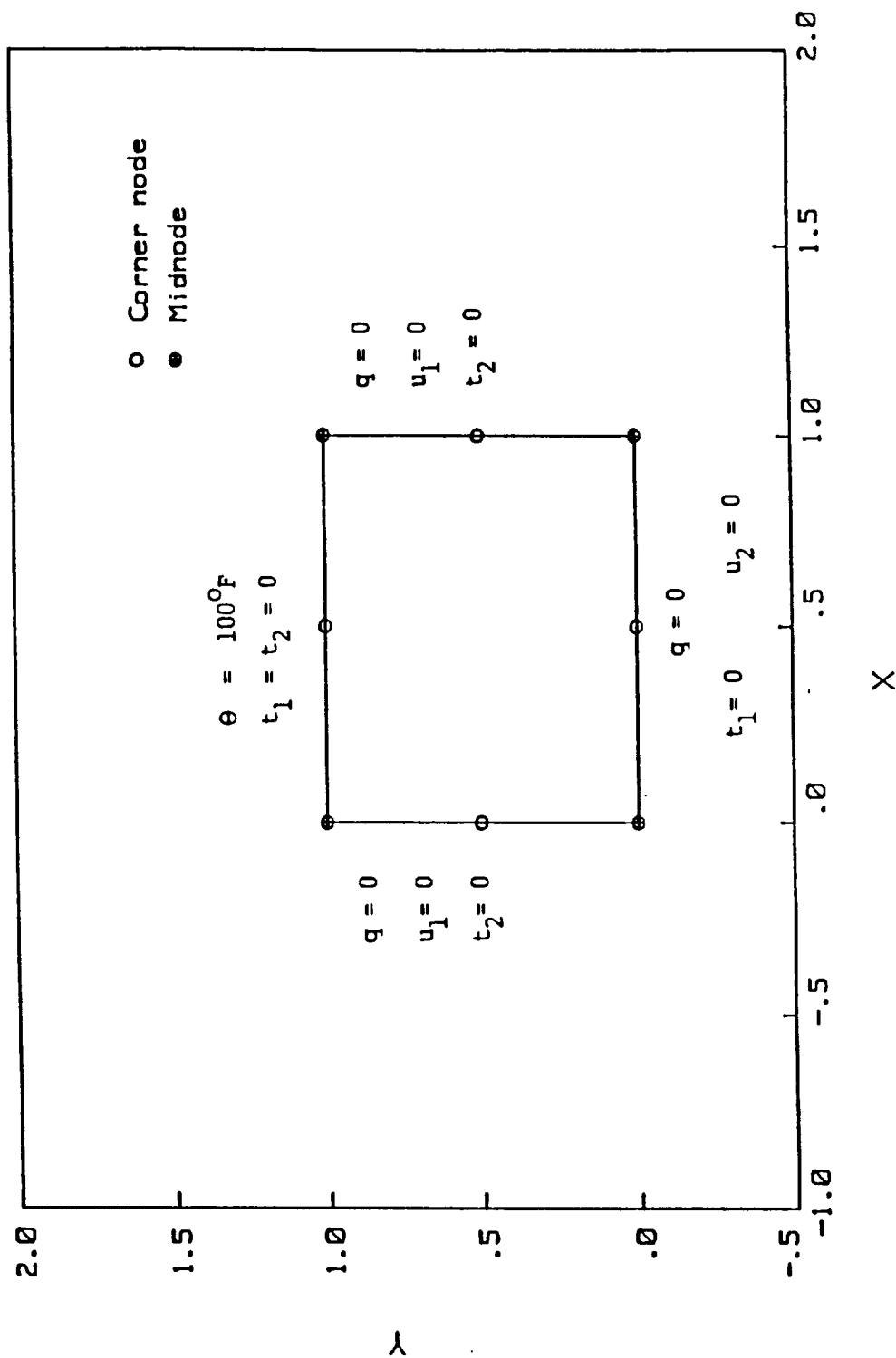


FIGURE 3.2
CIRCULAR DISC
Boundary Element Model

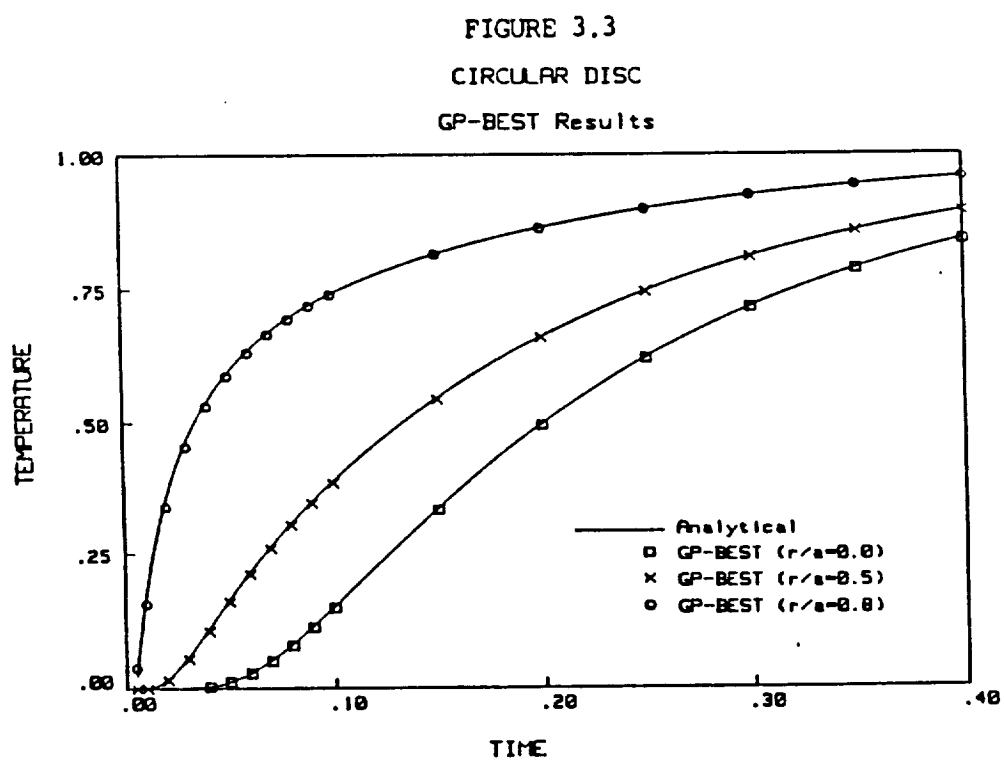
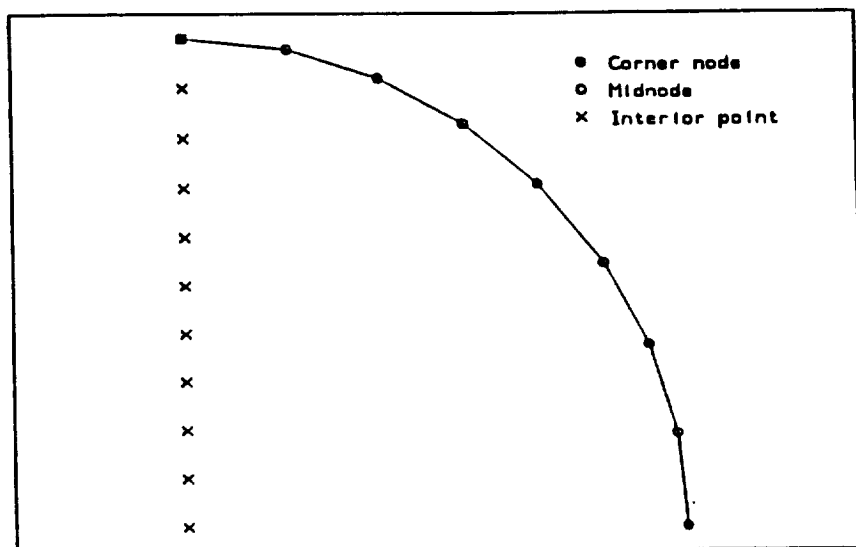


FIGURE 3.4
CIRCULAR DISC
GP-BEST Results

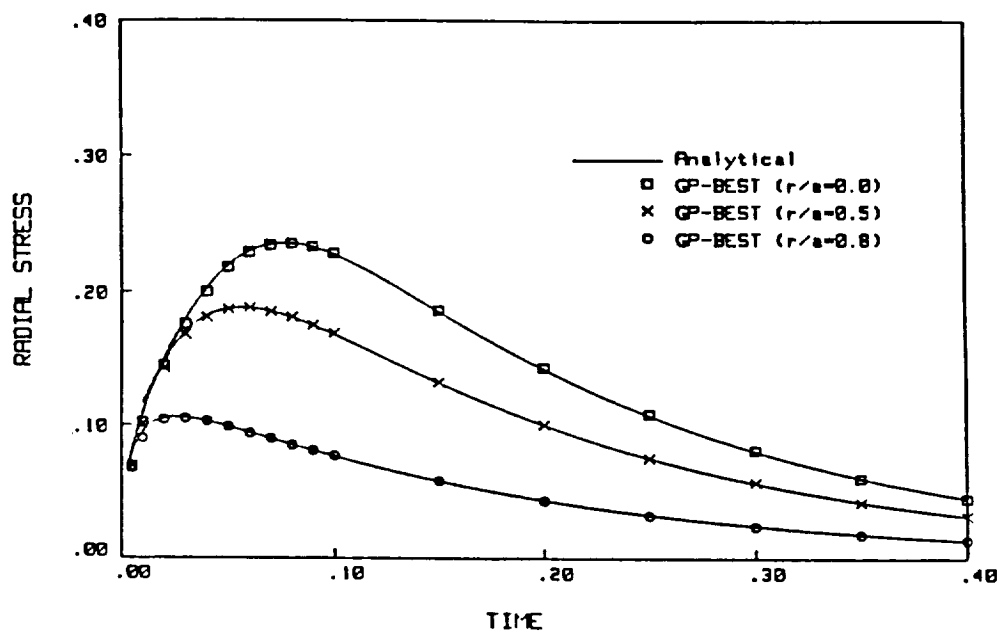
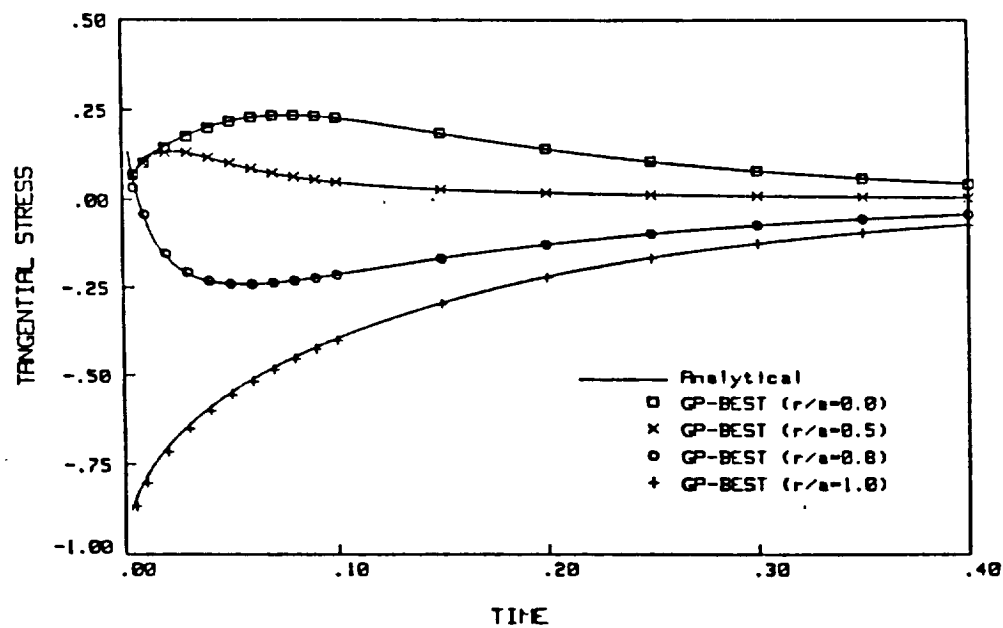


FIGURE 3.5
CIRCULAR DISC
GP-BEST Results



4. INTEGRAL FORMULATION FOR FLUIDS

4.1 Introduction

Attention is now shifted to the hot fluid. A number of integral formulations will be presented for both incompressible and compressible thermoviscous flow. In particular, significant effort has been directed recently toward the development and implementation of the convective formulations. As a result, boundary element solutions can now be obtained in the high Reynolds number range.

The presentation is separated into the three classes, namely, incompressible, convective incompressible and convective compressible flow. Individual subsections under each heading present the governing equations, integral representations, numerical implementation and numerical examples. It will be evident that significant progress has been made in the development of boundary element methods for both incompressible cases. On the other hand, for the compressible case, most of the effort has been necessarily directed toward the derivation of new fundamental solutions, which capture the essential character of the flow field.

4.2 Incompressible Thermoviscous Flow

4.2.1 Introduction

In the following, steady and time-dependent formulations are presented for relatively slow incompressible flow. The primary variables in each case are velocity, temperature, traction and heat flux. This is the set of variables for which boundary conditions are most readily defined, and for which the extension to three-dimensions is most easily accomplished. As will be seen, the individual formulations have much in common. The major differences involve the fundamental solutions that are employed, and the treatment of the contributions of past events. Both formulations have been implemented within the computer code GP-BEST.

4.2.2 Governing Equations

Application of the Principles of the Conservation of Mass, Momentum and Energy for an incompressible thermoviscous fluid lead to the development of the following differential equations:

$$\frac{\partial v_i}{\partial x_i} = 0 \quad (4.1a)$$

$$\mu \frac{\partial^2 v_i}{\partial x_j \partial x_j} - \frac{\partial p}{\partial x_i} - \rho \frac{D v_i}{D t} + f_i = 0 \quad (4.1b)$$

$$k \frac{\partial^2 \theta}{\partial x_j \partial x_j} - \rho c_e \frac{D \theta}{D t} + \psi = 0 \quad (4.1c)$$

where

x_i Eulerian coordinate

t time

v_i velocity vector

p pressure

θ temperature

ρ mass density

μ viscosity

k thermal conductivity

c_e specific heat

f_i body force

ψ body source,

and the operator

$$\frac{D}{D t} = \frac{\partial}{\partial t} + v_j \frac{\partial}{\partial x_j} \quad (4.2)$$

represents a material time derivative. By introducing a constant free stream velocity U_i and a velocity perturbation u_i , such that

$$v_i = U_i + u_i, \quad (4.3)$$

the governing equations can be rewritten as

$$\frac{\partial u_i}{\partial x_i} = 0 \quad (4.4a)$$

$$\mu \frac{\partial^2 u_i}{\partial x_j \partial x_j} - \frac{\partial p}{\partial x_i} - \rho \frac{\partial u_i}{\partial t} - \rho U_j \frac{\partial u_i}{\partial x_j} - \rho u_j \frac{\partial u_i}{\partial x_j} + f_i = 0 \quad (4.4b)$$

$$k \frac{\partial^2 \theta}{\partial x_j \partial x_j} - \rho c_\epsilon \frac{\partial \theta}{\partial t} - \rho c_\epsilon U_j \frac{\partial \theta}{\partial x_j} - \rho c_\epsilon u_j \frac{\partial \theta}{\partial x_j} + \psi = 0. \quad (4.4c)$$

Note that in equations (4.4) only the terms $\rho u_j \frac{\partial u_i}{\partial x_j}$ and $\rho c_\epsilon u_j \frac{\partial \theta}{\partial x_j}$ are actually nonlinear, although in some instances the body forces and sources may also contain nonlinearities. A number of distinct integral formulations are possible, depending upon which of the linear terms are included in the differential operator. All terms excluded from the differential operator, must then be grouped together as effective body forces and sources, f'_i and ψ' , respectively. Integral formulations based upon Stokes kernels are detailed in the next subsection.

4.2.3 Integral Representations

4.2.3.1 Steady

In this first formulation the time-dependent terms vanish, and the entire contribution of the convective terms are considered as effective body forces and sources. Thus,

$$f'_i = -\rho U_j \frac{\partial u_i}{\partial x_j} - \rho u_j \frac{\partial u_i}{\partial x_j} + f_i \quad (4.5a)$$

$$\psi' = -\rho c_\epsilon U_j \frac{\partial \theta}{\partial x_j} - \rho c_\epsilon u_j \frac{\partial \theta}{\partial x_j} + \psi. \quad (4.5b)$$

As a result, the well-known fundamental solutions for incompressible Stokes flow and steady-state heat conduction are applicable. The integral formulation, which can be derived directly from the governing differential equation (Dargush and Banerjee, 1990c), can be written

$$c_{\alpha\beta} u_\alpha = \int_S [G_{\alpha\beta} t_\alpha - F_{\alpha\beta} u_\alpha - G_{\alpha\beta} t_\alpha^0] dS + \int_V [D_{\alpha\beta k} \sigma_{k\alpha}^0 + G_{\alpha\beta} f_\alpha] dV \quad (4.6)$$

where

$$u_\alpha = \{u_1 \ u_2 \ \theta\} \quad (4.7a)$$

$$t_\alpha = \{t_1 \ t_2 \ q\} \quad (4.7b)$$

$$f_\alpha = \{f_1 \ f_2 \ \psi\} \quad (4.7c)$$

are generalized velocities, tractions, and body forces. In (4.7b), t_i are the surface tractions defined by

$$t_i = \tau_{ij} n_j - p n_i \quad (4.8a)$$

with n_i representing the local unit outward normal to the surface S , and τ_{ij} the fluid stresses, while the heat flux is defined via

$$q = -k \frac{\partial \theta}{\partial x_i} n_i. \quad (4.8b)$$

Furthermore,

$$c_{\alpha\beta} = \begin{bmatrix} c_{ij} & 0 \\ 0 & c_{\theta\theta} \end{bmatrix} \quad , \quad G_{\alpha\beta} = \begin{bmatrix} G_{ij} & 0 \\ 0 & G_{\theta\theta} \end{bmatrix} \quad , \quad F_{\alpha\beta} = \begin{bmatrix} F_{ij} & 0 \\ 0 & F_{\theta\theta} \end{bmatrix} \quad (4.9a, b, c)$$

$$D_{\alpha\beta k} = \frac{\partial G_{\alpha\beta}}{\partial x_k} \quad (4.9d)$$

$$\sigma_{k\alpha}^o = [\rho(U_k + u_k)u_i \quad \rho c_\epsilon(U_k + u_k)\theta] \quad (4.10a)$$

$$t_\alpha^o = \sigma_{k\alpha}^o n_k. \quad (4.10b)$$

In the terminology of Lighthill (1952), $\sigma_{k\alpha}^o$ is the momentum flux tensor or fluctuating Reynolds stress. Here, $\sigma_{k\alpha}^o$ is labeled the generalized convective stress tensor, while t_α^o is the generalized convective traction. Both $\sigma_{k\alpha}^o$ and t_α^o contain terms which are nonlinear in the generalized velocities.

In (4.9a), $c_{ij}(\xi)$ and $c_{\theta\theta}(\xi)$ are constants. When ξ is inside S , $c_{ij} = \delta_{ij}$ and $c_{\theta\theta} = 1$. If ξ is on the boundary then the values are determined by the relative smoothness of S at ξ . For ξ outside the region V , both c_{ij} and $c_{\theta\theta}$ are zero. Meanwhile, the kernel functions G_{ij} , $G_{\theta\theta}$, F_{ij} and $F_{\theta\theta}$ are provided in Appendix B.2.

4.2.3.2 Time-Dependent

For this next formulation, the effective body forces and sources are identical to those provided in (4.5), however, the time-dependent terms are now included in the linear operator. The required fundamental solution for the viscous portion was first given by Oseen (1927), while the transient heat conduction fundamental solution is well-known (Carslaw and Jaeger, 1959). By applying standard methodology (Banerjee and Butterfield, 1981; Dargush and Banerjee, 1990d), the following governing integral equations can be derived

$$c_{\alpha\beta}u_{\alpha} = \int_S [g_{\alpha\beta} * t_{\alpha} - f_{\alpha\beta} * u_{\alpha} - g_{\alpha\beta} * t_{\alpha}^0] dS + \int_V [d_{\alpha\beta k} * \sigma_{k\alpha}^0 + g_{\alpha\beta} * f_{\alpha} - g_{\alpha\beta} \rho u_{\alpha}^0] dV \quad (4.11)$$

Note that (4.11) is similar to (4.6) for the steady case, except that Riemann convolution integrals over time have been introduced, along with an initial condition volume integral involving u_{α}^0 . Once again $\sigma_{k\alpha}^0$ and t_{α}^0 contain terms which are nonlinear in the generalized velocities. Kernel functions, $G_{\alpha\beta}$ and $F_{\alpha\beta}$, developed from the instantaneous point force and source adjoint fundamental solutions $g_{\alpha\beta}$ and $f_{\alpha\beta}$, are provided in Appendix B.3. It should be noted that these functions are considerably more complicated than the corresponding steady kernels.

4.2.4 Numerical Implementation

4.2.4.1 Introduction

Analytical solutions are possible for only the simplest geometries and boundary conditions. More generally, approximations must be introduced in both time and space to expose the practical utility of these integral equations. Consequently, in this section, state-of-the-art boundary element technology is applied to steady and unsteady incompressible thermoviscous flows. Recent boundary element developments in the fields of elastodynamics (Banerjee et al, 1986; Ahmad and Banerjee, 1988) and thermoelasticity (Dargush and Banerjee, 1989b, 1990a) are directly applicable for these problems. The presentation below will concentrate on those aspects of the numerical implementation which differ from that detailed in Section 3. The current implementation is limited to the two-dimensional case,

although certainly both of the integral formulations presented in the previous subsection are equally valid in three dimension.

4.2.4.2 Temporal and Spatial Discretization

For time-dependent problems, the total time interval from zero to τ is subdivided into N equal increments of duration $\Delta\tau$. Then, the field variables $t_\alpha, u_\alpha, t_\alpha^o$, and $\sigma_{k\alpha}^o$ are assumed constant within each $\Delta\tau$ time increment. As a result,

$$g_{\alpha\beta} * t_\alpha \cong \sum_{n=1}^N t_\alpha^n \int_{(n-1)\Delta\tau}^{n\Delta\tau} g_{\alpha\beta} dt = \sum_{n=1}^N t_\alpha^n G_{\alpha\beta}^{N-n+1} \quad (4.12)$$

with similar expressions holding for the remaining convolution integrals. This is identical to the treatment discussed in Section 3 for thermoelasticity.

The methodology employed for spatial discretization of the bounding surface also follows that described in Section 3. Thus, linear, quadratic or quartic shape functions are utilized to portray the functional behavior of the field variables over three-noded surface elements.

However, in addition to the surface description, the domain must be discretized into cells in the regions where the nonlinear convective effects are important, or where nonzero initial conditions are present. Shape functions are once again introduced to approximate the geometric and functional variation with each volume cell. Thus, for any point X within an individual cell

$$x_i(\zeta) = M_w(\zeta)x_{iw} \quad (4.13)$$

and

$$\sigma_{iw}^o(\zeta) = M_w(\zeta)\sigma_{iw}^o \quad (4.14)$$

where

M_w, M_w shape functions

x_{iw} nodal coordinates

σ_{iw}^o nodal generalized convective stress .

The current implementation utilizes six and eight-noded cells for the geometric representation, along with linear, quadratic, or quartic functional variation. Typical cells are depicted in Figure 4.1. For the quadratic cell, both serendipity (8-noded) and lagrangian (9-noded) variations are included. Serendipity quartic cells were found to have unsatisfactory performance and consequently are not available.

As a result of the spatial discretization, the boundary integral equation for time-dependent thermoviscous flow can now be written

$$c_{\alpha\beta}u_{\alpha}^N = \sum_{n=1}^N \left\{ \sum_{m=1}^M \left[t_{\alpha\omega}^n \int_{S_m} G_{\alpha\beta}^{N-n+1} N_{\omega} dS - u_{\alpha\omega}^n \int_{S_m} F_{\alpha\beta}^{N-n+1} N_{\omega} dS - t_{\alpha\omega}^n \int_{S_m} G_{\alpha\beta}^{N-n+1} N_{\omega} dS \right] \right. \\ \left. + \sum_{l=1}^L \left[\sigma_{k\alpha\omega}^n \int_{V_l} D_{\alpha\beta k}^{N-n+1} M_{\omega} dV \right] \right\} + \sum_{l=1}^L \left[\rho u_{\alpha\omega}^0 \int_{V_l} g_{\alpha\beta}^N M_{\omega} dV \right] \quad (4.15a)$$

while for steady conditions this reduces to

$$c_{\alpha\beta}u_{\alpha} = \sum_{m=1}^M \left[t_{\alpha\omega} \int_{S_m} G_{\alpha\beta} N_{\omega} dS - u_{\alpha\omega} \int_{S_m} F_{\alpha\beta} N_{\omega} dS - t_{\alpha\omega}^0 \int_{S_m} G_{\alpha\beta} N_{\omega} dS \right] \\ + \sum_{l=1}^L \left[\sigma_{k\alpha\omega}^0 \int_{V_l} D_{\alpha\beta k} M_{\omega} dV \right], \quad (4.15b)$$

where M and L are the total number of surface elements and volume cells, respectively, and

$$S = \sum_{m=1}^M S_m \quad (4.16a)$$

$$V = \sum_{l=1}^L V_l. \quad (4.16b)$$

The positioning of the nodal variables outside of the integrals is a key step, since now the integrands of (4.15) contain only known functions, which can be evaluated numerically.

Up to this juncture, the region of interest has been assumed to be composed of a single volume V with surface S . However, this need not be the case. In general, space may be subdivided into a number of individual non-overlapping geometric modeling regions (GMRs). Each GMR occupies a certain volume of space, say V_g , bounded by the surface S_g . For a point ξ within V_g , the integration required by (4.15) need only be conducted over S_g and V_g , since the contribution to $u_{\alpha}(\xi)$ from the other GMRs outside S_g will be zero.

As a result, integration costs can be dramatically reduced by introducing multiple GMRs for thermoviscous flow problems. Additionally, there is no inherent requirement that all GMRs utilize the same physical model. For example, one GMR could employ the steady formulation of equation (4.6), while a second region includes the transient kernel effects contained in the formulation of (4.11). In any case, compatibility must, of course, be maintained across all GMR-to-GMR interfaces. Examples of mixed GMR formulation are contained in Section 4.3.6 and form the basis of the approach for fluid structure interaction that will be explored in Section 5.

4.2.4.3 Integration

The evaluation of the integrals appearing in (4.15) is the next process to be examined. Due to the singular nature of the kernel functions $G_{\alpha\beta}$, $F_{\alpha\beta}$ and $D_{\alpha\beta k}$ considerable care must be exercised during numerical integration. This is particularly true for incompressible viscous flow, in which the final solution is extremely sensitive to errors in integration coefficients. In general, the integration algorithms must be much more sophisticated than those developed for thermoelasticity. In the present implementation, discussed in detail in Honkala and Dargush (1990), a number of different integration schemes are employed depending upon the order of the kernel singularity, the proximity of the field point ξ to the element, and the size of the element.

Once again consider the following three distinct categories for the surface integrals:

- (1) The point ξ does not lie on the element m .
- (2) The point ξ lies on the element m , but the kernels involve only weakly singular integrands of the $\ln r$ type.
- (3) The point ξ lies on the element m , and the integral has a strong $\frac{1}{r}$ singularity.

In practical problems involving many elements, it is evident that most of the integration occurring in equation (4.15) will be of the Category (1) variety. The integrand is non-singular and standard Gaussian quadrature can be employed. However, for near-singular

cases when ξ is close to element m very high order formulas are needed to capture the kernel behavior. For these instances, it is beneficial to identify the point X^o on the element nearest to ξ , and then subdivide the interval of integration about X^o . Within each of the two subsegments a nonlinear transformation is used to further reduce the order of Gaussian quadrature needed for high precision. This nonlinear transformation is similar to that proposed by Mustoe (1984) and Telles (1987), however it should be emphasized that subsegmentation is still required.

Turning next to Category (2), one finds that, unlike elasticity or potential flow, standard Gaussian formulas alone are inadequate. Instead the terms involving $\ln r$ must be isolated and integrated with special log-weighted Gaussian integration. The remaining non-singular terms comprising $G_{\alpha\beta}$ are then evaluated utilizing standard quadrature.

The strongly singular integrals of Category (3) exist only in the Cauchy principal value sense and cannot be evaluated numerically with sufficient precision. Fortunately, the indirect ‘rigid body’ or ‘equipotential’ method, originally developed by Cruse (1974), is applicable, and leads to the accurate determination of the singular block of the second integral in (4.15). The remainder of that integral is non-singular. Consequently, subsegmentation along with standard Gaussian quadrature is adequate.

Similar care is needed for the volume integrals, which involve the kernel $D_{\alpha\beta k}$ containing a $\frac{1}{r}$ -type singularity. However, for two-dimensional volume integration, this kernel is only weakly singular, and can be evaluated in the following direct manner. First, the nearest node, say A , in cell l to the point ξ is determined. The cell is then subdivided into triangles radiating from A as shown in Figure 4.3. Next, each triangle is mapped onto a unit square. The apex corresponding to A is stretched to form one side of the square. This process essentially eliminates the $\frac{1}{r}$ singularity. Finally, the square is further subsegmented in both radial and circumferential directions depending upon the closeness of ξ and the size of cell l . Standard Gaussian quadrature is applied to each subsegment. This cell integration scheme was based on work by Mustoe (1984) for elastoplasticity. In

the present incompressible viscous flow implementation, tolerances have been tightened so that additional subsegmentation is performed, along with higher order quadrature formulas. Additionally, it has been found that circumferential subsegmentation is much more beneficial than the radial breakup.

In time-dependent problems, beyond the first time step, additional integration is required. This integration involves the kernels $G_{\alpha\beta}^n, F_{\alpha\beta}^n$ and $D_{\alpha\beta k}^n$ for $n > 1$. From Table 4.1, these are all nonsingular. As a result, a much less sophisticated integration scheme is employed to obtain the required level of accuracy with fewer subsegments and gauss points. If the initial velocities are not uniform, then the nonsingular initial condition integral of equation (4.15a) must also be evaluated at each time step. This is accomplished in a manner similar to the integration of $D_{\alpha\beta k}^n$.

Table 4.1 - Kernel Singularities

<u>Kernel</u>	<u>Singularity Order</u>
$G_{\alpha\beta}^1$	$\ln r$
$G_{\alpha\beta}^n$ for $n > 1$	non-singular
$F_{\alpha\beta}^1$	$\frac{1}{r}$
$F_{\alpha\beta}^n$ for $n > 1$	non-singular
$D_{\alpha\beta k}^1$	$\frac{1}{r}$
$D_{\alpha\beta k}^n$ for $n > 1$	non-singular

4.2.4.4 Assembly

Once the spatial discretization and numerical integration algorithms are completely defined, a system of nonlinear algebraic equations can be developed to permit an approximate solution of the thermoviscous boundary value problem. The method of collocation is employed by writing (4.15) at each functional mode.

For each time step N of a transient problem, this nodal collocation process yields

$$\sum_{n=1}^N [\mathbf{G}^{N-n+1} \mathbf{t}^n - \mathbf{F}^{N-n+1} \mathbf{u}^n - \mathbf{G}^{N-n+1} \mathbf{t}^{on} + \mathbf{D}^{N-n+1} \boldsymbol{\sigma}^{on}] - \boldsymbol{\Gamma}^N \mathbf{u}^o = \mathbf{0} \quad (4.17)$$

where

\mathbf{t}^n	nodal traction vector for time step n with 3Q components
\mathbf{u}^n	nodal velocity vector for time step n with 3P components
\mathbf{t}^{on}	nodal convective traction vector for time step n with 3Q components
$\boldsymbol{\sigma}^{on}$	nodal convective stress vector for time step n with 6P components
\mathbf{u}^o	nodal initial velocity vector with 3P components
\mathbf{G}^n	unassembled matrix of size 3P x 3Q calculated from the first integral of (4.15) during time step n
\mathbf{F}^n	assembled matrix of size 3P x 3P calculated from the second integral of (4.15) during time step n , plus the $c_{\alpha\beta}$ contribution in \mathbf{F}^1
\mathbf{D}^n	assembled matrix of size 3P x 6P calculated from the first volume integral of (4.15) .
$\boldsymbol{\Gamma}^N$	assembled matrix of size 3P x 3P calculated from the initial condition integral of (4.15)
P	total number of functional nodes
$Q = \sum_{m=1}^M A_m$	
A_m	number of functional nodes in element m .

All of the coefficient matrices in (4.17) contain independent blocks for each GMR in multiregion problems. However, for any well-posed problem, the boundary conditions and interface relations remove all but 3P unknown components of \mathbf{u}^N and \mathbf{t}^N . Furthermore,

by solving (4.17) at each increment of time, all of the components of $\mathbf{u}^n, \mathbf{t}^n, \mathbf{t}^{on}$ and σ^{on} for $n < N$ are known from previous time steps. Then, (4.17) can be rewritten at time $N\Delta\tau$ as

$$\begin{aligned} \mathbf{g}(\mathbf{x}) &= \mathbf{Ax}^N - \mathbf{D}^1\sigma^{on} + \mathbf{G}^1\mathbf{t}^{on} - \mathbf{By}^N \\ &\quad - \sum_{n=1}^{N-1} [\mathbf{G}^{N-n+1}\mathbf{t}^n - \mathbf{F}^{N-n+1}\mathbf{u}^n - \mathbf{G}^{N-n+1}\mathbf{t}^{on} + \mathbf{D}^{N-n+1}\sigma^{on}] + \mathbf{\Gamma}^N\mathbf{u}^o = 0 \end{aligned} \quad (4.18)$$

in which

\mathbf{x}^N nodal vector of unknowns with 3P components

\mathbf{y}^N nodal vector of knowns with 3Q components

while \mathbf{A} and \mathbf{B} are the associated coefficient obtained from \mathbf{F}^1 and \mathbf{G}^1 . The \mathbf{A} matrix now includes the compatibility relationships enforced on GMR interfaces. As a result, the GMR blocks in \mathbf{A} are no longer independent, however \mathbf{A} does remain block banded.

The terms included in the summation of (4.18) represent the contribution of past events. This, along with the terms \mathbf{By}^N and $\mathbf{\Gamma}^N\mathbf{u}^o$, can be simply evaluated once at each time step N with no need for iteration. Let,

$$\mathbf{b}^N = -\mathbf{By}^N - \sum_{n=1}^{N-1} [\mathbf{G}^{N-n+1}\mathbf{t}^n - \mathbf{F}^{N-n+1}\mathbf{u}^n - \mathbf{G}^{N-n+1}\mathbf{t}^{on} + \mathbf{D}^{N-n+1}\sigma^{on}] + \mathbf{\Gamma}^N\mathbf{u}^o. \quad (4.19)$$

Then (4.18) becomes the following nonlinear set of algebraic equations

$$\mathbf{g}(\mathbf{x}) = \mathbf{Ax}^N - \mathbf{D}^1\sigma^{on} + \mathbf{G}^1\mathbf{t}^{on} + \mathbf{b}^N = 0. \quad (4.20)$$

A closer examination of \mathbf{b}^N is in order. For example with $N = 1$

$$\mathbf{b}^1 = -\mathbf{By}^1 + \mathbf{\Gamma}^1\mathbf{u}^o, \quad (4.21a)$$

while for the second time step

$$\mathbf{b}^2 = -\mathbf{By}^2 - \mathbf{G}^2\mathbf{t}^1 + \mathbf{F}^2\mathbf{u}^1 + \mathbf{G}^2\mathbf{t}^{o1} - \mathbf{D}^2\sigma^{o1} + \mathbf{\Gamma}^2\mathbf{u}^o \quad (4.21b)$$

Obviously, for each step N , one new set of matrices $\mathbf{G}^N, \mathbf{F}^N, \mathbf{D}^N$ and $\mathbf{\Gamma}^N$ must be determined via integration and assembly. Integration, particularly the volume integration needed for \mathbf{D}^N and \mathbf{T}^N , can be quite expensive.

As an alternative to the convolution approach defined above, a time marching recurring initial condition algorithm can be employed. This has been utilized by a number of researchers for transient problems of heat conduction, acoustics, and elasticity (Banerjee and Butterfield, 1981). For this latter approach, at time step N the entire contribution of past events is represented by an initial condition integral which utilizes \mathbf{u}^{N-1} as the initial velocity. Thus,

$$\mathbf{g}(\mathbf{x}) = \mathbf{Ax}^N - \mathbf{D}^1 \sigma^{oN} + \mathbf{G}^1 t^{oN} + \mathbf{b}^N = 0 \quad (4.22)$$

with

$$\mathbf{b}^N = -\mathbf{By}^N + \mathbf{I}^1 \mathbf{u}^{N-1}. \quad (4.23)$$

Obviously, (4.22) is identical to (4.20). Only the evaluation of \mathbf{b}^N is different. The advantage of the recurring initial condition approach is that no integration is needed beyond the first time step. However, volume integration is required throughout the entire domain because of the presence of \mathbf{u}^{N-1} , even for linear problems in which volume integration would not normally be required.

In order to take full advantage of both methods, the present work utilizes the convolution approach in linear regions, and the recurring initial condition algorithm for the remaining nonlinear GMRs which are filled with volume cells. Since \mathbf{b}^N can be computed independently for each GMR, this new dual approach provides no particular difficulty.

4.2.4.5 Solution

An iterative algorithm, along the lines of those traditionally used for BEM elastoplasticity (Banerjee and Butterfield, 1981; Banerjee et al, 1987), can be employed to solve the boundary value problem. However, convergence is usually achieved only at low Reynolds number. More generally the interior equations must be brought into the system matrix, as in (4.20), and a full or modified Newton-Raphson algorithm must be employed to obtain solutions even at moderate Reynolds number. (Similar 'variable stiffness' algorithms have also been introduced by Banerjee and Raveendra (1987) and Henry and Banerjee (1988))

for elastoplasticity.) Symbolically, at any iteration k ,

$$\left[\frac{\partial \mathbf{g}}{\partial \mathbf{x}}(\mathbf{x}^l) \right] \left\{ \Delta \mathbf{x}^k \right\} = - \left\{ \mathbf{g}(\mathbf{x})^k \right\} \quad (4.24)$$

where

$$\mathbf{x}^{k+1} = \mathbf{x}^k + \Delta \mathbf{x}^k \quad (4.25)$$

and the derivatives on the lefthand side of (4.24) are evaluated at \mathbf{x}^k . With the full Newton-Raphson approach, $l = k$ and the system matrix must be formed and decomposed at each iteration. The out-of-core solver used in the present implementation was developed originally for elastostatics (Banerjee et al, 1985) from the LINPACK software package (Dongarra et al, 1979), and operates on a submatrix level. Within each submatrix, Gaussian elimination with single pivoting reduces the block to upper triangular form. The final decomposed compacted form of the system matrix is stored in a direct access file for later reuse. Backsubstitution completes the determination of $\Delta \mathbf{x}^k$. Iteration continues until

$$\frac{\|(\Delta \mathbf{x}^N)^k\|}{\|(\mathbf{x}^N)^k\|} < \epsilon \quad (4.26)$$

where ϵ is a small tolerance, and $\|\mathbf{x}\|$ is the Euclidean norm of \mathbf{x} . For the modified Newton-Raphson algorithm, the system matrix is not formed at every iteration, and only backsubstitution is needed to determine $\Delta \mathbf{x}^k$.

4.2.4.6 Calculation of Additional Boundary Quantities

Once the iterative process has converged, a number of additional boundary quantities of interest can be easily calculated. For example, lift and drag can be calculated by numerically integrating the known nodal traction and shape function products over the surface elements of interest. Low order Gaussian quadrature is adequate for this integration, since all the functions are very well behaved.

Furthermore, at each boundary node, the pressure p , stress σ_{ij} , and strain rates $\frac{\partial u_i}{\partial x_j}$ can be determined by simultaneously solving the following relationships:

$$\sigma_{ji}(\xi) n_j(\xi) = N_\omega(\zeta) t_{i\omega} \quad (4.27a)$$

$$\sigma_{ij}(\xi) - \mu \left(\frac{\partial u_i}{\partial x_j}(\xi) + \frac{\partial u_j}{\partial x_i}(\xi) \right) + p(\xi) = 0 \quad (4.27b)$$

$$\frac{\partial x_j}{\partial \zeta} \frac{\partial u_i}{\partial x_j}(\xi) = \frac{\partial N_\omega}{\partial \zeta} u_{i\omega} \quad (4.27c)$$

$$\frac{\sigma_{ii}(\xi)}{2} + p(\xi) = 0. \quad (4.27d)$$

It should be emphasized that (4.27) represents a set of nine independent equations which are written at the boundary point ξ , and can be solved easily for p , σ_{ij} and $\frac{\partial u_i}{\partial x_j}$ at that point. Afterward, boundary vorticity and dilatation can be obtained, respectively, from

$$\Omega = \frac{\partial u_2}{\partial x_1} - \frac{\partial u_1}{\partial x_2} \quad (4.28a)$$

$$\Delta = \frac{\partial u_1}{\partial x_1} + \frac{\partial u_2}{\partial x_2}. \quad (4.28b)$$

Of course, for incompressible flow, the dilatation should be zero, but (4.28b) can be used as a check.

A comprehensive PATRAN interface has also been developed. Consequently, any of the quantities computed above may be displayed graphically in the form of profiles or contours.

4.2.5 Numerical Examples

4.2.5.1 Introduction

All of the formulations discussed above have been implemented as a segment of GP-BEST, a general purpose boundary element code. In this section, a number of examples are included, primarily, to demonstrate the validity and attractiveness of the boundary element formulations for relatively slow incompressible flow.

4.2.5.2 Converging Channel

The two-dimensional incompressible flow through a converging channel also possesses a well known analytical solution which is purely radial (Millsaps and Pohlhausen, 1953). A comprehensive finite element study of this problem has been made by Gartling et al (1977).

The boundary element model is shown in Figure 4.4a. The mesh contains 96 cells and is divided into two regions. The boundary conditions were modeled using an exact specification of the boundary conditions appearing in the analytical solution (Fig. 4.4a). Viscosity is unity, and tractions and density are incremented to reach higher Reynolds numbers. The Reynolds number for this problem is defined as

$$R_e = \frac{\rho R_i V_2(R_i)}{\nu} \quad (4.29)$$

where $V_2(R_i)$ is the maximum velocity in the region, which is -24.0 for the problem solved here.

Figure 4.4b illustrates the results for two Reynolds numbers, indicating good accuracy along the entire width of the channel. Not only are the velocities accurate, but the pressures and tractions are very accurate also.

It has been observed that finite element versions of this problem have several peculiarities which prevent the analytical solution from being reproduced. First of all, since velocities are often specified at the inlet and at the wall and centerline, ambiguous boundary condition specification results. Also, typically a parabolic "fully developed" velocity profile is usually specified at the inlet. However, the nonlinear solution has a flattened velocity distribution across the width of the channel (see Fig. 4.4b). Hence, the analytical solution cannot be reproduced exactly if the "fully developed" profile is specified at the inlet. Also, the finite element modelers of this problem usually leave out the traction distribution at the exit and specify zero tractions there. This also gives rise to non-radial flow.

The reason for so much interest in the converging flow problem is that it is one of the few problems possessing an analytical solution. However, by specifying a model which does not correspond to this problem, as in the finite element case, one cannot accurately compare results to the analytical solution. Any such comparisons are merely qualitative. In this light, the boundary element model here has utilized an exact model of the boundary condition and a meaningful comparison can be made.

4.2.5.3 Transient Couette Flow

Consider as the first transient analysis the case of developing Couette flow between two plates, parallel to the x-z plane, a distance h apart. Initially, both of the plates, as well as the fluid, are at rest. Then, beginning at time $t = 0$, the bottom plate is moved continuously with velocity V in the x-direction. Due to the no-slip condition at the fluid-plate interface, Couette flow begins to develop as the vorticity diffuses. Eventually, when steady conditions prevail, the x-component of the velocity assumes a linear profile.

The following exact solution to this unsteady problem is provided by Schlichting (1955):

$$v_x(y, t) = V \left\{ \sum_{n=0}^{\infty} erfc[2n\eta_1 + \eta] - \sum_{n=0}^{\infty} erfc[2(n+1)\eta_1 - \eta] \right\} \quad (4.30a)$$

$$v_y(y, t) = 0 \quad (4.30b)$$

where

$$\eta = \frac{y}{(4\mu t/\rho)^{1/2}} \quad \eta_1 = \frac{h}{(4\mu t/\rho)^{1/2}} \quad (4.31a, b)$$

$$erfc(z) = 1 - erf(z) = 1 - \frac{2}{\pi^{1/2}} \int_0^z e^{-\gamma^2} d\gamma. \quad (4.31c)$$

All of the nonlinear terms vanish, since both v_y and $\partial v_x / \partial x$ are zero.

The two-dimensional boundary element model, utilized for this problem, is displayed in Figure 4.5. Four quadratic surface elements are employed, with one along each edge of the domain. A number of sampling points are included strictly to monitor response. Notice that the region of interest is arbitrarily truncated at the planes $x = 0$ and $x = \ell$. All of the boundary conditions are also shown in Figure 4.5. For the presentation of GPBEST results, all quantities are normalized. Thus,

$$Y = \frac{y}{h} \quad (4.32a)$$

$$T = \frac{ct}{h^2} \quad (4.32b)$$

and the horizontal velocity is v_x/V . Figure 4.6 provides the velocity profiles at four different times, using a time step $\Delta T = 0.025$ and the convolution approach. There is some error

present at small times near the top plate, where the velocity is nearly zero. Results at $Y = 0.5$ versus time are shown in Figure 4.7 for several values of the time step. Obviously, the correlation improves with a reduction in time step and $\Delta T = 0.025$ provides accurate velocities throughout the time history. However, even for a very large time step, the GPBEST solution shows no signs of instability. Error, evident in the initial portion, diminishes with time, and all values of ΔT produce the correct steady response. Further reduction of ΔT beyond 0.025 yields little benefit. Instead, mesh refinement in the y -direction is needed, primarily to capture the short time behavior. Figure 4.8 shows the GPBEST results for a model with just two, equal length, elements along each vertical side. The correlation with the analytical solution is now excellent. The time step selected for the refined model was based upon the general recommendation that

$$\Delta T \cong \frac{0.05\ell_{\min}^2}{c}, \quad (4.33)$$

where ℓ_{\min} is the length of the smallest element.

The convolution approach, defined by equation (4.18), was used to obtain the results presented in Figures 4.6-4.8. Alternatively, the recurring initial condition algorithm can be invoked. In that case, complete volume discretization is required even for this linear problem. For the model of Figure 4.6, a single volume cell connecting the eight nodes is all that is required. The GPBEST results for different values of ΔT are shown in Figure 4.9. The solutions are good for the two smaller time step magnitudes, however there is a slight degradation in accuracy from the convolution results.

Interestingly, the solution in (4.30a) is identical to that for one-dimensional transient heat conduction in an insulated rod with one end maintained at temperature V , while the other remains at zero. However, in a corresponding boundary element analysis, the numerical integrations defined in (4.15a) must be calculated much more precisely for unsteady viscous flow than for heat conduction in order to obtain comparable levels of accuracy.

4.2.5.4 Flow Between Rotating Cylinders

As the next example, the developing flow between rotating cylinders is analyzed. The inner cylinder of radius r_i is stationary, while the outer concentric cylinder with radius r_o is given a tangential velocity V , beginning abruptly at time zero. The steady solution appears in Schlichting (1955). However, even for the transient case, the flow is purely circumferential. Thus, the governing Navier-Stokes equations reduce to

$$\mu \left(\frac{\partial^2 v_\theta}{\partial r^2} + \frac{1}{r} \frac{\partial v_\theta}{\partial r} - \frac{v_\theta}{r^2} \right) - \rho \frac{\partial v_\theta}{\partial t} = 0 \quad (4.34a)$$

$$-\frac{\partial p}{\partial r} + \frac{v_\theta^2}{r} = 0 \quad (4.34b)$$

in polar coordinates (r, θ, z) . As discussed in Batchelor (1967), separation of variables can be used to obtain the following solution (Honkala and Dargush, 1990)

$$v_r(r, t) = 0 \quad (4.35a)$$

$$v_\theta(r, t) = c_1 r + \frac{c_2}{r} + \sum_{n=1}^{\infty} D_n \{ J_1(\lambda_n r) Y_1(\lambda_n r_o) - Y_1(\lambda_n r) J_1(\lambda_n r_o) \} e^{-\lambda_n^2 c t} \quad (4.35b)$$

where

$$c_1 = \frac{V r_o}{r_o^2 - r_i^2} \quad c_2 = -c_1 r_i^2 \quad (4.36a, b)$$

$$D_n = \frac{\pi^2}{2} \frac{\lambda_n J_1^2(\lambda_n r_i)}{J_1^2(\lambda_n r_i) - J_1^2(\lambda_n r_o)} \{ Y_1(\lambda_n r_o) F_{1n} + J_1(\lambda_n r_o) F_{2n} \} \quad (4.36c)$$

$$F_{1n} = -c_1 [r_o^2 J_2(\lambda_n r_o) - r_i^2 J_2(\lambda_n r_i)] + c_2 [J_o(\lambda_n r_o) - J_o(\lambda_n r_i)] \quad (4.36d)$$

$$F_{2n} = c_1 [r_o^2 Y_2(\lambda_n r_o) - r_i^2 Y_2(\lambda_n r_i)] - c_2 [Y_o(\lambda_n r_o) - Y_o(\lambda_n r_i)] \quad (4.36e)$$

and λ_n is the n th root of the equation

$$J_1(\lambda r_i) Y_1(\lambda r_o) - J_1(\lambda r_o) Y_1(\lambda r_i) = 0. \quad (4.37)$$

Figure 4.10 depicts the boundary element model representing the region between the two cylinders. A thirty degree segment is isolated, with cyclic symmetry boundary conditions imposed along the edges $\theta = 0^\circ$ and $\theta = 30^\circ$. The inner radius is unity, while an outer radius of two is assumed. Unit values are also taken for the viscosity, density and V . The

model consists of six quadratic elements and two quadratic cells. The cells, of course, are not needed for linear analysis utilizing the convolution approach.

Results of the GPBEST analysis are compared to the exact solution in Figure 4.11 for convolution and in Figure 4.12 for the recurring initial condition algorithm. In both diagrams, results with and without the nonlinear convective terms are plotted. The results are quite good throughout the time history with the convolution approach, while some noticeable error is present at early times for the recurring initial condition solutions. The linear and nonlinear velocity profiles are nearly identical, as expected from the exact solution expressed in (4.35b). However, unlike the previous example, the nonlinear terms do not simply vanish from the integral equation written in cartesian form. Instead, the nonlinear surface and volume integrals must combine in the proper manner to produce the correct solution. Consequently, this problem provides a good test for the entire BEM formulation.

Relative run times are shown in Table 4.2 for the different analysis types. Obviously, the nonlinear convolution approach is very expensive, since this involves volume integration at each time step. As a result, in the general implementation, convolution is only utilized in linear GMRs.

**Table 4.2 - Flow Between Rotating Cylinders
(Run Time Comparisons)**

<u>Analysis Type</u>	<u>Time Marching Algorithm</u>	<u>Relative CPU Time</u>
Linear	Convolution	1.0
Nonlinear	Convolution	25.8
Linear	Recurring Initial Condition	1.5
Nonlinear	Recurring Initial Condition	1.8

4.2.5.5 Driven Cavity Flow

The two-dimensional driven cavity has become the standard test problem for incompressible computational fluid dynamics codes. In a way, this is unfortunate because of the ambiguities in the specification of the boundary conditions. However, numerous results are available for comparison purposes.

The incompressible fluid of uniform viscosity is confined within a unit square region. The fluid velocities on the left, right and bottom sides are fixed at zero, while a uniform nonzero velocity is specified in the x -direction along the top edge. Thus, in the top corners, the x -velocity is not clearly defined. To alleviate this difficulty in the present analysis, the magnitude of this velocity component is tapered to zero at the corners.

Results are presented for the four region, 324 cell boundary element model shown in Figure 4.13. Notice that a higher level of refinement is used near the edges. Spatial plots of the resulting velocity vectors are displayed in Figures 4.14a and b for Reynolds numbers (Re) of 400 and 1000, respectively. Notice that, in particular, the shift of the vortical center follows that described by Burggraf (1966) in his classic paper. A more quantitative examination of the results can be found in Figure 4.15 where the horizontal velocities on the vertical centerline obtained from the present GPBEST analysis are compared to those of Ghia et al (1982). It is assumed that the latter solutions are quite accurate since the authors employed a 129 by 129 finite difference grid. As is apparent, from the figure, all of the solutions are in excellent agreement. Finally, it should be noted that the simple iterative algorithm fails to converge much beyond $Re = 100$. Beyond that range the use of a Newton-Raphson type algorithm is imperative.

In this driven cavity problem, complete volume discretization is required, since the nonlinear convective terms are nonzero throughout the entire domain. As a result, the evaluation of the volume integrals appearing in (4.6) is computationally expensive due to the singular nature of the kernels. Consequently, it is important to investigate the relative merits of a boundary element approach. To aid in this study, a finite element

formulation was developed based primarily on the work of Gartling et al (1977). This finite element implementation utilizes a penalty function approach for incompressibility, along with a Newton-Raphson solution algorithm. An identical sixty-four lagrangian cell model was selected for both the boundary element and finite element analysis. Results are plotted in Figure 4.16 for $Re = 100$. The boundary element results, though more expensive, are significantly more accurate. In fact, at this level of refinement, the finite element results show some oscillation. Clearly, for a given mesh, the boundary integral formulation captures more of the physics. Further comparative studies are planned for the coming months.

4.2.5.6 Transient Driven Cavity Flow

The next example involves the initiation of flow in the same square cavity. An incompressible fluid of uniform density and viscosity is at rest within a unit square region. The velocities of the vertical sides and the bottom are fixed at zero throughout time. At time zero, the horizontal velocity of the top edge is suddenly raised to a value of 1000 and maintained at that level. A gradual transition of velocities is introduced near the top corners to provide continuity.

The four region, 324 cell model shown in Figure 4.13 is employed for the boundary element analysis. The resulting velocity vector plots at several times are shown in Figure 4.17 for this case having a Reynolds number of 1000. The recurring condition algorithm was used. As in the previous two time-dependent examples, the results lead directly to the steady solution after a sufficient number of time steps. This steady solution correlates closely with the results of Ghia et al (1982), as presented in Figure 4.15.

It should be noted that Tosaka and Kakuda (1987) have run the transient driven cavity at $Re = 10,000$. However, their results show signs of instability even at relatively small times, and are compared to the steady solution of Ghia et al which also is not correct at this much higher Reynolds number. A valid solution in this Re range would necessitate the use of an extremely refined mesh, far beyond that employed by Tosaka and Kakuda or Ghia

et al.

4.2.6 Summary

The formulations presented in this section, based upon Stokes fundamental solutions, are suited primarily for low Reynolds number regimes. For creeping flows, all of the nonlinear terms vanish, resulting in a very efficient, very precise boundary-only solution. The resulting boundary element method is clearly superior to any of the domain based methods for problems of this nature, under both steady and transient conditions.

At somewhat higher velocities, the nonlinear convective effects cannot be ignored. Consequently, the surface integral involving t_α^o and the volume integral containing $\sigma_{k\alpha}^o$ in equations (4.6) and (4.11) are required. Since volume integration is quite computationally intensive, a boundary element approach becomes less attractive. This is particularly true when discretization is required throughout the domain, as is the case for confined flows. Still, for a given mesh, the boundary element formulation provides a higher degree of accuracy than finite difference or finite element methods, especially in the determination of boundary quantities.

4.3 Convective Incompressible Thermoviscous Flow

4.3.1 Introduction

At high fluid velocities, the convective terms in Navier-Stokes equations tend to dominate. As a result, boundary element formulations employing Stokes kernels are inappropriate, since these fundamental solutions model the effects of viscosity but not convection. Instead, more of the physics of the problem must be brought into the linear operator. This concept was clearly understood by Oseen in the early portion of the twentieth century. In his 1927 monograph, Oseen developed exact integral expressions for Navier-Stokes equations using a convective fundamental solution. Unfortunately since this was well before the advent of the computer, he was unable to do much with his formulations beyond some approximate solutions at very low Reynolds number. In the present section, the work of

Oseen is resurrected to form the basis for an attractive boundary element method for high speed flows.

4.3.2 Governing Equations

The differential equations, governing the behavior of an incompressible thermoviscous fluid in the presence of a free stream velocity U_i , can be written:

$$\mu \frac{\partial^2 u_i}{\partial x_j \partial x_j} - \frac{\partial p}{\partial x_i} - \rho U_j \frac{\partial u_i}{\partial x_j} - \rho \frac{\partial u_i}{\partial t} + f'_i = 0, \quad (4.38a)$$

$$\frac{\partial u_i}{\partial x_i} = 0, \quad (4.38b)$$

$$k \frac{\partial^2 \theta}{\partial x_j \partial x_j} - \rho c_\epsilon U_j \frac{\partial \theta}{\partial x_j} - \rho c_\epsilon \frac{\partial \theta}{\partial t} + \psi' = 0. \quad (4.38c)$$

where u_i once again represents the velocity perturbation. In (4.38), the effective body forces and sources are defined as

$$f'_i = -\rho u_j \frac{\partial u_i}{\partial x_j} + f_i \quad (4.39a)$$

$$\psi' = -\rho c_\epsilon u_j \frac{\partial \theta}{\partial x_j} + \psi. \quad (4.39b)$$

These equations are of course identical to those presented in (4.4), except that now the convective terms $\rho U_j \partial u_i / \partial x_j$ and $\rho c_\epsilon U_j \partial \theta / \partial x_j$ are included in the linear differential operator. Fundamental solutions based upon (4.38) will contain the character of the flow field at high velocities.

4.3.3 Fundamental Solutions

It is instructive to begin with a look at the fundamental solution of the steady form of the heat equation defined above as (4.38c). In a static medium (i.e., $U_i = 0$), the fundamental solution G must satisfy

$$k \frac{\partial^2 G}{\partial x_j \partial x_j} + \delta(x - \xi) = 0 \quad (4.40)$$

in which δ is the generalized delta function. The solution to (4.40) in two-dimensional space is the well-known potential flow Green's function

$$G(x, \xi) = -\frac{\ln r}{2\pi k} \quad (4.41)$$

with

$$y_i = x_i - \xi_i \quad (4.42a)$$

$$r^2 = y_i y_i \quad (4.42b)$$

Thus, $G(x, \xi)$ represents the temperature response at x due to a unit point heat source at ξ . This response is plotted in the $x_1 - x_2$ plane for a source at the origin in Figure 4.18. Radial symmetry is evident.

However, if the medium is moving at velocity U_i , then the fundamental solution G^U must instead satisfy

$$k \frac{\partial^2 G^U}{\partial x_j \partial x_j} - \rho c_\epsilon U_j \frac{\partial G^U}{\partial x_j} + \delta(x - \xi) = 0 \quad (4.43)$$

Now, the Green's function (e.g. Carslaw and Jaeger, 1947) is given by

$$G^U(x, \xi) = \frac{e^{-U_k y_k / 2\kappa}}{2\pi k} K_0 \left[(U_k U_k)^{1/2} \left(\frac{r}{2\kappa} \right) \right] \quad (4.44)$$

in which $\kappa = k/\rho c_\epsilon$. This response is plotted in Figures 4.19a-d for various magnitudes of an x_1 -directional velocity. Obviously, in a moving medium, radial symmetry is lost and a pronounced front-and-back effect develops. That is, at a given distance from the heat source, it is hottest directly downstream.

It should be emphasized that the so-called convective fundamental solution defined in (4.44) actually embodies both the processes of conduction and convection. At low velocity, conduction dominates producing a nearly radially symmetric response. On the other hand, in a high speed medium, the response is concentrated in a very narrow band downstream of the source. Thus, as illustrated in Figure 4.19, G^U captures the transition from elliptic toward hyperbolic behavior.

The corresponding convective viscous fundamental solution G_{ij}^U was first presented by Oseen (1911), as the solution to

$$\mu \frac{\partial^2 G_{ij}^U}{\partial x_k \partial x_k} - \frac{\partial G_{pj}^U}{\partial x_i} - \rho U_k \frac{\partial G_{ij}^U}{\partial x_k} + \delta_{ij} \delta(x - \xi) = 0 \quad (4.45a)$$

$$\frac{\partial G_{kj}^U}{\partial x_k} = 0. \quad (4.45b)$$

The G_{ij}^U tensor is given in explicit form in Appendix B.4. However, the component G_{11}^U , which represents the velocity in the x_1 -direction due to a unit point force in the x_1 -direction, is displayed in Figures 4.20a-d. For very small U_i , the solution of (4.45) approaches the Stokes kernels detailed in Appendix B.2. This is shown in Figure 4.20a. Notice that, unlike the heat conduction response of Figure 4.19a, the static viscous fundamental solution is not radially symmetric. This is due to the vectorial nature of the flow, and is directly attributed to the $y_i y_j / r^2$ terms in G_{ij} . However, as the flow velocity increases (i.e., Figures 4.20b-d), a stronger sense of upstream and downstream develops, and the response once again becomes concentrated in a narrow band ahead of the applied force. At high speed, outside of this band, the response is essentially zero. This behavior is not only important from a physical standpoint, but also can be beneficial in the development of efficient boundary element algorithms.

4.3.4 Integral Representations

The convective fundamental solutions depicted in Figures 4.19 and 4.20 capture the proper character of high Reynolds number incompressible thermoviscous flows, and as a result, can provide the basis for an attractive boundary element formulation. The corresponding integral equations, under steady conditions, can be developed directly from the governing differential equations (4.38). This result is,

$$c_{\alpha\beta}u_\alpha = \int_S [G_{\alpha\beta}^U t_\alpha - F_{\alpha\beta}^U u_\alpha - G_{\alpha\beta}^U t_\alpha^{U_o}] dS + \int_V [D_{\alpha\beta k}^U \sigma_{k\alpha}^{U_o} + G_{\alpha\beta}^U f_\alpha] dV, \quad (4.46)$$

where

$$\sigma_{k\alpha}^{U_o} = [\rho u_k u_i \quad \rho c_\epsilon u_k \theta] \quad (4.47a)$$

$$t_\alpha^{U_o} = \sigma_{k\alpha}^{U_o} n_k. \quad (4.47b)$$

the superscript U on the kernel functions is a reminder that these are based upon convective fundamental solutions. All of the kernels appearing in (4.46) are detailed in Appendix B.4.

In most cases the body forces, f_α , are either zero or can be accounted for via a particular integral so that the second volume integral in (4.46) is not needed.

In examining (4.46), it should be noted that the nonlinearities are contained in the surface integral involving $G_{\alpha\beta}^U t_\alpha^{U_o}$ and the remaining volume integral, $D_{\alpha\beta k}^U \sigma_{k\alpha}^{U_o}$. Specifically, only $t_\alpha^{U_o}$ and $\sigma_{k\alpha}^{U_o}$ are nonlinear, and these are both formed from the product of perturbations. For high speed flows, these perturbations are only significant in the vicinity of objects and in the wake. As a result, volume discretization is only needed in those areas. Elsewhere, the linearized Oseen approximation is adequate.

Equation (4.46) is identical to the integral equation developed by Oseen (1927), except for the treatment of the nonlinear convective terms. In deriving (4.46), an additional integration-by-parts operation was invoked to completely eliminate the appearance of velocity gradients.

If one is interested in the transient thermoviscous response in a medium with a more or less steady free stream velocity, then a time-dependent formulation is also possible. For this case, the time derivatives are retained in the linear operator, and the following integral equation results:

$$c_{\alpha\beta} u_\alpha = \int_S [g_{\alpha\beta}^U * t_\alpha - f_{\alpha\beta}^U * u_\alpha - g_{\alpha\beta}^U * t_\alpha^{U_o}] dS + \int_V [d_{\alpha\beta k}^U * \sigma_{k\alpha}^{U_o} + g_{\alpha\beta}^U * f_\alpha - g_{\alpha\beta}^U \rho u_\alpha^o] dV \quad (4.48)$$

This integral equation and the corresponding fundamental solutions have not appeared in the literature. The functions $g_{\alpha\beta}^U$ are quite involved, but can be expressed in terms of incomplete exponential integrals. Details will be presented next year.

4.3.5 Numerical Implementation

The integral representations for convective thermoviscous flow are quite similar to those presented in Section 4.2.3. Consequently, there is a great deal of overlap in the algorithms employed for their respective numerical implementation. At present, the major difference occurs in the schemes utilized for integration.

As discussed previously, the convective fundamental solutions have a much different character than the more familiar Stokes based kernels. The standard boundary element integration schemes are unable to accurately capture the localized nature of the convective kernels, particularly at large Reynolds number. In general, subsegmentation must be much more intense for singular and near-singular cases. For example, in convective near-singular integration, first the location X° on the element nearest to the load point ξ is identified. Then, a graded subsegmentation pattern is defined about X° based upon criteria including the distance of ξ to X° and the free stream velocity. For higher speed flow, smaller subsegments are generated. Gaussian integration order is also typically higher for the convective surface integration. Similar adjustments are required for volume integration as well.

During this past year, some progress has been made in the development of alternate integration strategies for singular integration. For example, partial analytical treatment of the G_{ij}^U kernel has proved to be more cost effective. Also, the standard ‘rigid body’ technique has been extended to other known solution fields in order to indirectly calculate some of the singular contributions.

However, additional effort is still needed to develop integration algorithms designed specifically for high speed convective kernels. In particular, the response depicted in Figure 4.20d must be anticipated. Thus, there is no need to integrate an element which lies outside the narrow band of nonzero response. Furthermore, elements located partially or wholly within the band should be subsegmented accordingly.

The remainder of the numerical implementation follows that discussed in Section 4.2.4. Thus, assembly, solution, and the calculation of additional boundary quantities are accomplished in the same manner as for the Stokes kernel approach. While this is perfectly legitimate, full advantage has not yet been taken of the character of the convective response. For example, at very high speeds, as the behavior becomes hyperbolic, the system equations form a nearly-sequential, banded set. The present assembler and solver, which

were designed for elliptic systems, do not recognize this structure, and consequently, are quite inefficient.

4.3.6 Numerical Examples

4.3.6.1 Introduction

In order to thoroughly study the effectiveness of a boundary element approach for high speed flows, the above convective formulations were implemented as a segment of a state-of-the-art general purpose boundary element code. In the following, several numerical examples are presented. These examples are intended to validate the formulations, and to suggest the potential advantages of using a boundary element method for this class of problems.

4.3.6.2 Burgers Flow

The classic uniaxial linear Burgers problem provides an excellent test of the convective thermoviscous formulations. The incompressible fluid flows in the x -direction with uniform velocity U . Meanwhile, the y -component of the velocity and temperature are specified as U_o and T_o , respectively, at inlet. Both are zero at the outlet. The length of the flow field is L . The analytical solution (Schlichting, 1955) is

$$V_y = \zeta U_o$$

$$T = \zeta T_o$$

where

$$\zeta = \left\{ 1 - \exp \left[R_L \left(\frac{x}{L} - 1 \right) \right] \right\} / \{ 1 - \exp [-R_L] \}$$

with $R_L = UL$.

The boundary element model employs eighteen quadratic surface elements encompassing the rectangular domain. The elements are graded, providing a very fine discretization near the exit, where V_y and T vary substantially for large R_L . Results are shown in Figure

4.21 for the thermal problem and in Figure 4.22 for the viscous problem. Excellent correlation with the analytical solution is obtained in both instances for this boundary-only analysis, even for the highly convective case of $R_L = 1000$. The portion of the flow field just ahead of the outlet is examined more closely in Figure 4.23. The convective Oseen solution obviously produces a precise solution. This problem can also be solved by utilizing the Stokes kernels and volume cells. As seen in Figure 4.23, this latter approach is not quite as accurate. It should be noted that traditionally finite difference and finite element methods have a difficult time dealing with the convective terms present in this problem. Generally, ad hoc upwinding techniques must be introduced to produce stable, accurate solutions. On the other hand, with the convective boundary element approach the kernel functions contain an analytical form of upwinding. As a result, very precise BEM results can be obtained.

4.3.6.3 Flow Over a Cylinder

As the next convective fluids example, the oft-studied case of incompressible flow over a circular cylinder is considered. Initially for this problem, both the steady convective and non-convective formulations are utilized in the same analysis. The boundary element model is displayed in Figure 4.24. Note that half-symmetry is imposed. In the inner region, the Stokes kernels are employed along with a complete volume discretization. Thus, the complete Navier-Stokes equations are represented. The outer region uses the Oseen kernels with a boundary-only formulation. The small non-linear contributions that would be present in the outer region away from the cylinder are ignored. For those more familiar with finite elements, each region can be thought of as a substructure or superelement. However, the outer region does not require a volume mesh.

The steady-state velocity vector plot at $Re = 40$ is shown in Figure 4.25. The recirculating zone, behind the cylinder, is clearly visible. Additionally, the resulting drag coefficient (C_D) of 1.8 obtained from the BE analysis is within the band of experimental scatter as presented by Panton (1984) for the circular cylinder.

Similarly, a transient analysis can be conducted. Now a full mesh as shown in Figure 4.26 is employed. The inner region uses a time-dependent nonlinear Stokes formulation, while linear Oseen kernels provide the basis for the outer infinite region. Results are shown in Figure 4.27a for $Re = 100$ at a time for which the flow is nearly fully developed. Meanwhile, Figure 4.27b present the solution at the same time, but with a different angle of attack for the oncoming fluid. The results are virtually identical. This illustrates the relative insensitivity of boundary element solutions to the cell discretization pattern. The reason for this behavior, which is particularly important in modeling hyperbolic phenomena, is that so much of the boundary element formulation is analytical. Another item to note from these results is the completely symmetric flow patterns that were obtained. Asymmetry would have to be induced by perturbing either the geometry, the free stream velocity or the boundary conditions.

While all of this is encouraging, the development of a simplified procedure involving far less volume discretization is desirable. For example, a completely linear Oseen analysis, which ignores all nonlinear convective terms in both regions, produces a very similar solution, except in the vicinity of the cylinder. Vector plots from the nonlinear analysis and the boundary-only linear Oseen analysis are superimposed in Figure 4.28. Although it is difficult to distinguish between the two analyses in that plot, both produce a recirculatory zone behind the cylinder. Thus, the main features of the problem are captured by the boundary-only analysis. However, the linear solution, in general, overstates the velocities and velocity gradients in the neighborhood of the cylinder. Consequently, a drag coefficient of 3.4 is calculated, which is much higher than that found experimentally. This trend, of overpredicting the experimental drag, continues even to much higher Reynolds numbers as shown in Figure 4.29. Qualitatively, however, the behavior of the BEM Oseen solution is consistent with the experimental curve for Reynolds Numbers up to 100,000.

A much improved solution can be obtained by introducing a row of cells encompassing the cylinder. The full nonlinear Navier-Stokes equations are solved within this inner region

which includes an inner and outer ring of surface elements. Exterior to the outer ring is a linear Oseen region. This exterior region consists simply of one matching ring of surface elements. Its volume extends outward to infinity, where the velocity reaches its free stream value. Figure 4.30 illustrates a typical mesh, along with the resulting velocity vectors. As Reynolds number is increased, the significant nonlinear effects concentrate nearer to the cylinder, so that the thickness of the inner region may be reduced. Figure 4.29 also displays the drag obtained by utilizing just a single row of cells. Results are quite encouraging.

An alternative approach for high speed flows involves the conversion of the nonlinear volume integral into effectively a surface integral by introducing a suitable perturbation velocity decay function. If this is accomplished then even a nonlinear analysis reduces to a boundary-only solution algorithm. A concerted effort will be made in this direction during the coming year.

4.3.6.4 Flow Past Airfoils

For illustrative purposes, a boundary-only thermoviscous analysis was conducted for convective flow around a pair of NACA-0018 airfoils. The boundary element model of the blades is shown in Figure 4.31. A hot fluid at unit temperature flows from left to right with a unit magnitude of the free stream velocity. Meanwhile, the airfoils are assumed to be stationary with their outer surface maintained at zero temperature.

It should be emphasized that this problem was run as a boundary-only analysis, however, a number of sampling points were included in the fluid surrounding the airfoils in order to graphically portray the response. First the thermal solution is examined. Figure 4.32a depicts the temperature distribution in the fluid at a Peclet (Pe) number of ten, where $Pe = UL/\kappa$, with fluid velocity U , thermal diffusivity κ and airfoil chord length L . Meanwhile, Figures 4.32b-d show the response at progressively higher Peclet number. At $Pe = 10000$, quartic surface elements were required in order to obtain an accurate solution. The strong convective character is quite noticeable at larger Pe as the effect of the cold airfoils is swept downstream. Also, in Figures 4.32c and d there is virtually no interaction

between the airfoils. This type of behavior is expected from a physical standpoint. It occurs in the analysis because of the banded nature of the convective fundamental solutions illustrated previously (e.g., Figure 4.19). However, interaction will take place if the angle of attack is altered. Figure 4.32e shows the response at a 30° angle for $Pe = 1000$.

The velocity distribution around the airfoils follows a similar pattern. For these results displayed in Figure 4.33, Reynolds number is defined by $Re = \rho UL/\mu$. In these plots, the magnitude of the velocity, obtained from a boundary-only solution, is contoured. These results feature somewhat more interaction particularly upstream of the airfoils. It should be emphasized that even though a linearized solution algorithm is employed the so-called phenomenon of boundary layer separation can still occur. Figure 4.34 focuses on the rear portion of the upper blade. The contour line demarks the transition from positive to negative streamwise velocity, and thus very nearly identifies the point of separation.

Next, a second row of blades is added. The modeling effort for this extension is quite trivial, since there is actually no discretization required beyond that needed to describe the airfoil surfaces. For this problem, four vertical sections of one hundred sampling points were included for display purposes. Velocity vectors across those sections are plotted in Figures 4.35 and 4.36 for Reynolds numbers of 10000 and 100000, respectively. The vertical spacing between the airfoils increases as one examines a through c in these two diagrams. The velocity profiles are noticeably affected by that spacing. However, in all of the plots significant velocity gradients are present. It is interesting to consider the level of refinement that would be necessary in a domain based finite difference or finite element analysis in order to capture similar gradients.

4.3.7 Summary

A new methodology has been presented for the solution of high Reynolds number incompressible thermoviscous flow. The convective fundamental solutions that lie at the heart of these methods model both the diffusive character of viscosity as well as the hyperbolic nature of convection. This is accomplished analytically, independent of any dis-

cretization pattern. Consequently, the resulting boundary element formulations are quite attractive particularly for higher speed unconfined flows.

Solutions obtained for the cylinder compare favorably with experimental data. Results presented in Figures 4.32-4.36 for the airfoils appear to be reasonable, although these are not solutions to the complete Navier-Stokes equations. In particular, all terms of second order in the perturbation velocities have been ignored. For high speed flows, these solutions can be improved by including some cells in the thin boundary layer surrounding the airfoils and in the wake. It is not necessary to capture all of the intricacies of the flow field in order to obtain good engineering information on the surface of the airfoil.

Further work is still needed in order to produce an effective analysis tool. For example, several promising alternatives for the representation of the nonlinear terms must be explored, and an intensive effort is required toward the development of efficient numerics tailored for the structure of the convective formulations. The latter effort should be directed toward algorithms for massively parallel machines, which provide an ideal setting for boundary element processing.

4.4 Compressible Thermoviscous Flow

4.4.1 Introduction

Several of the previous examples have demonstrated the potential of the convective incompressible boundary integral formulation for flows in the high Reynolds number range. However, more generally, at very high speeds, compressibility of the fluid must also be considered. In particular, shock-related phenomena are not present in the incompressible formulations and kernel functions. To correct this deficiency, a compressible thermoviscous integral formulation is presented in this section. It should be noted that, while Oseen derived most of the fundamental solutions required for the incompressible case, no such similar solutions are available for compressibility. Consequently, considerable time and effort was required to derive these new approximate infinite space Green's functions.

4.4.2 Governing Equations

The conservation laws of mass, momentum and energy for a compressible thermoviscous fluid can be written in the following form

$$-\rho \frac{\partial v_i}{\partial x_i} - \frac{D\rho}{Dt} + \phi = 0 \quad (4.49a)$$

$$(\lambda + \mu) \frac{\partial^2 v_j}{\partial x_j \partial x_i} + \mu \frac{\partial^2 v_i}{\partial x_j \partial x_j} - \frac{\partial p}{\partial x_i} - \rho \frac{Dv_i}{Dt} + f_i = 0 \quad (4.49b)$$

$$k \frac{\partial^2 \theta}{\partial x_j \partial x_j} - \rho c_\epsilon \frac{D\theta}{Dt} - p \frac{\partial v_i}{\partial x_i} + \psi = 0 \quad (4.49c)$$

where ϕ is a mass source and λ is a second viscosity coefficient. All other quantities are defined in Section 4.2.2. Reference values for each of the primary variables are introduced in an effort to produce a linearized differential operator. Thus, let

$$v_i = U_i + u_i \quad (4.50a)$$

$$p = p_o + \bar{p} \quad (4.50b)$$

$$\theta = \theta_o + \bar{\theta} \quad (4.50c)$$

$$\rho = \rho_o + \bar{\rho}, \quad (4.50d)$$

in which U_i , p_o , θ_o , and ρ_o are constant reference values, and u_i , \bar{p} , $\bar{\theta}$ and $\bar{\rho}$ are the perturbations. Plugging these definitions into (4.49) produces, after some manipulation,

$$-p_o \frac{\partial u_i}{\partial x_i} - \frac{D_o \bar{p}}{Dt} + \phi' = 0 \quad (4.51a)$$

$$(\lambda + \mu) \frac{\partial^2 u_j}{\partial x_j \partial x_i} + \mu \frac{\partial^2 u_i}{\partial x_j \partial x_j} - \frac{d\bar{p}}{\partial x_i} - \rho_o \frac{D_o u_i}{Dt} + f'_i = 0 \quad (4.51b)$$

$$k \frac{\partial^2 \bar{\theta}}{\partial x_j \partial x_j} - \rho_o c_\epsilon \frac{D_o \bar{\theta}}{Dt} + \psi' = 0 \quad (4.51c)$$

where ϕ' , f'_i , and ψ' are now modified body mass sources, forces, and heat sources. Also, in (4.51),

$$\frac{D_o}{Dt} = \frac{\partial}{\partial t} + U_i \frac{\partial}{\partial x_i}. \quad (4.52)$$

A set of approximate fundamental solutions to (4.51) were given in the previous annual report (Dargush and Banerjee, 1989c). However, those solutions had two major deficiencies. Firstly, the phenomenon of shock was not portrayed as expected from a physical standpoint, and secondly, the order of the kernel singularities was too high.

During the current year, these fundamental solutions were abandoned. Instead, attention was redirected toward idealizing the physical process as a combination of vortical and dilatational motion. The vortical component is dominated by viscosity and convection, and is identical for both compressible and incompressible flows. On the other hand, the dilatational component must respond elastically within a convective medium. Viscous damping is also present.

These considerations lead to a redevelopment of the mass conservation equation exclusively in terms of pressure. The resulting governing equations become

$$c^2 \frac{\partial^2 \bar{p}}{\partial x_j \partial x_j} + \eta \frac{D_o}{Dt} \frac{\partial^2 \bar{p}}{\partial x_j \partial x_j} - \frac{D_o^2 \bar{p}}{Dt^2} + \Omega' = 0 \quad (4.52a)$$

$$(\lambda + \mu) \frac{\partial^2 u_j}{\partial x_j \partial x_i} + \mu \frac{\partial^2 u_i}{\partial x_j \partial x_j} - \frac{d\bar{p}}{\partial x_i} - \rho_o \frac{D_o u_i}{Dt} + f'_i = 0 \quad (4.52b)$$

$$k \frac{\partial^2 \bar{\theta}}{\partial x_j \partial x_j} - \rho_o c \epsilon \frac{D_o \bar{\theta}}{Dt} + \psi' = 0 \quad (4.52c)$$

where c is the speed of sound.

4.4.3 Fundamental Solutions

The steady two-dimensional infinite space fundamental solutions of (4.52), derived by Shi (1991), are presented in Appendix B.5. Since the algebraic form of these kernels is so complicated it is best to examine the behavior graphically. For this exercise, a forty-by-forty grid of sampling points was generated as shown in Figure 4.37. The source point is fixed at the origin, located as the central point in the grid.

First, the component G_{11} is plotted for various free stream velocities, expressed in terms of Mach number, in Figure 4.38. (Recall that G_{11} is the velocity in the x_1 -direction at the sampling point due to a unit point force in the x_1 -direction at the origin.) The

response has some similarity to that for incompressible flow displayed in Figure 4.20. As the magnitude of the free stream velocity increases, a pronounced sense of flow direction becomes evident with the nonzero response concentrating in a narrow band ahead of the applied force. However, the response is always continuous, and there is a gradual evolution from the elliptic form at low velocity to the near-hyperbolic behavior in quickly moving streams.

On the other hand, the character of G_{pp} , representing the pressure response due to a unit source, is much different. At a zero Mach number, the pressure is radially symmetric as seen in Figure 4.39a. Increasing the Mach number to 0.9 produces a transition to the, by now, familiar convective form. However, at $M = 1$, the field suddenly becomes singular. Figure 4.39c shows a distinctive Mach cone at $M = 1.1$. It should be noted that the analytical kernels of Appendix B.5 produce absolutely straight lines defining the cone. Unfortunately, the graphics package is unable to accurately portray the discontinuity. As the Mach number increases further, the included angle of the cone decreases. The response at $M = 8$ is displayed in Figure 4.39d.

Finally, Figure 4.40 shows the coupling term G_{1p} , which measures the velocity in the x_1 -direction due to a unit source. This term also exhibits the shock-related Mach cone, however, now there is additionally evidence of some viscous damping of the response.

4.4.4 Integral Representations

The formal appearance of the governing integral equations for steady compressible thermoviscous flow is very similar to that provided in Section 4.3.4. Specifically, let

$$c_{\alpha\beta}u_{\alpha} = \int_S [G_{\alpha\beta}^U t_{\alpha} - F_{\alpha\beta}^U u_{\alpha}] dS + \int_V [G_{\alpha\beta}^U f'_{\alpha}] dV$$

where now

$$u_{\alpha} = \{u_1 \quad u_2 \quad \bar{p} \quad \bar{\theta}\}$$

$$t_{\alpha} = \{t_1 \quad t_2 \quad \partial \bar{p} / \partial n \quad q\}$$

$$f'_{\alpha} = \{f'_1 \quad f'_2 \quad \Omega' \quad \psi'\}.$$

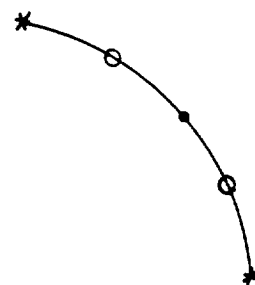
The major difference is, of course, in the kernel functions $G_{\alpha\beta}^U$ and $F_{\alpha\beta}^U$.

4.4.5 Summary

New fundamental solutions were derived for compressible thermoviscous flow during this past year. The two-dimensional steady form is given in Appendix B.5, however solutions were also obtained for the transient case, and for three-dimensional domains. The contour plots of Figure 4.38 through 4.40 suggest that this latest effort has produced physically meaningful kernel functions.

Although the numerical implementation of the compressible formulation has not yet been undertaken, a couple of characteristics of the boundary element approach should be noted. For high speed flows, the nonlinearities will once again be concentrated in a thin layer near the surface and in the wake. Thus, all of the discussion concerning high Re incompressible flow is valid here as well. Furthermore, with compressibility comes the hyperbolic phenomenon of shock. In a boundary element approach, the discontinuity can be captured analytically through the fundamental solution. It is not necessary to use a mesh to model the, generally unknown, location of the shock front. This is a distinct advantage for boundary elements over the domain-based methods.

FIGURE 4.1 TWO-DIMENSIONAL BOUNDARY ELEMENTS



GEOMETRIC NODES (*,●) 3

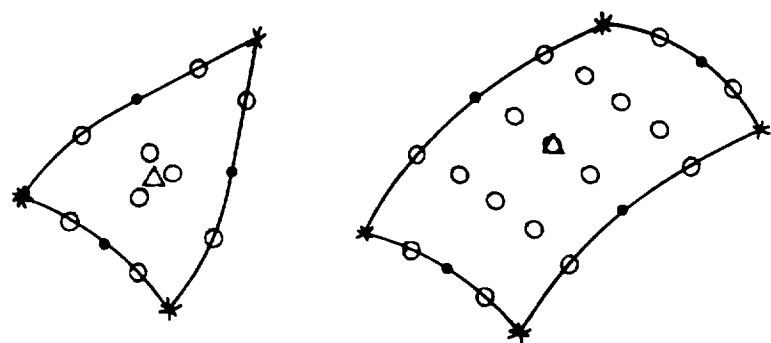
FUNCTIONAL NODES

LINEAR (*) 2

QUADRATIC (*,●) 3

QUARTIC (*,●,○) 5

FIGURE 4.2 TWO-DIMENSIONAL VOLUME CELLS



GEOMETRIC NODES (*, ·)	6	8
FUNCTIONAL NODES		
LINEAR (*)	3	4
QUADRATIC		
SERENDIPITY (*, ·)	6	8
LAGRANGIAN (*, ·, Δ)	7	9
QUARTIC (*, ·, o)	15	25

FIGURE 4.3 - INTEGRATION SUBSEGMENTATION

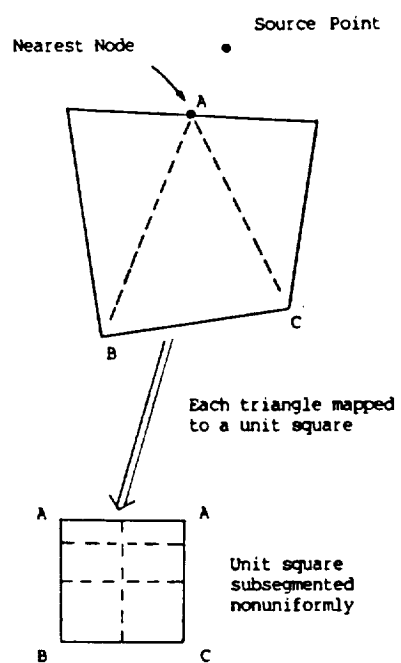


FIGURE 4.4a - CONVERGING CHANNEL

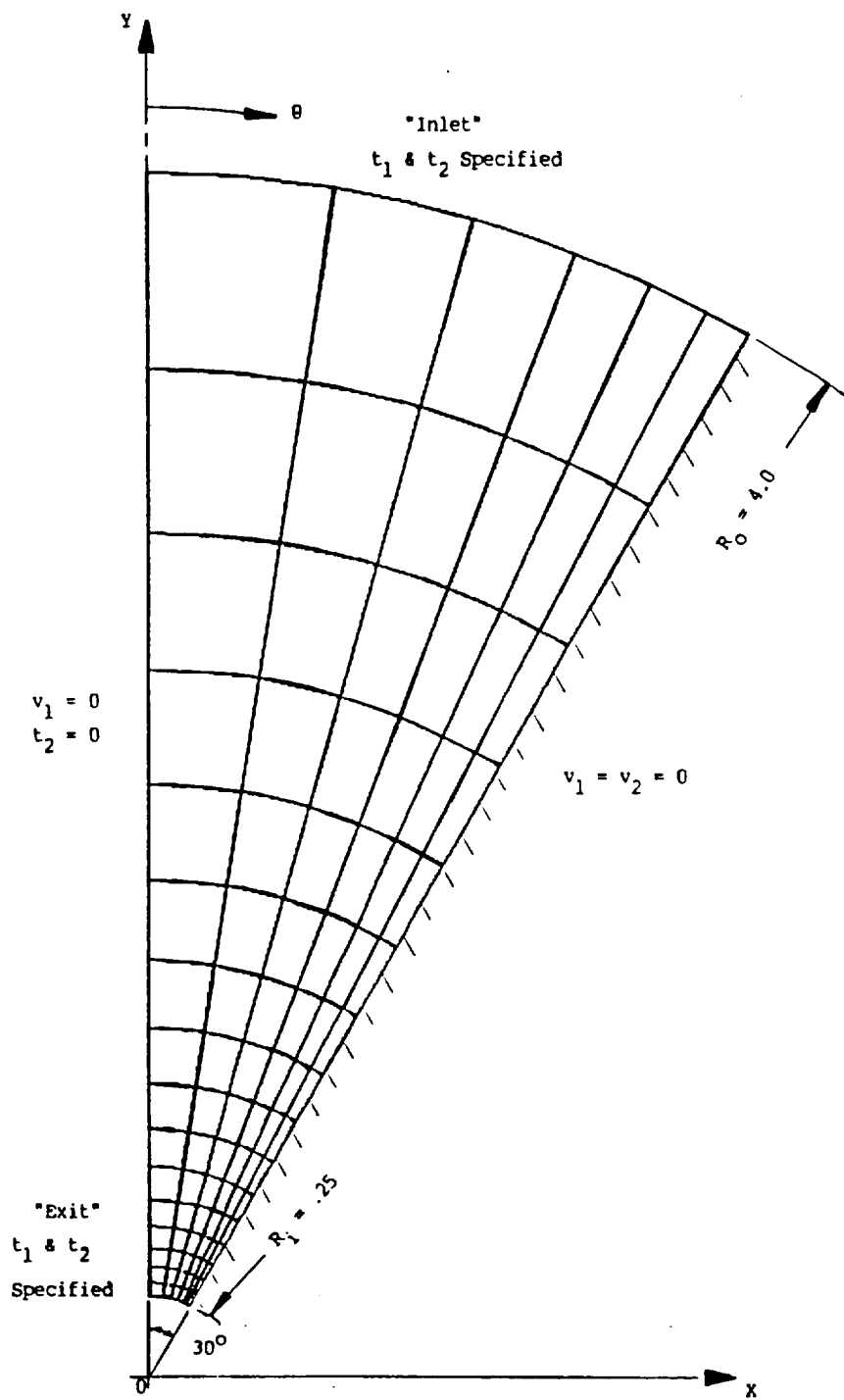


FIGURE 4.4b - CONVERGING CHANNEL

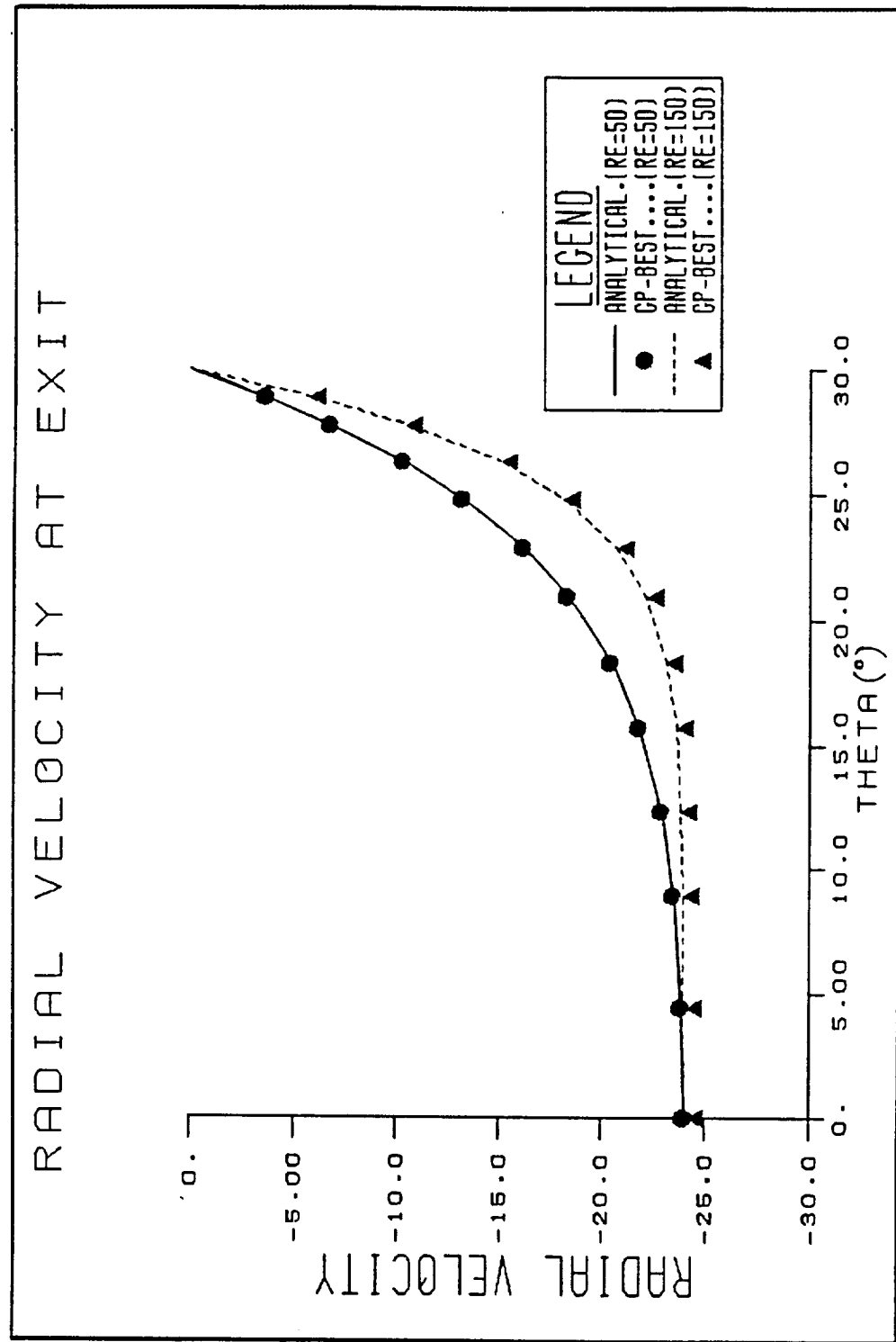


FIGURE 4.5

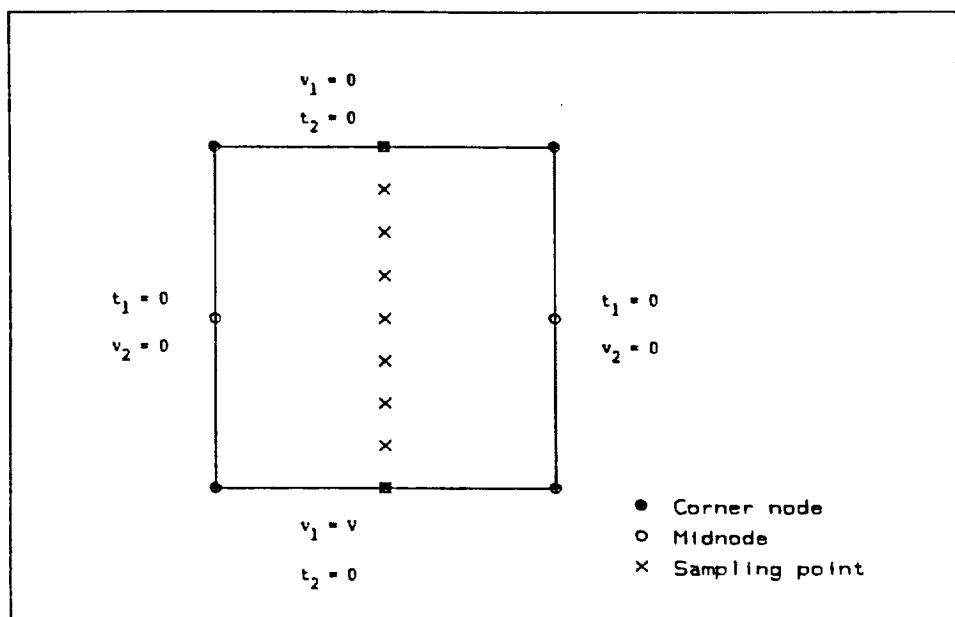
TRANSIENT COUETTE FLOW
Boundary Element Model

FIGURE 4.6

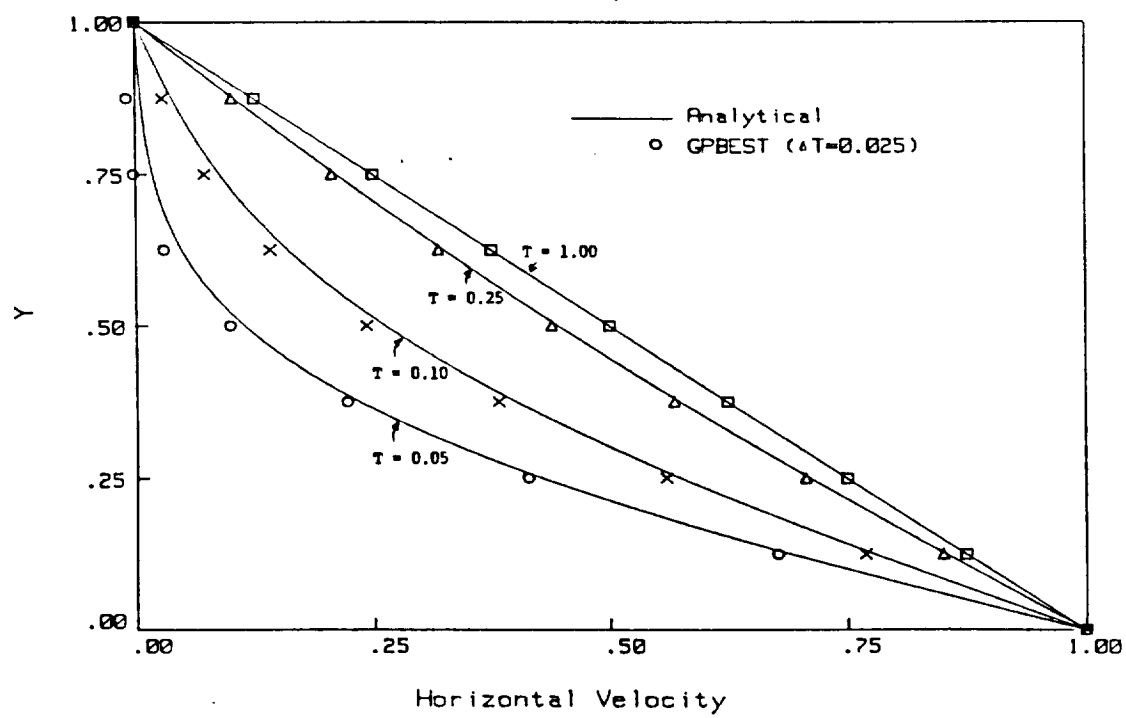
TRANSIENT COUETTE FLOW
Velocity Profile

FIGURE 4.7

TRANSIENT COUETTE FLOW

Convolution

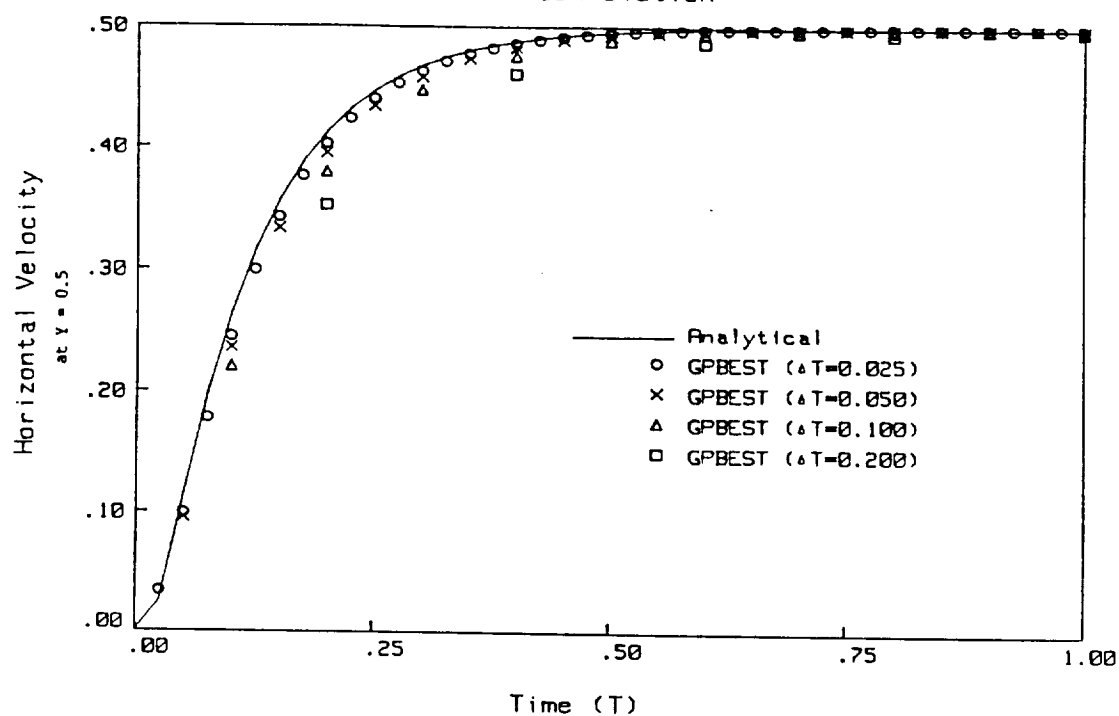


FIGURE 4.8

TRANSIENT COUETTE FLOW

Convolution - Refined Model

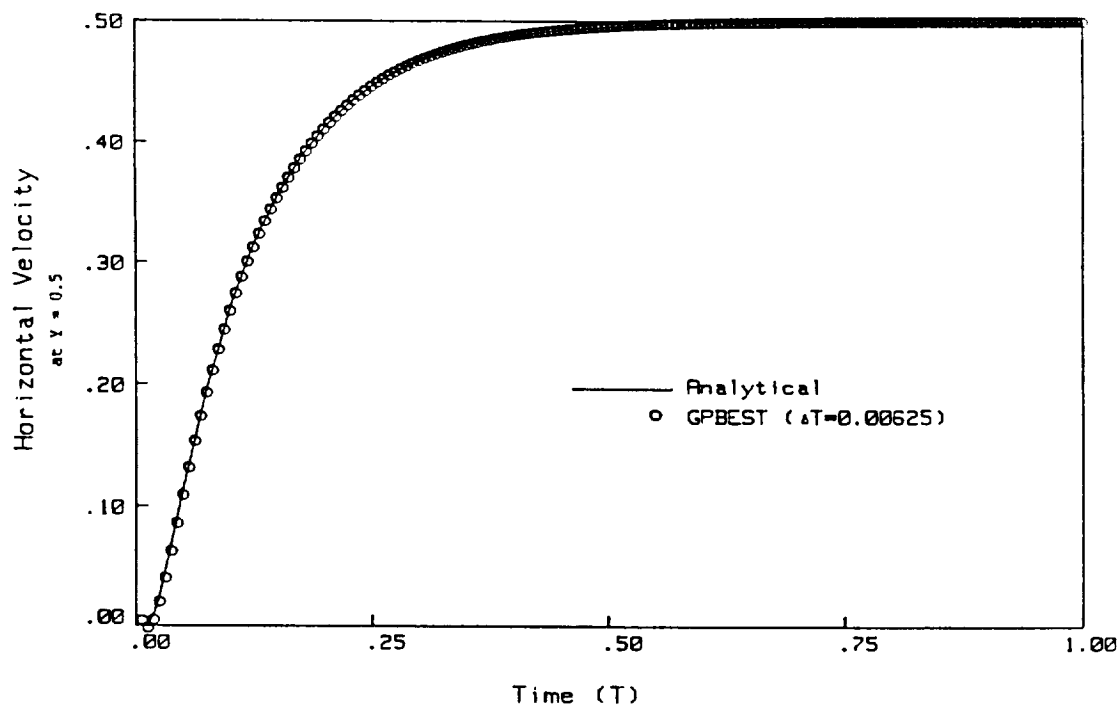


FIGURE 4.9

TRANSIENT COUETTE FLOW

Recurring Initial Condition

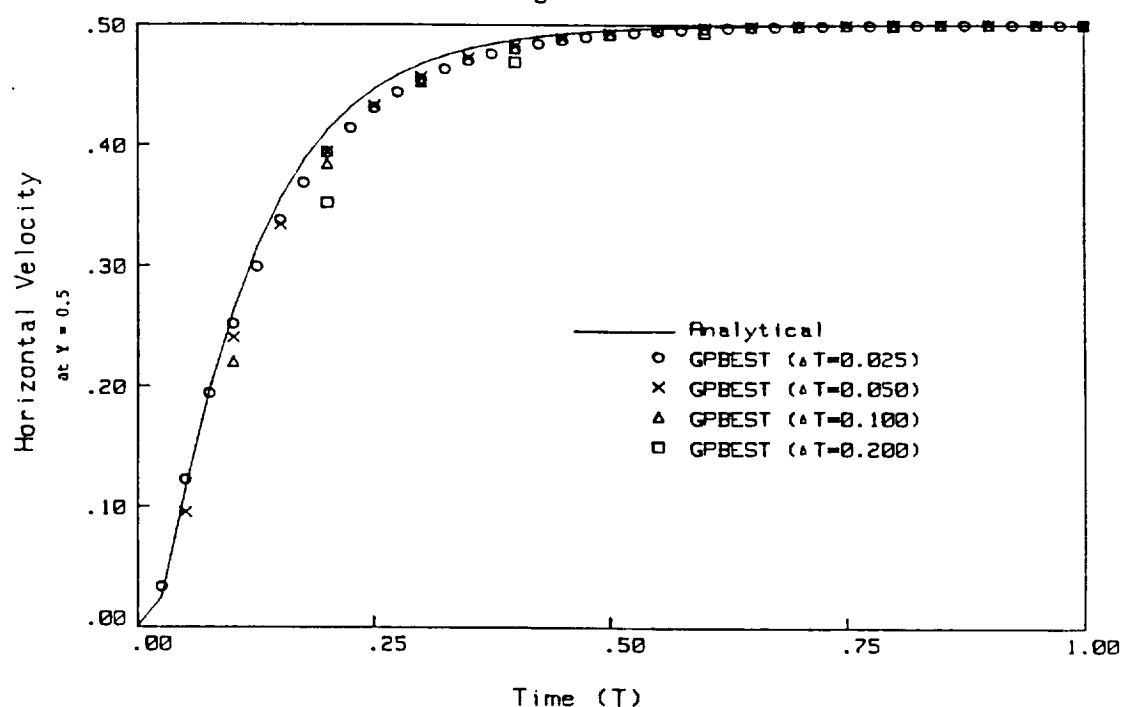


FIGURE 4.10

FLOW BETWEEN ROTATING CYLINDERS

Boundary Element Model

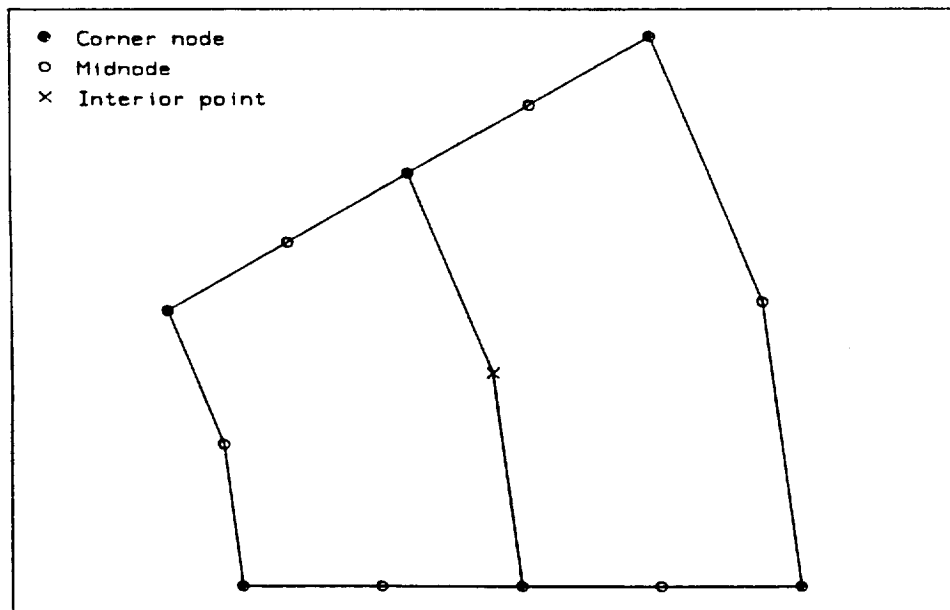


FIGURE 4.11
FLOW BETWEEN ROTATING CYLINDERS

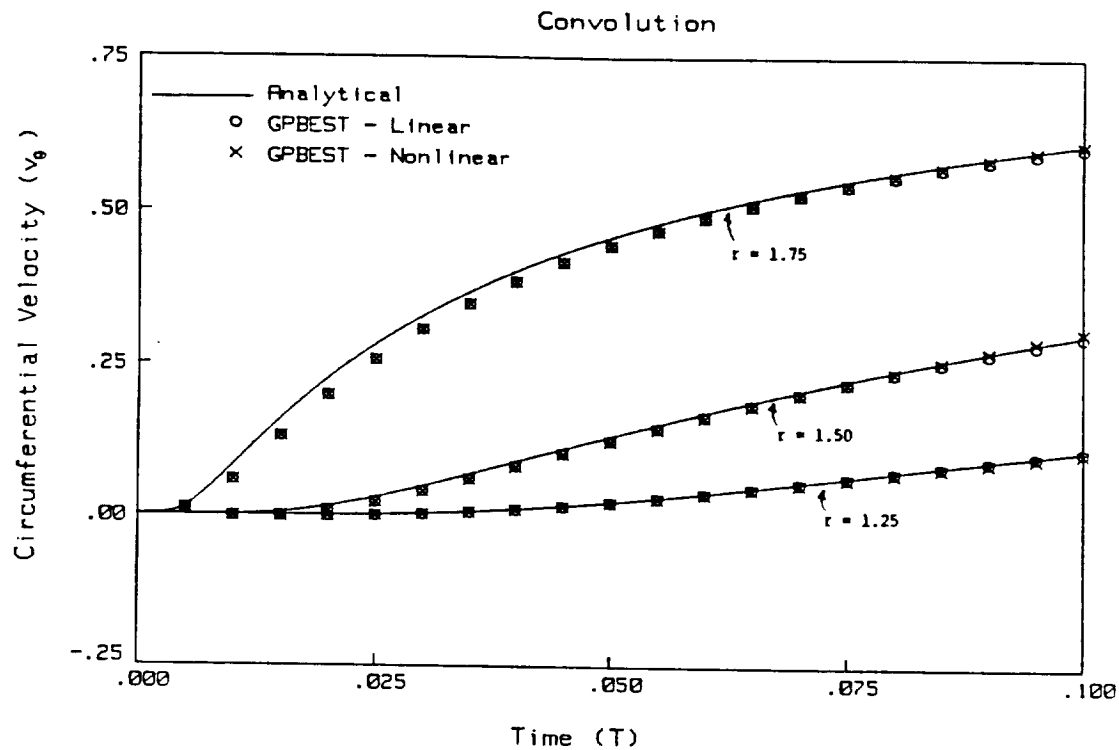


FIGURE 4.12
FLOW BETWEEN ROTATING CYLINDERS

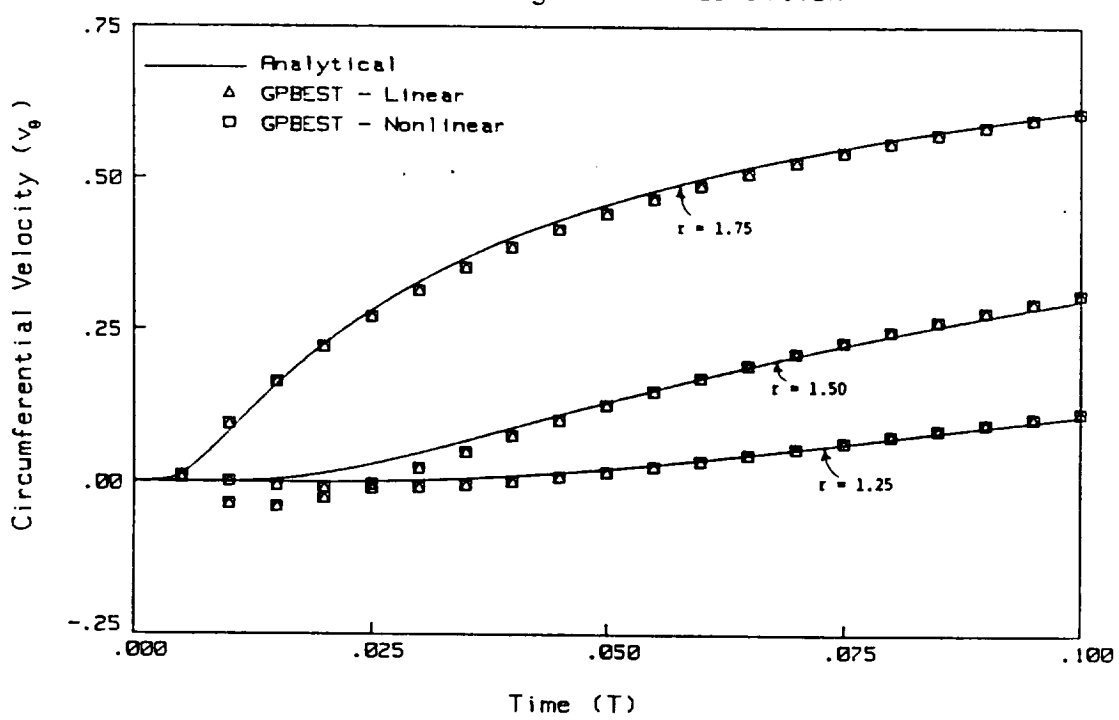


FIGURE 4.13

DRIVEN CAVITY – FOUR REGION MODEL

Boundary Element Model

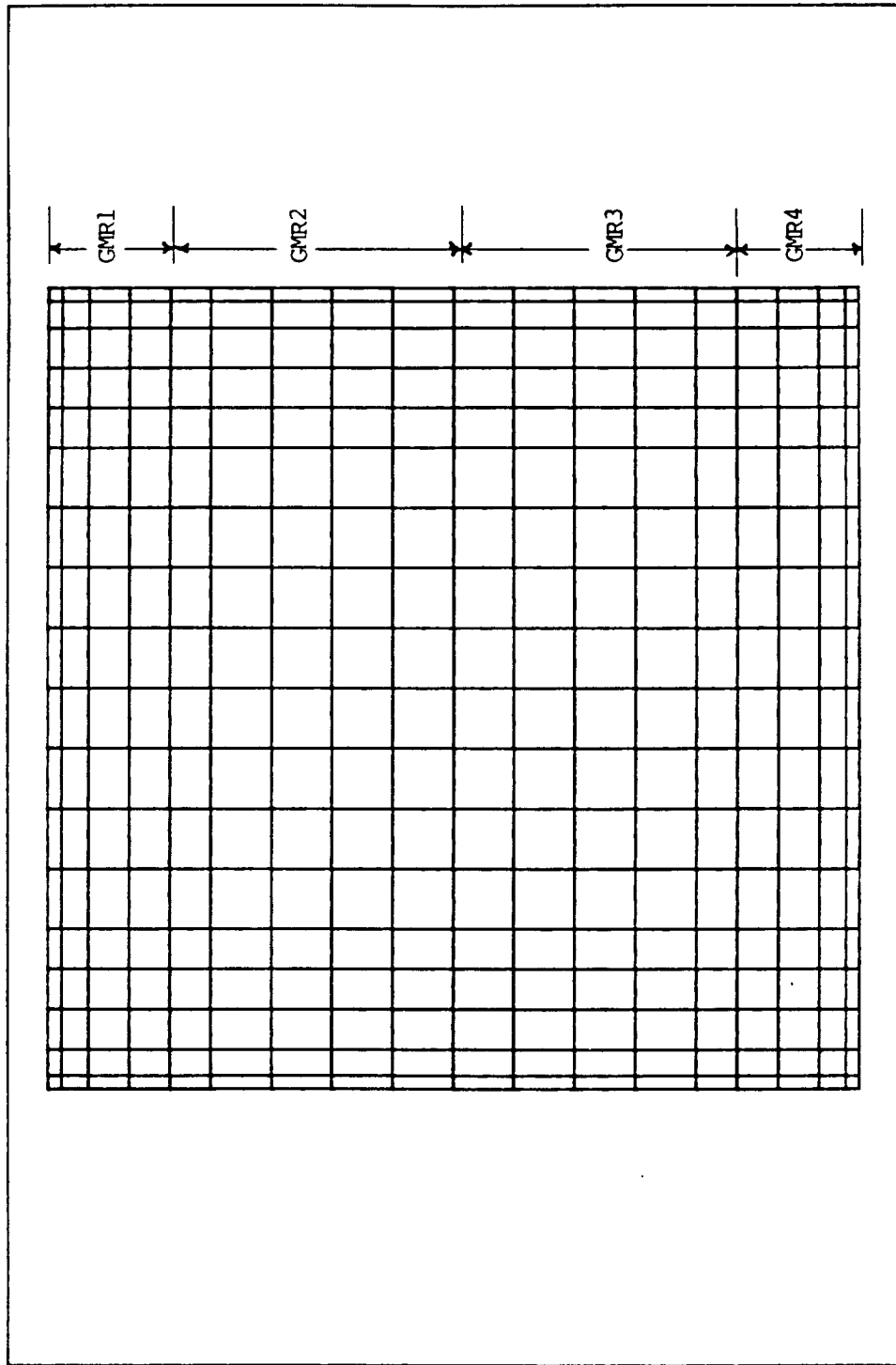
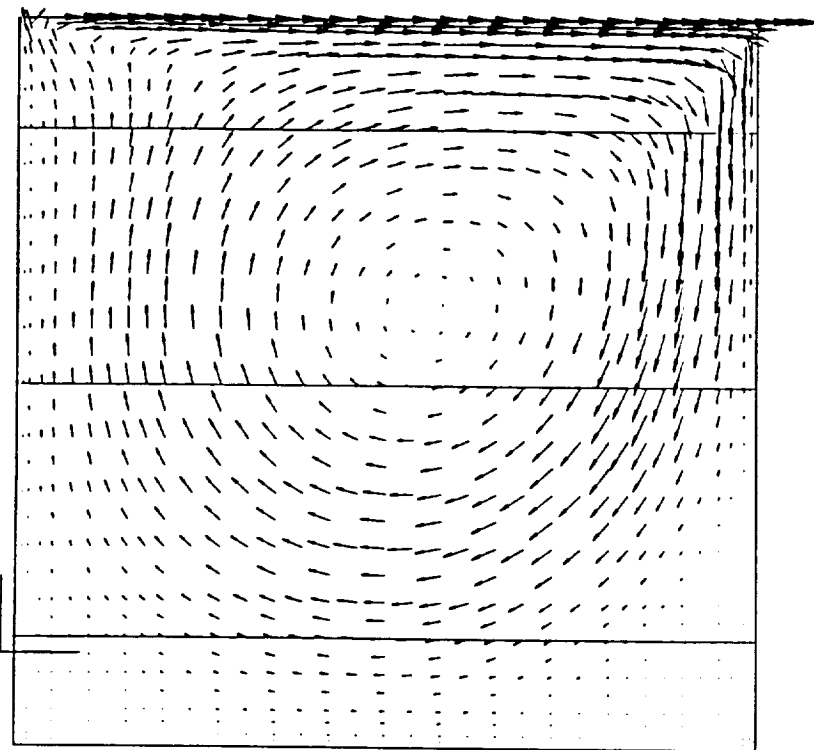
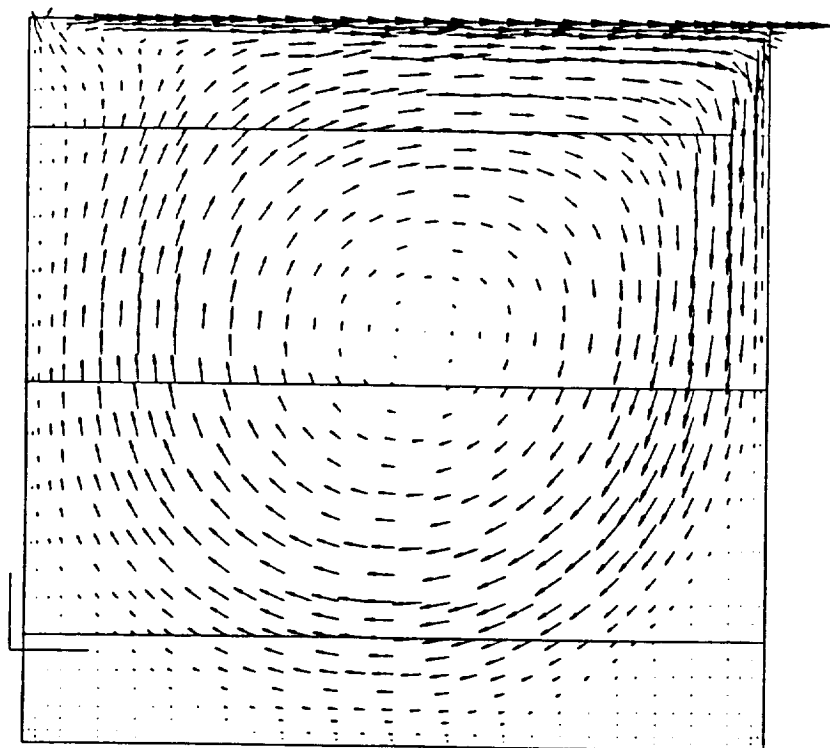


FIGURE 4.14 - DRIVEN CAVITY FLOW



a) $Re = 400$



b) $Re = 1000$

FIGURE 4.15

DRIVEN CAVITY - FOUR REGION MODEL
VELOCITY PROFILE

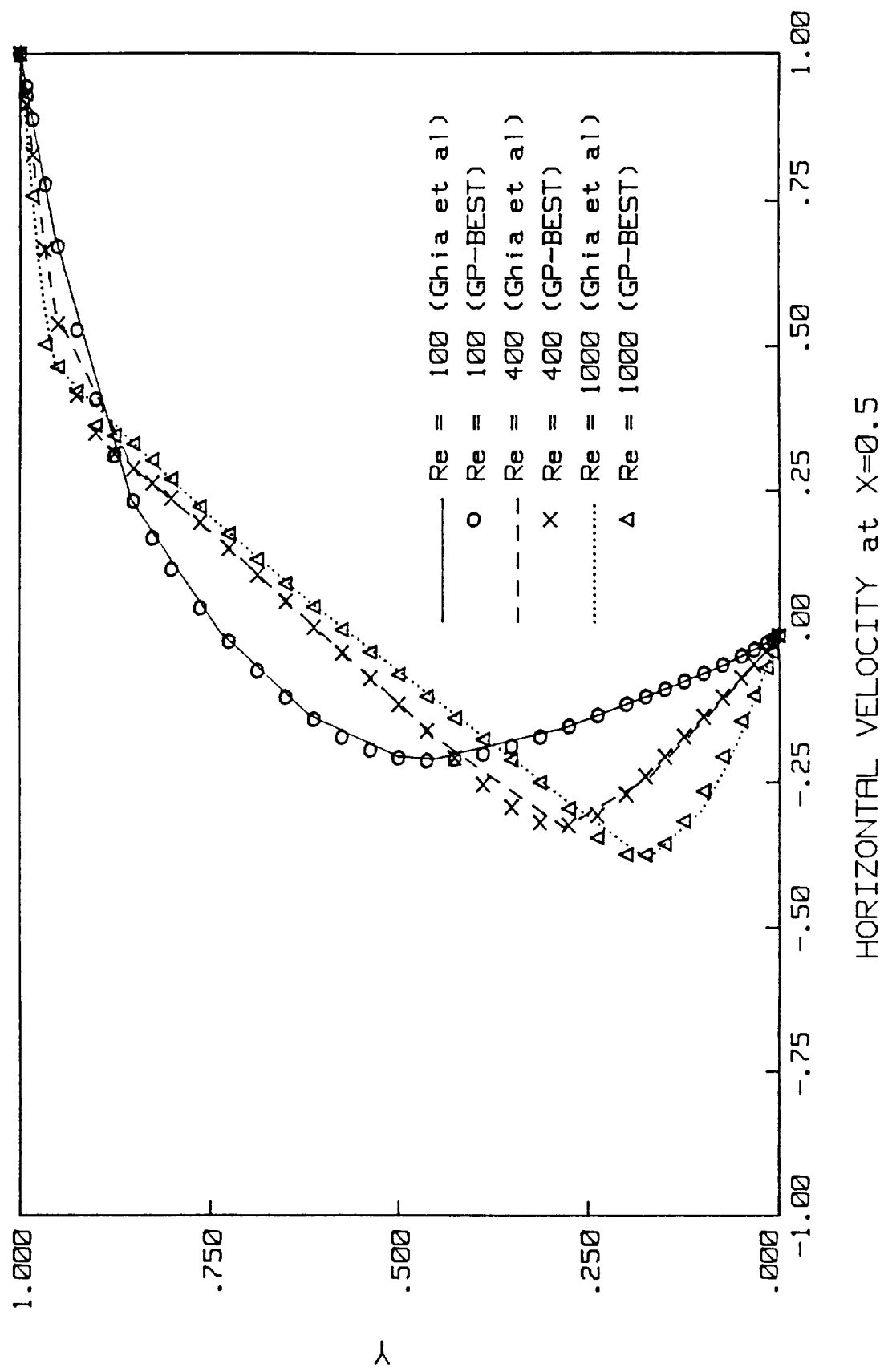


FIGURE 4.16

DRIVEN CAVITY - SINGLE REGION MODEL
VELOCITY PROFILE @ $Re = 100$

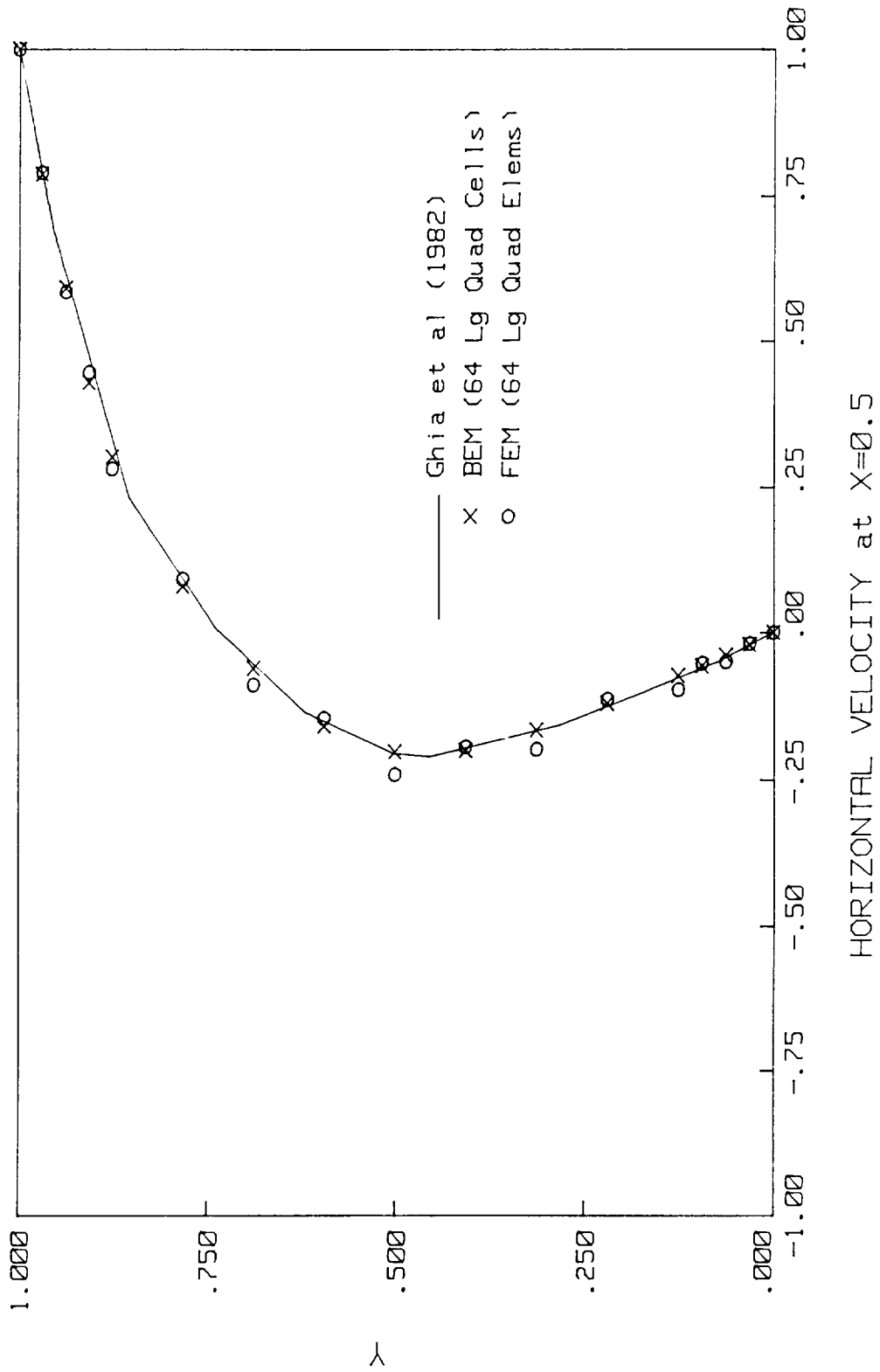
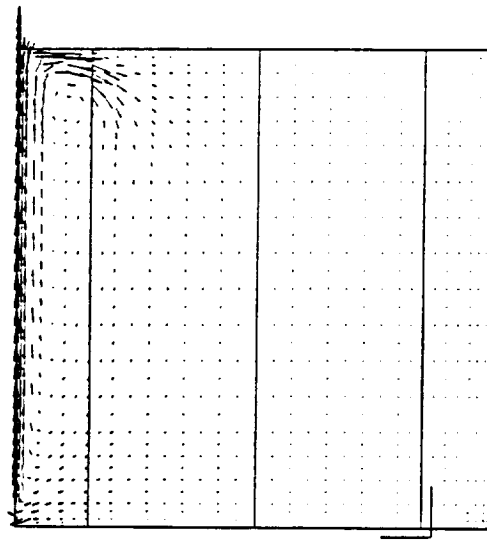
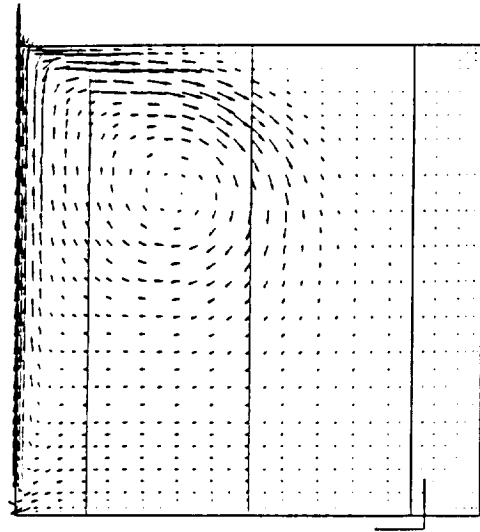


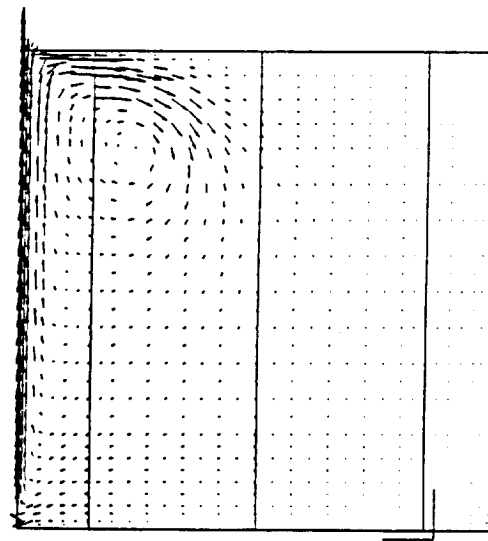
FIGURE 4.17 - TRANSIENT DRIVEN CAVITY FLOW



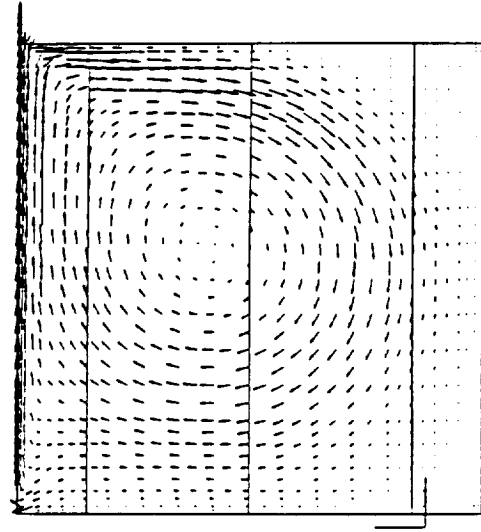
a) $Re = 1000, t = 1.0$



c) $Re = 1000, t = 5.0$



b) $Re = 1000, t = 2.5$



d) $Re = 1000, t = 12.5$

FIGURE 4.18

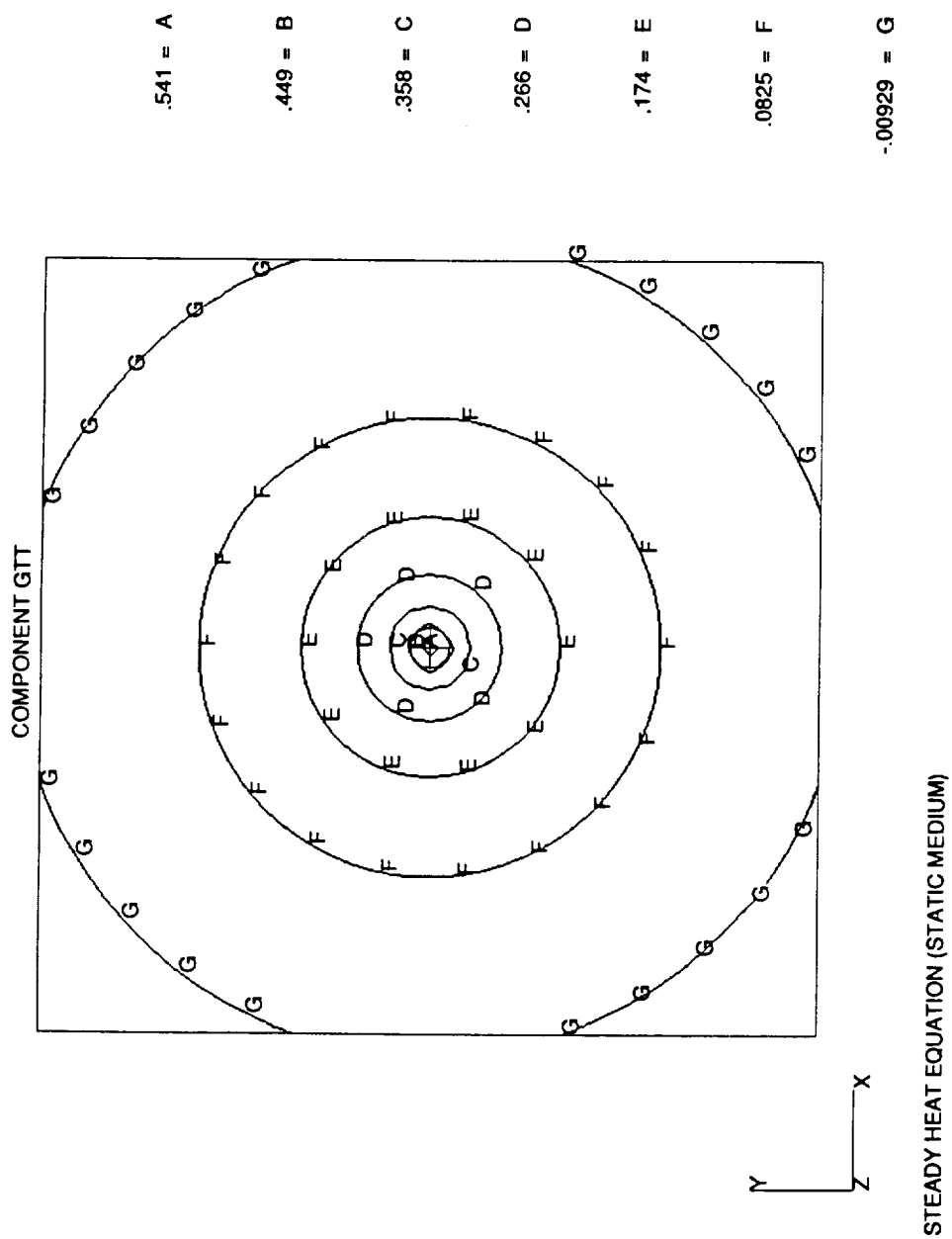
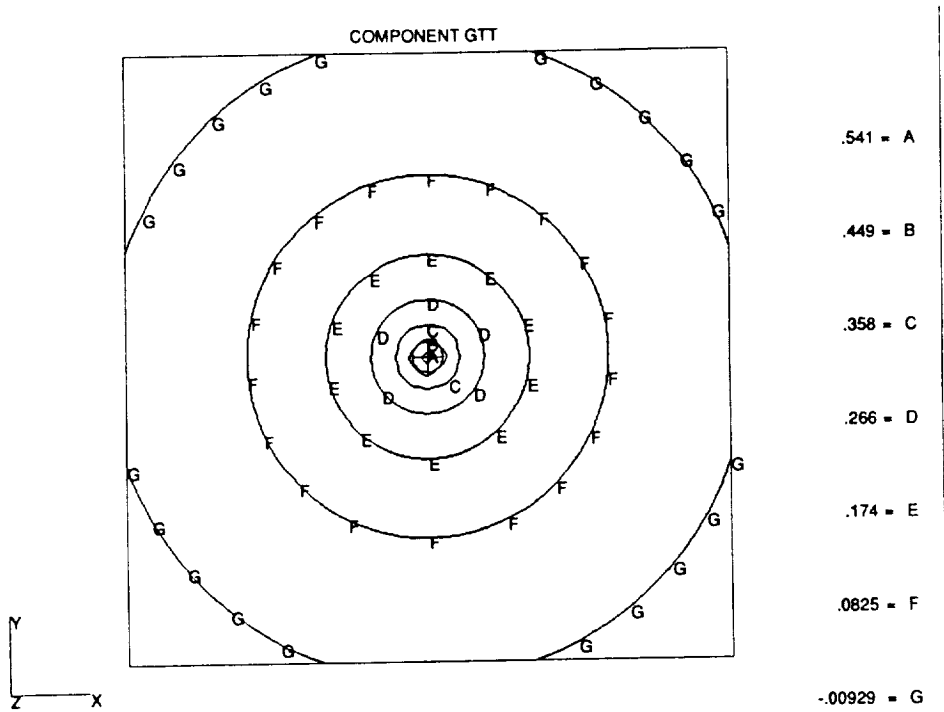
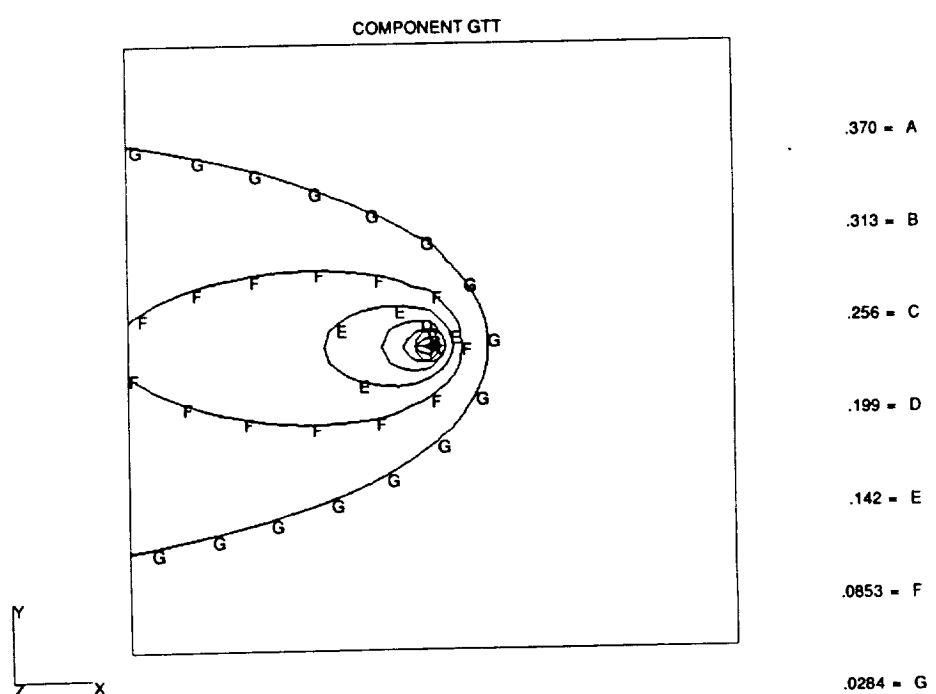


FIGURE 4.19a



INCOMPRESSIBLE CONVECTIVE THERMOVISCOS FLOW (RE = 0.0)

FIGURE 4.19b



INCOMPRESSIBLE CONVECTIVE THERMOVISCOS FLOW (RE = 10.0)

FIGURE 4.19c

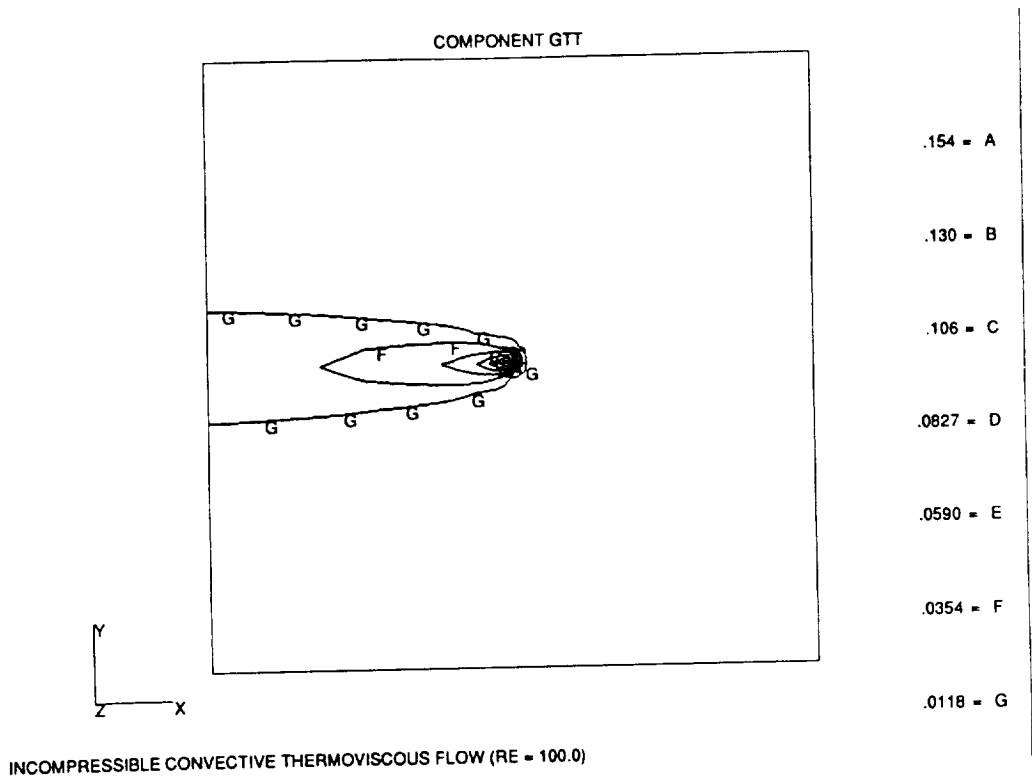


FIGURE 4.19d

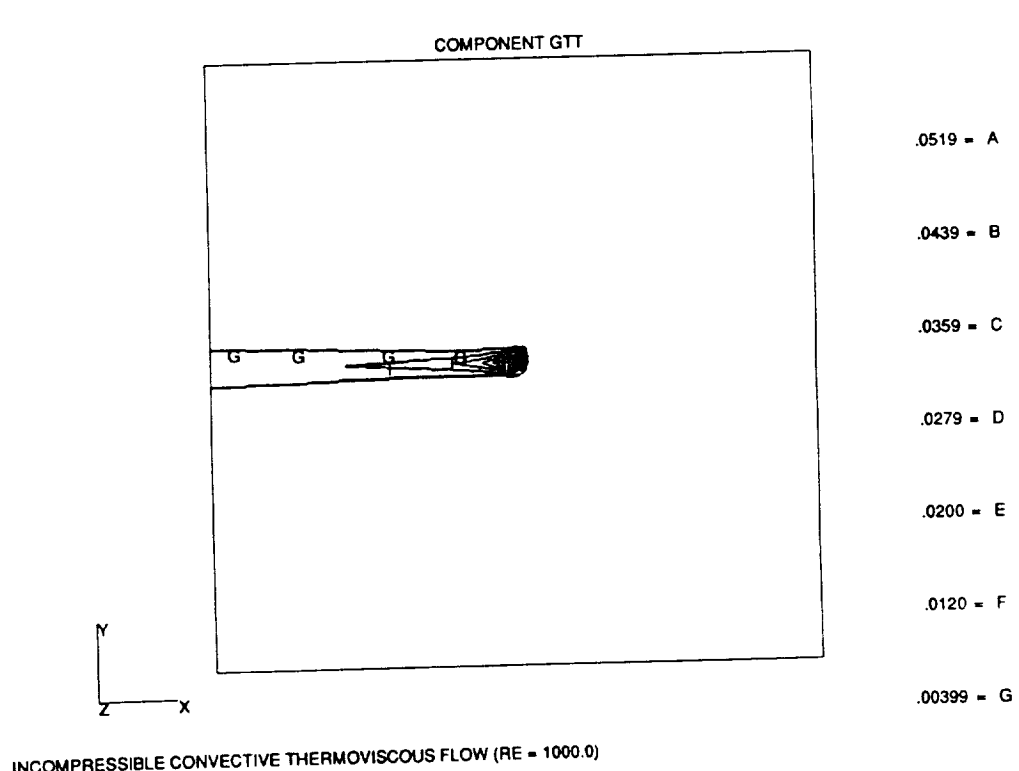


FIGURE 4.20a

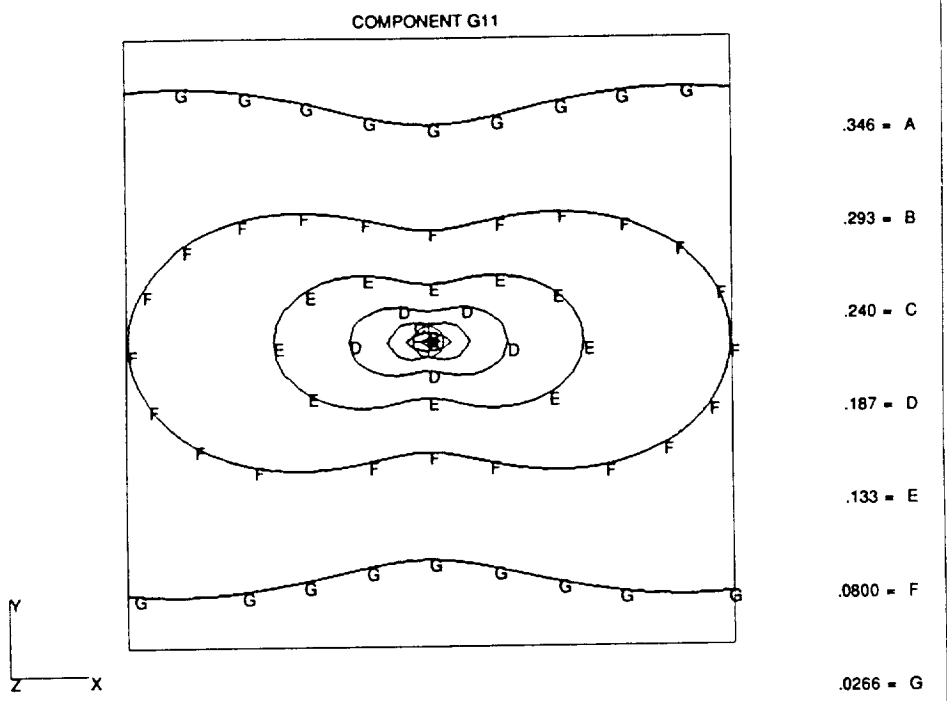


FIGURE 4.20b

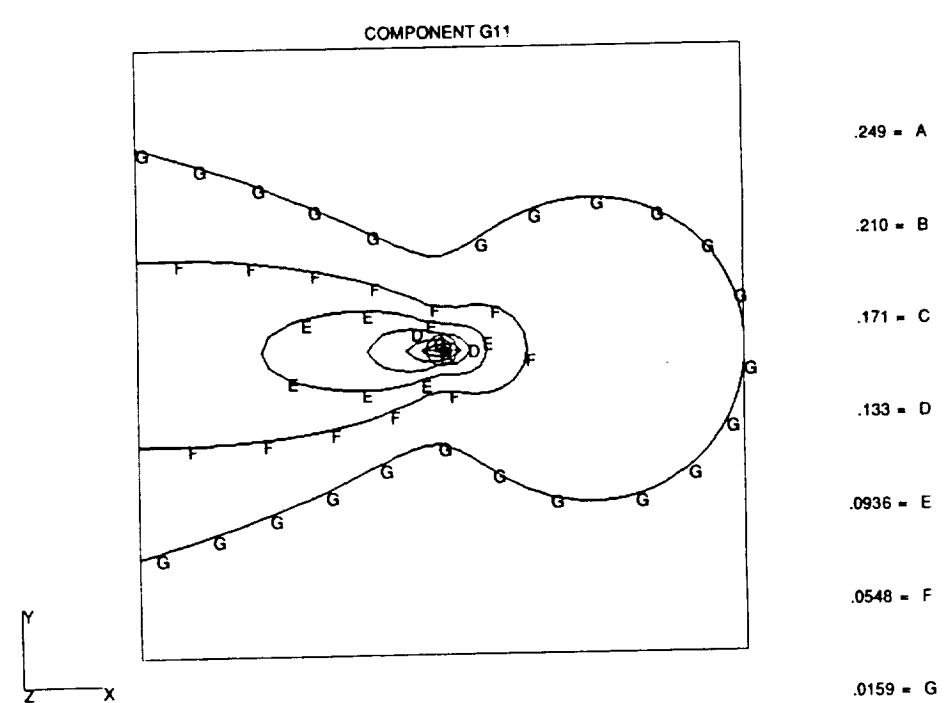


FIGURE 4.20c

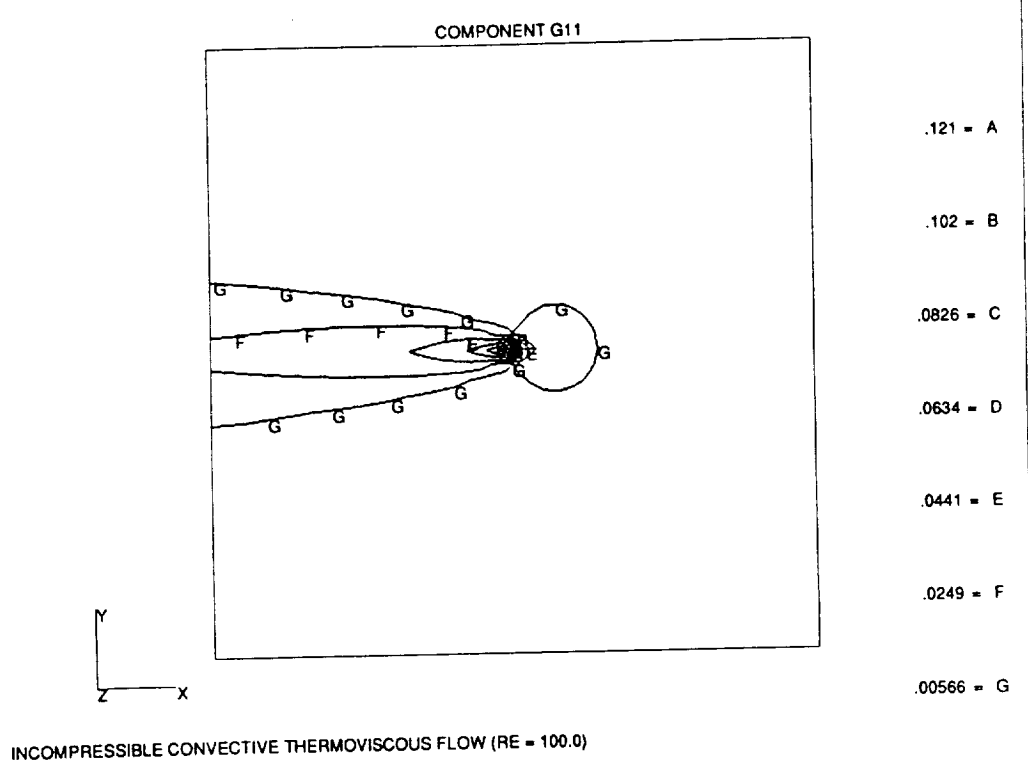


FIGURE 4.20d

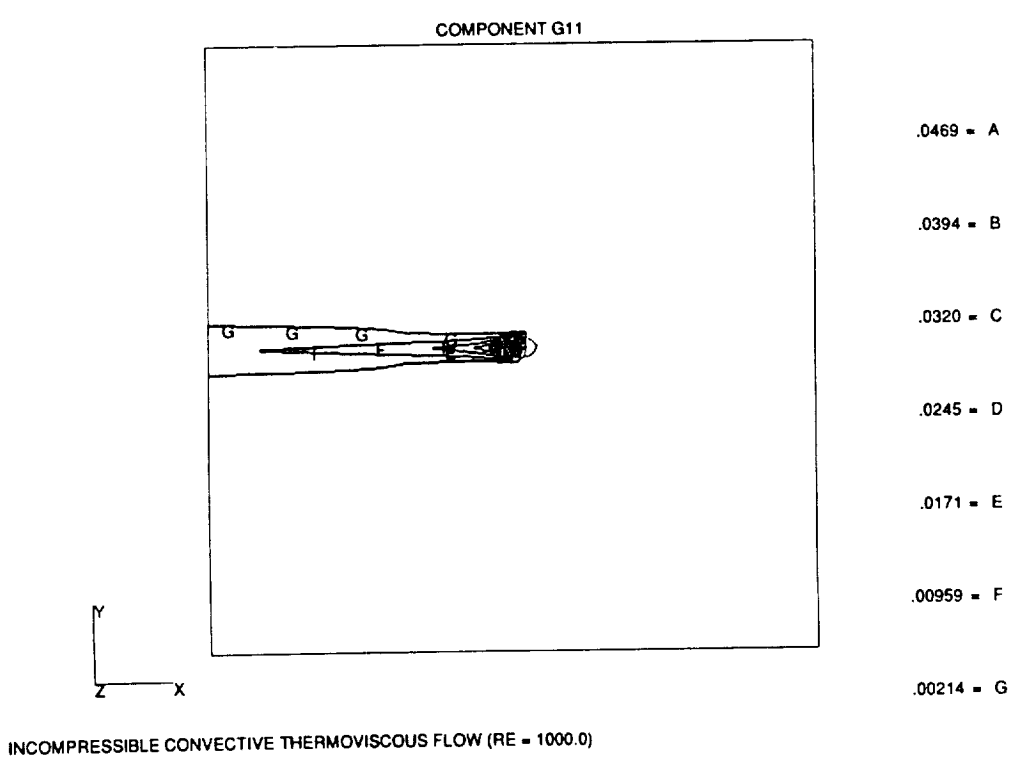


FIGURE 4.21

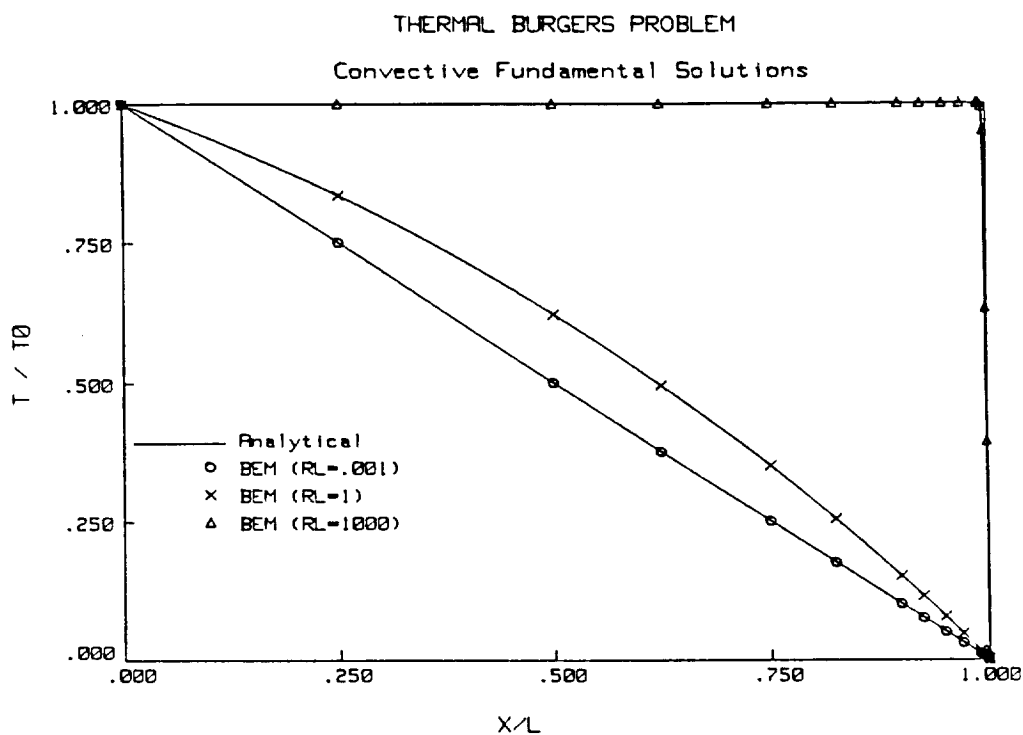


FIGURE 4.22

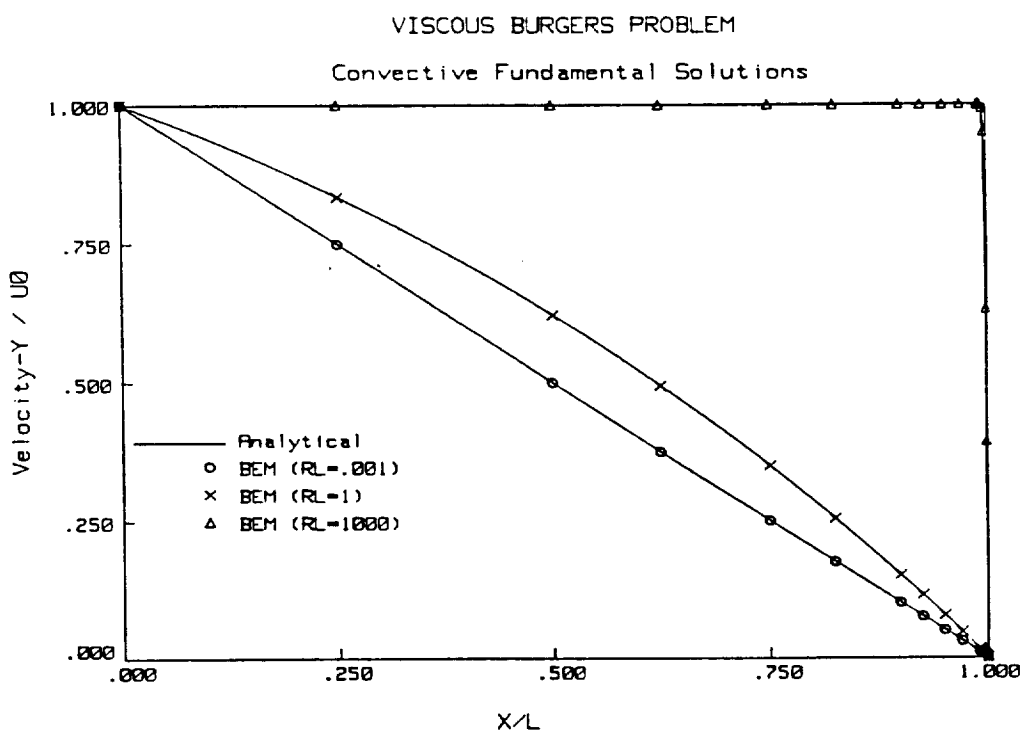


FIGURE 4.23
VISCOUS BURGERS PROBLEM

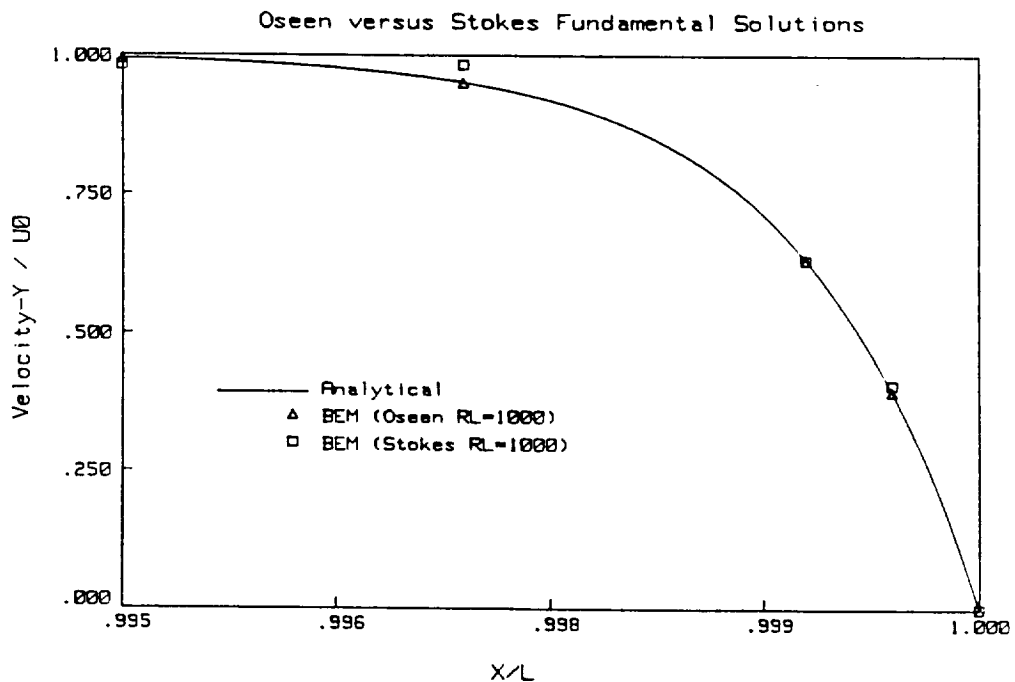


FIGURE 4.24
FLOW AROUND A CYLINDER
Boundary Element Model

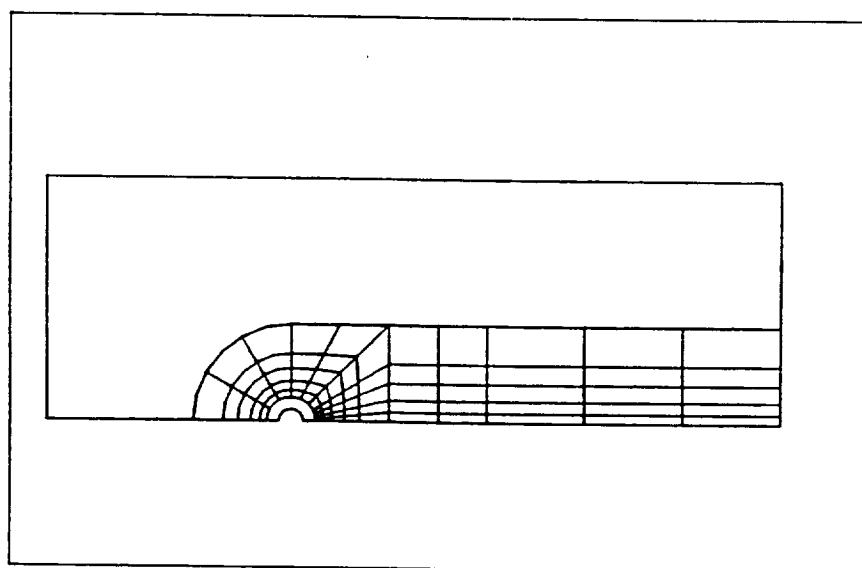


FIGURE 4.25
FLOW OVER A CYLINDER
VELOCITY VECTORS AT $Re = 40$

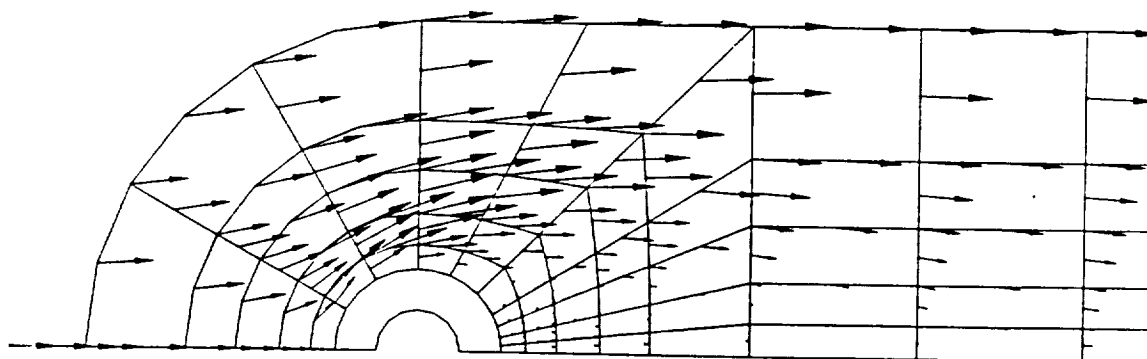
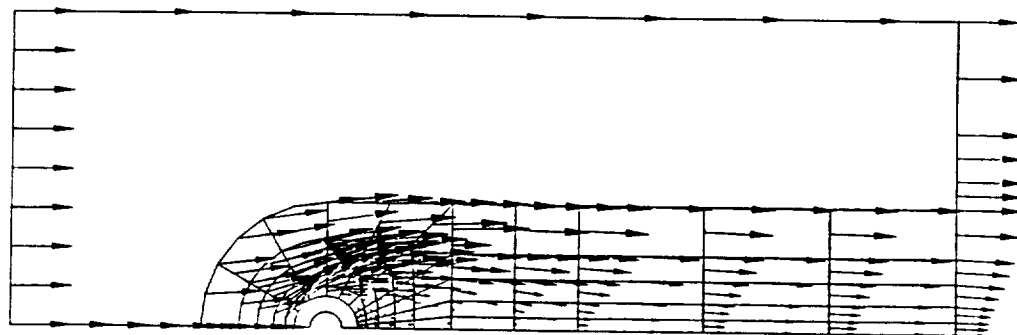


FIGURE 4.26 FLOW OVER A CYLINDER - FULL MESH

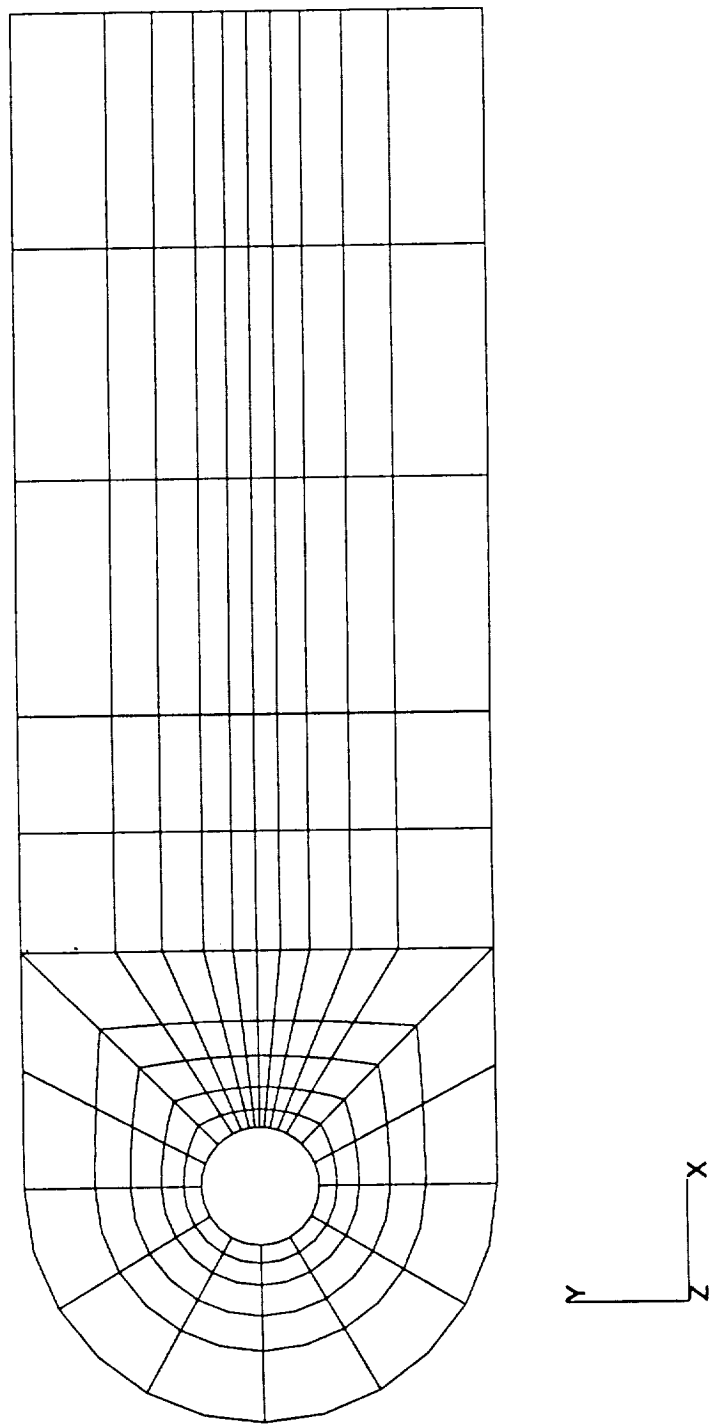


FIGURE 4.27a FULL CYLINDER (ANGLE OF ATTACK = 0°)

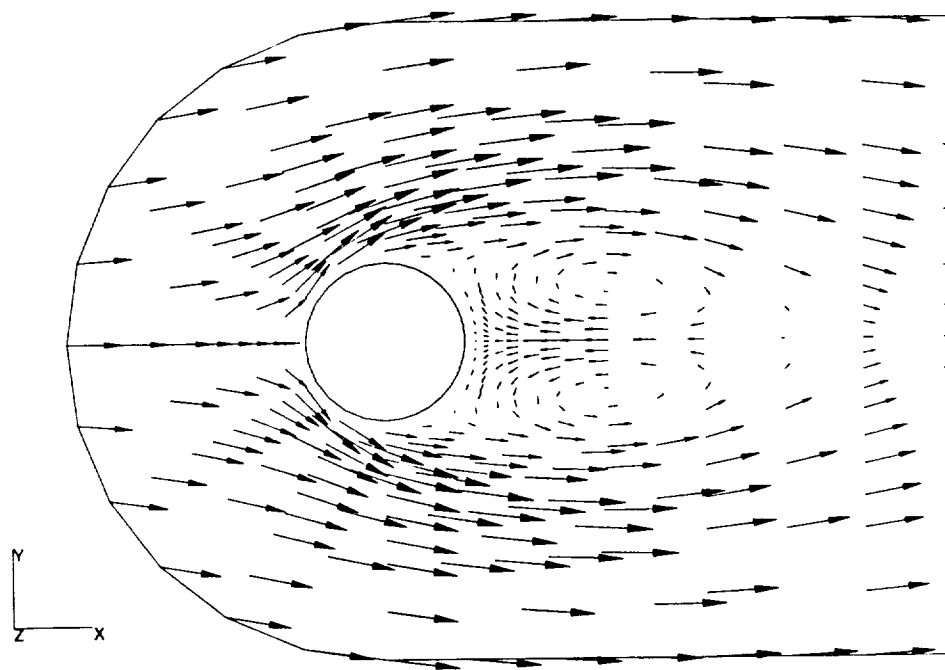


FIGURE 4.27b FULL CYLINDER (ANGLE OF ATTACK = 10°)

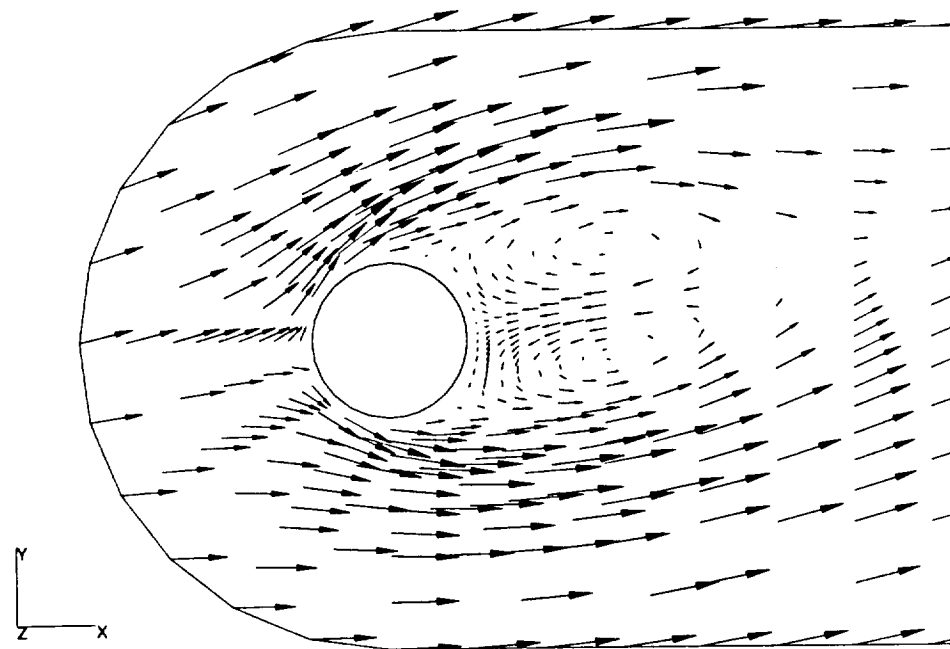


FIGURE 4.28

FLOW OVER A CYLINDER
NONLINEAR SOLUTION VERSUS LINEAR OSEEN SOLUTION

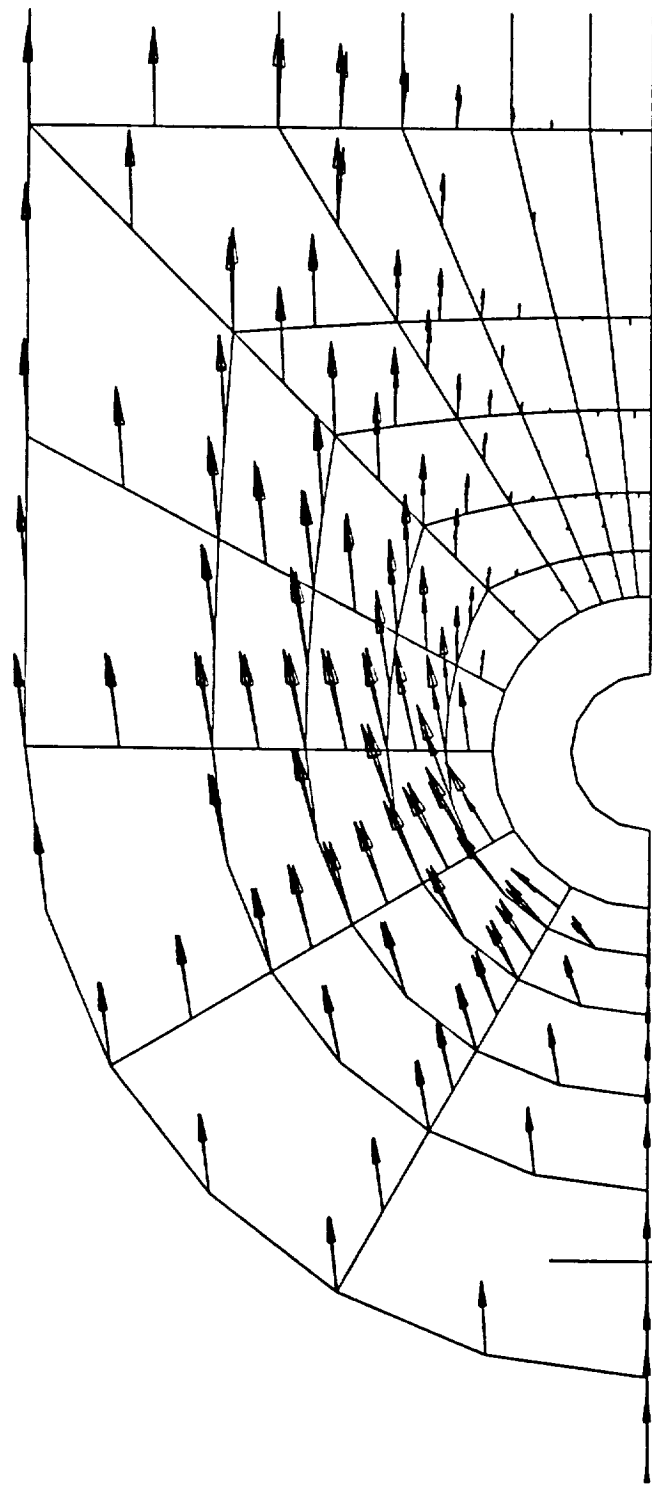


FIGURE 4.29

FLOW OVER A CYLINDER

Drag versus Reynolds Number

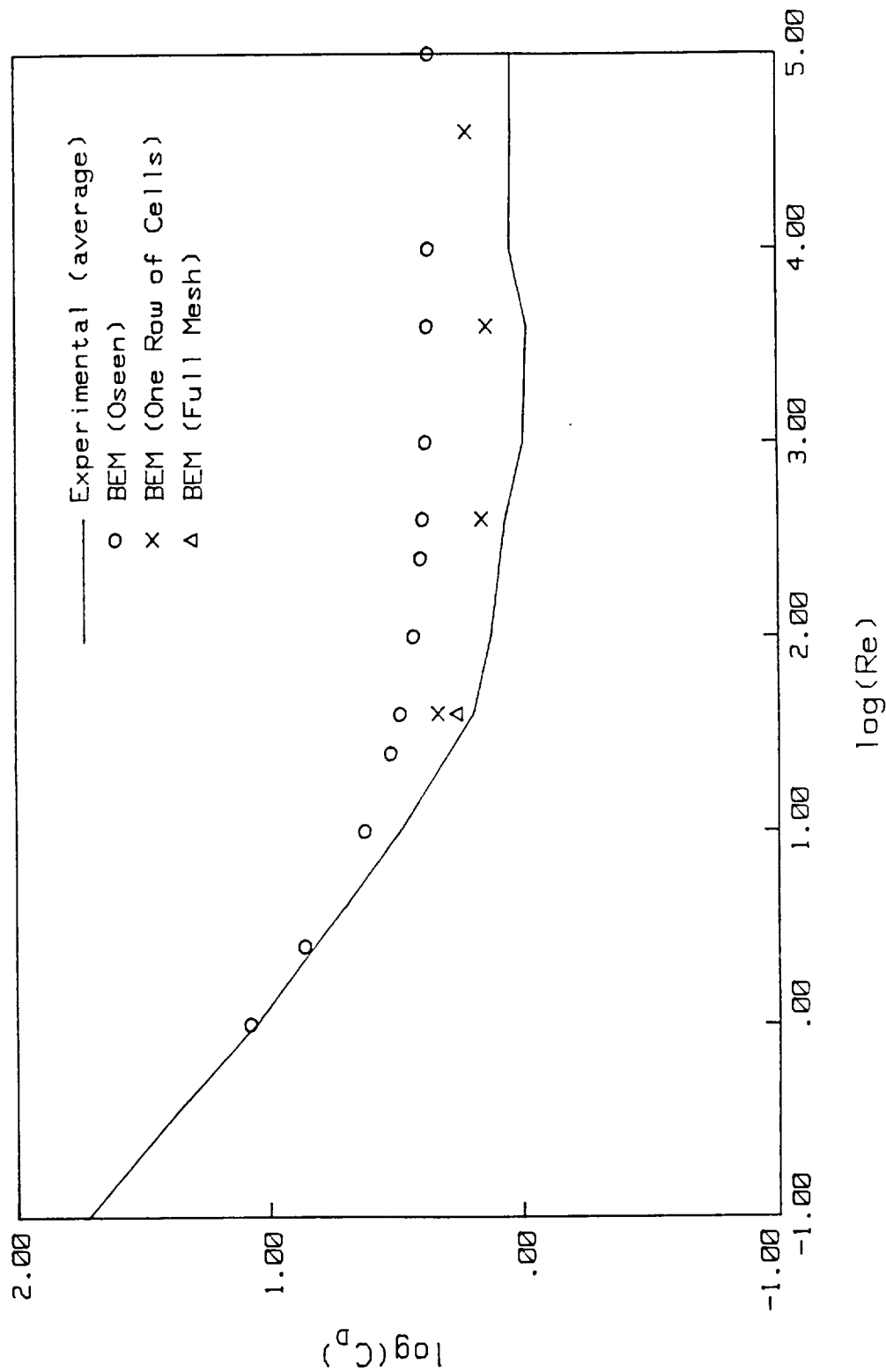


FIGURE 4.30

FLOW OVER A CYLINDER

NONLINEAR SOLUTION WITH A SINGLE ROW OF CELLS

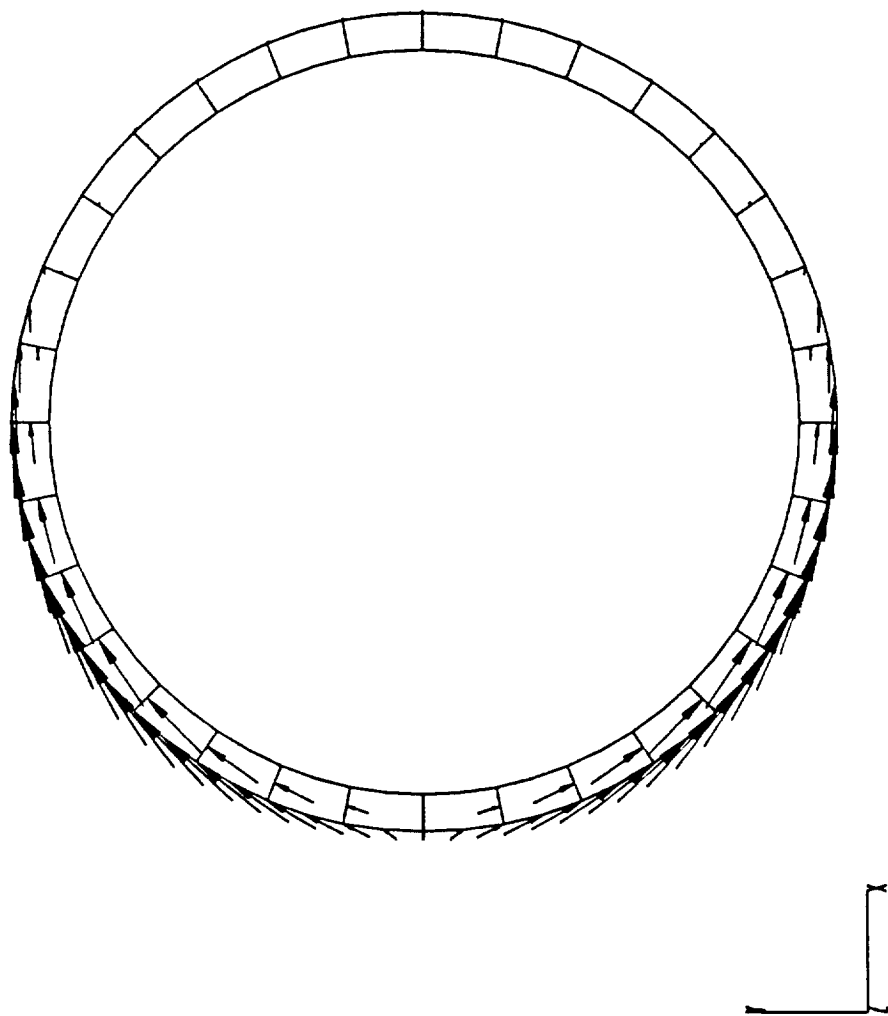


FIGURE 4.31

NACA-0018 AIRFOILS - BOUNDARY ELEMENT MODEL

W/SHRINK ELEMENTS OPTION

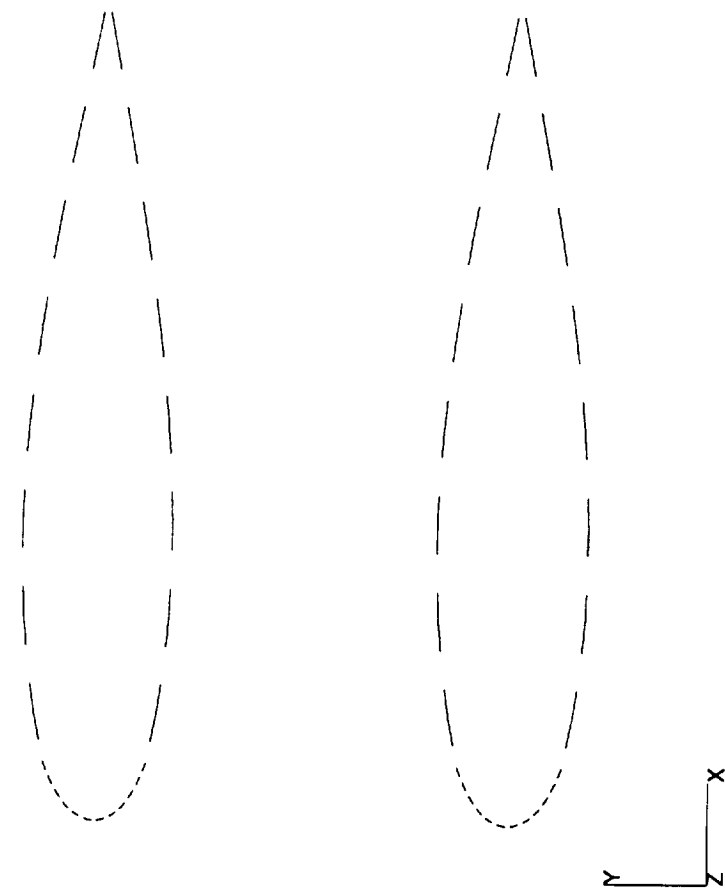


FIGURE 4.32a

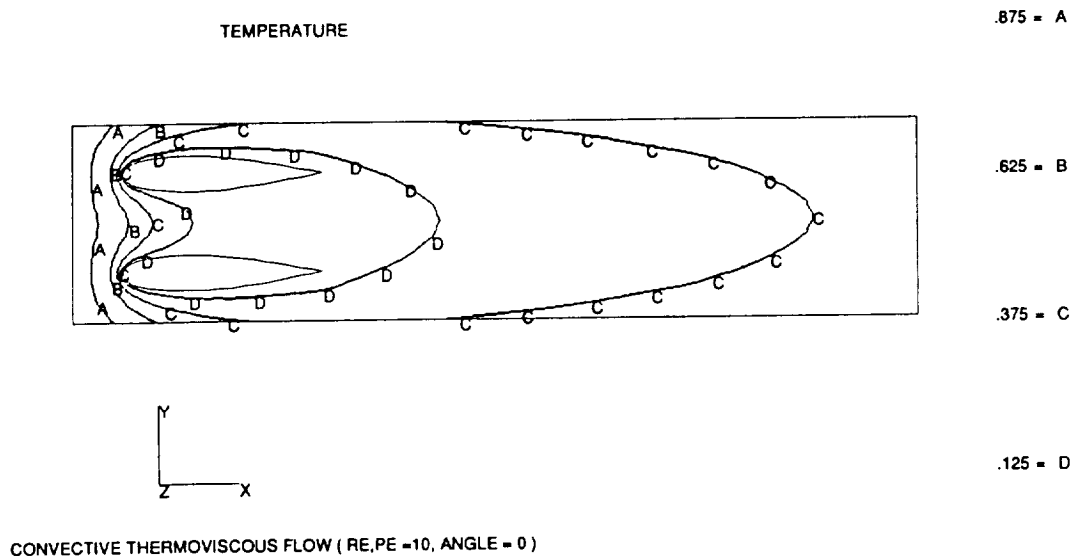


FIGURE 4.32b

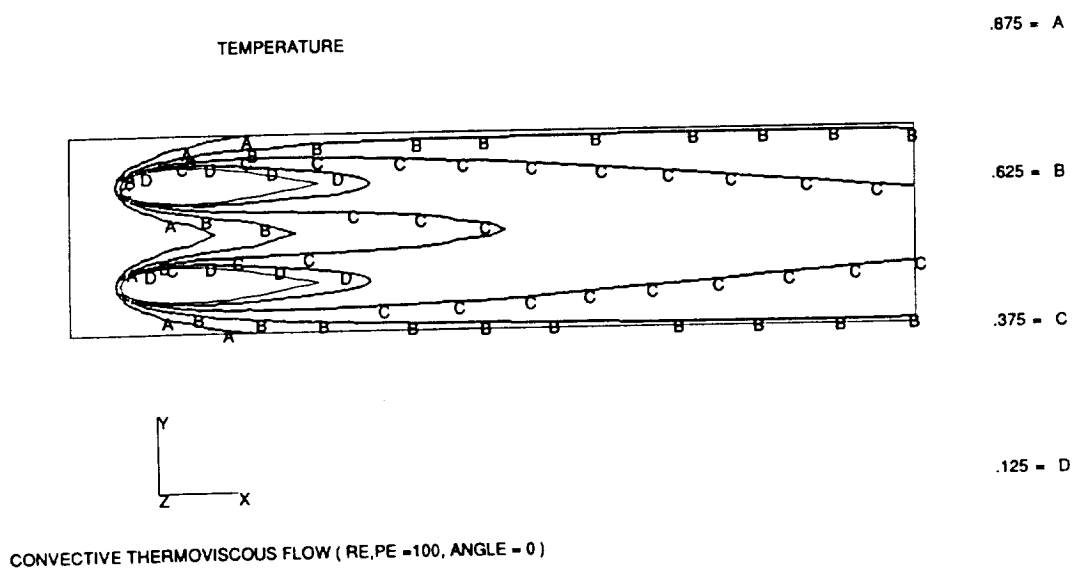


FIGURE 4.32C

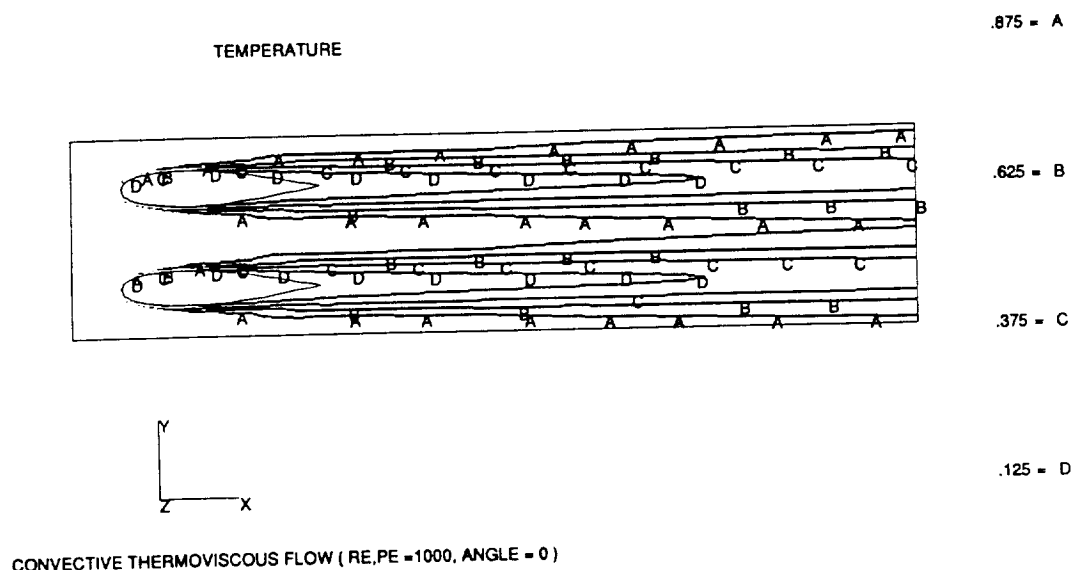


figure 4.32d

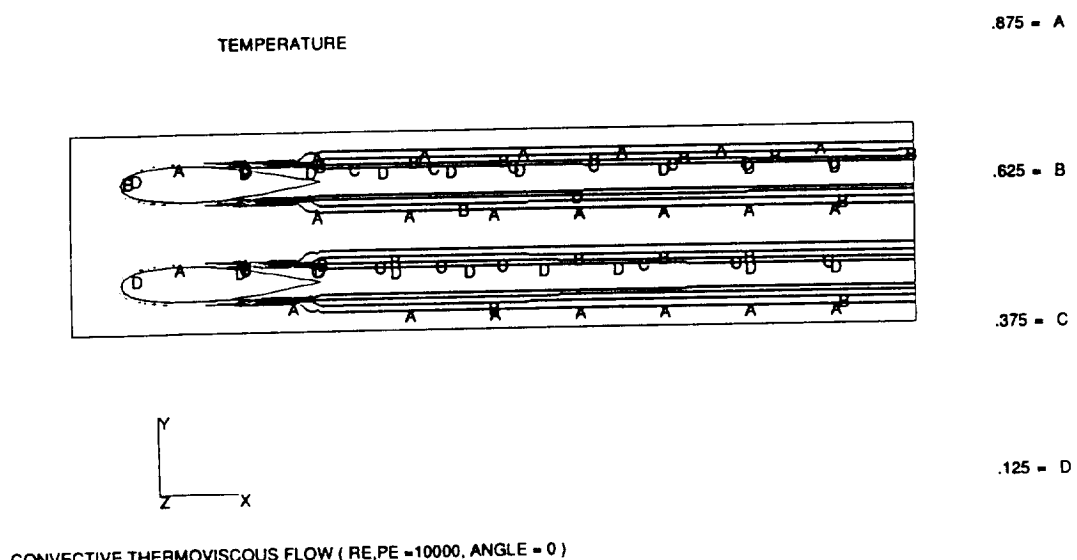


FIGURE 4.32e

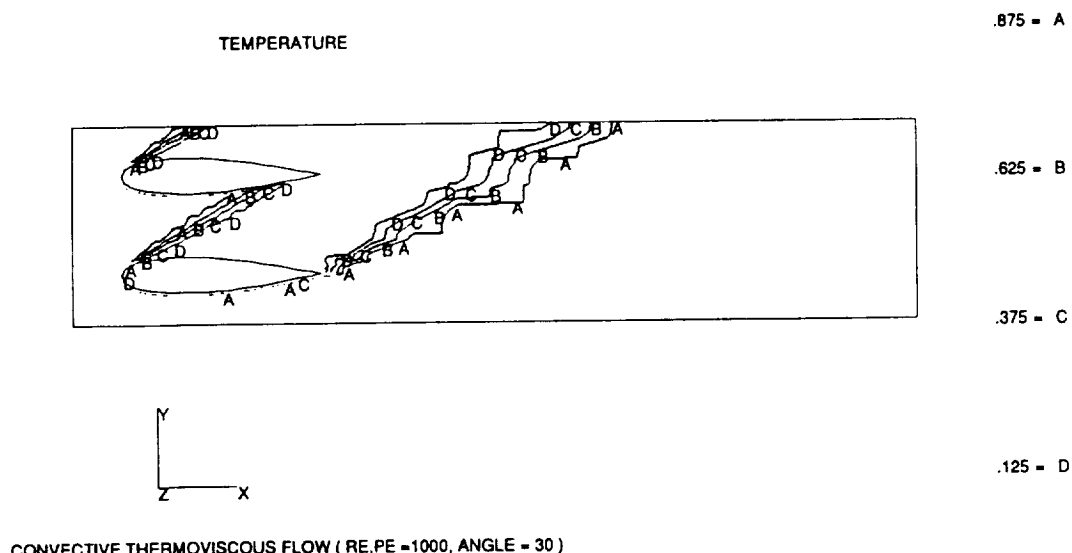


FIGURE 4.33a

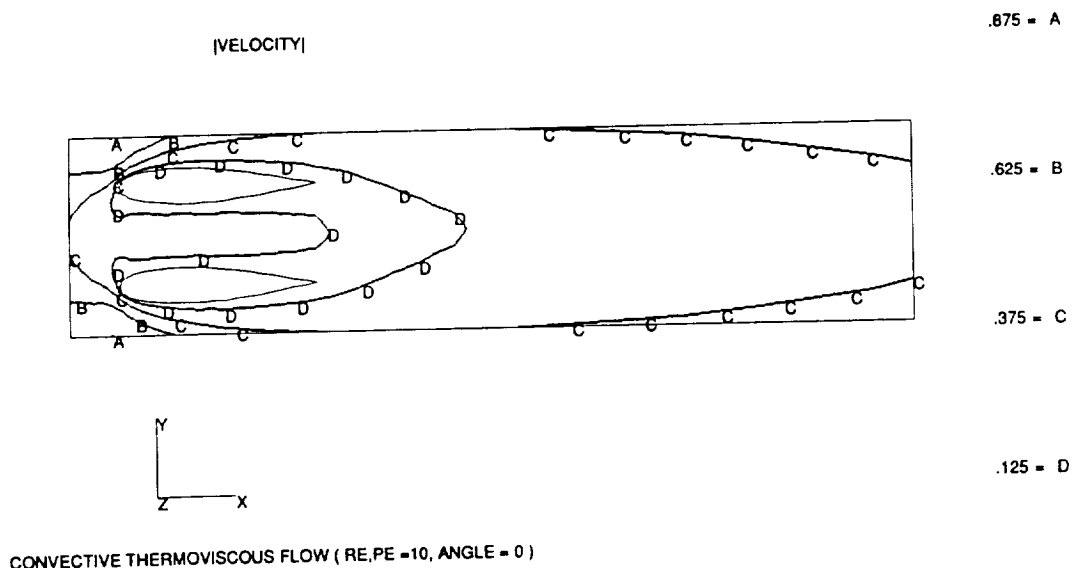


FIGURE 4.33b

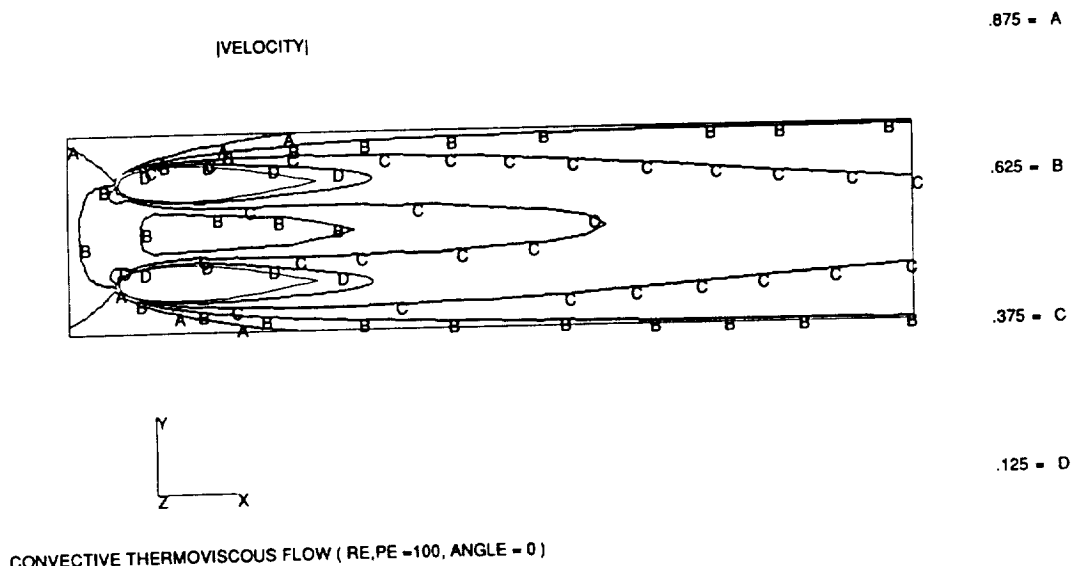


FIGURE 4.33c

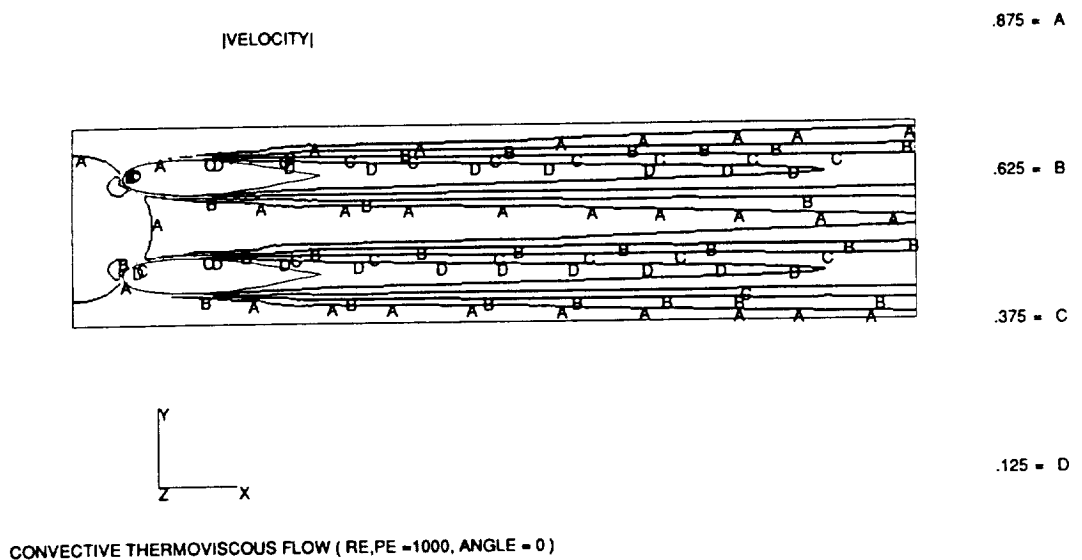


FIGURE 4.33d

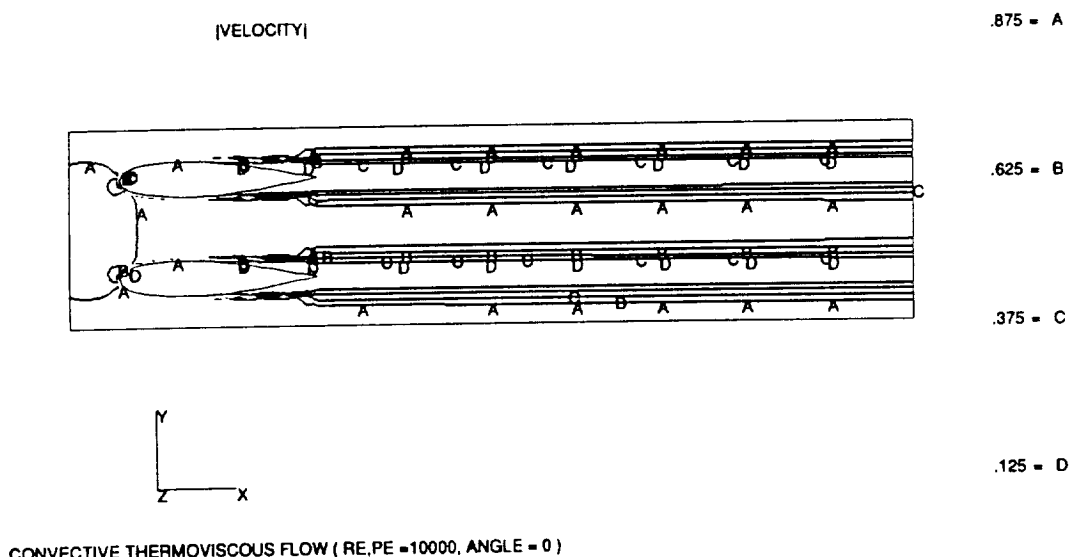


FIGURE 4.33e

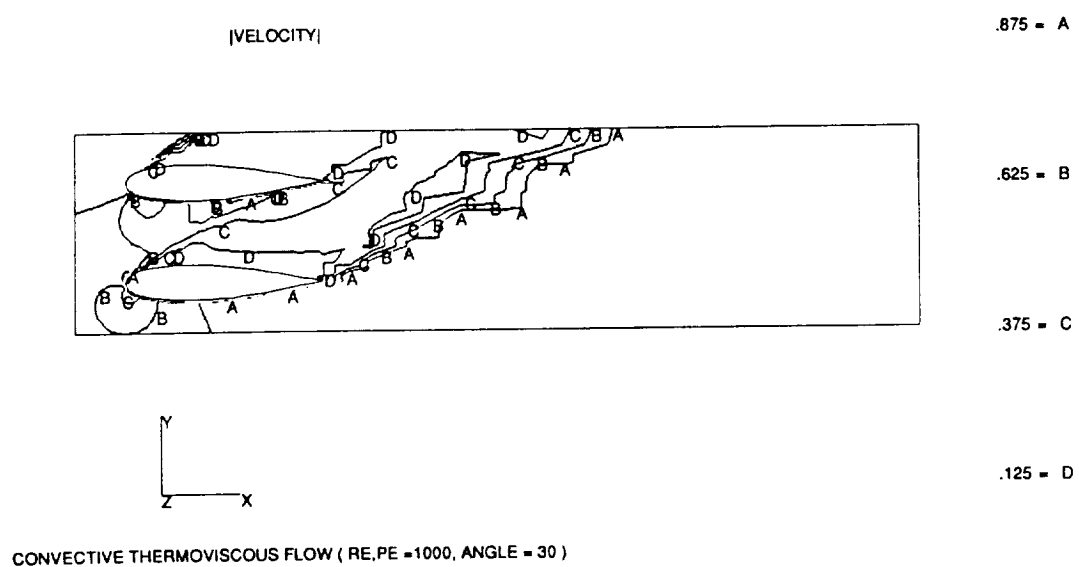
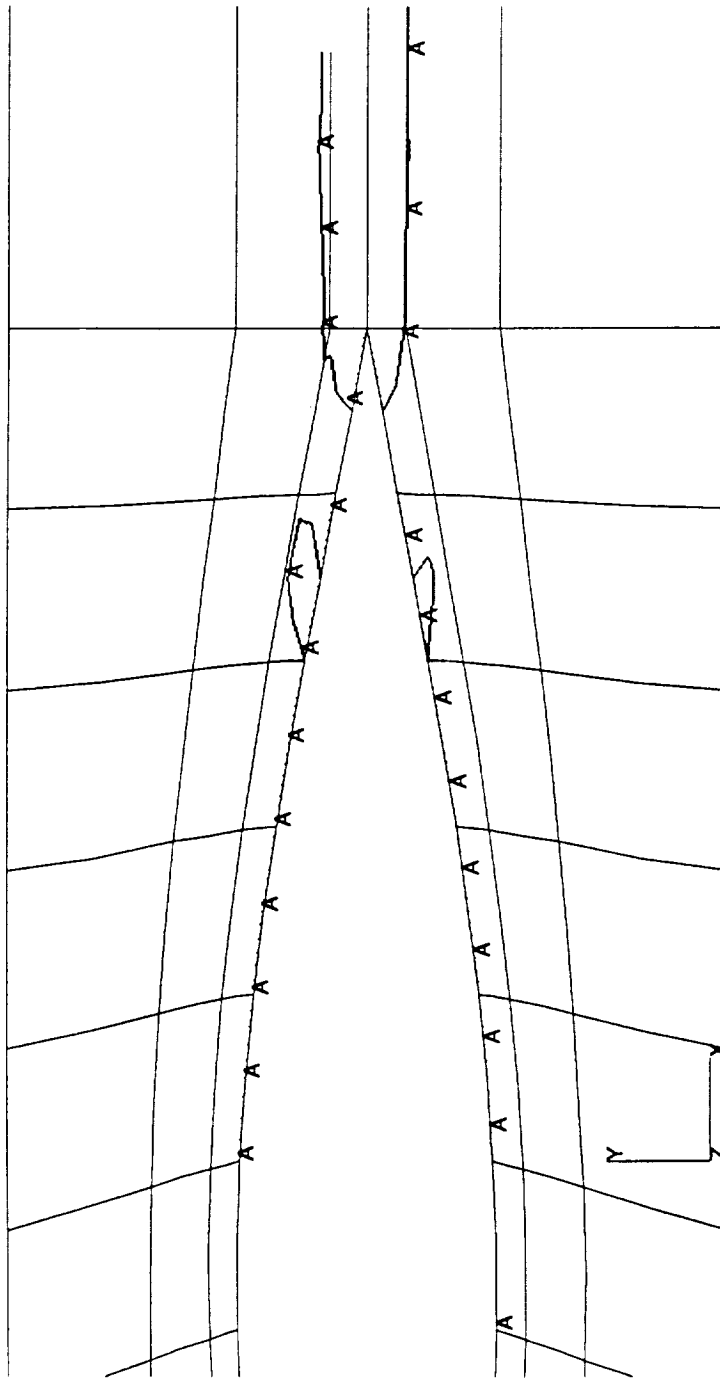


FIGURE 4.34 BOUNDARY LAYER SEPARATION



CONVECTIVE THERMOVISCous FLOW ($RE, PE = 1000$, ANGLE = 0)

FIGURE 4.35a

NACA-0018 AIRFOILS (RE = 10000; ANGLE = 0)

VELOCITY PROFILES

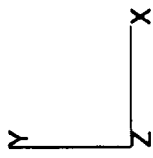
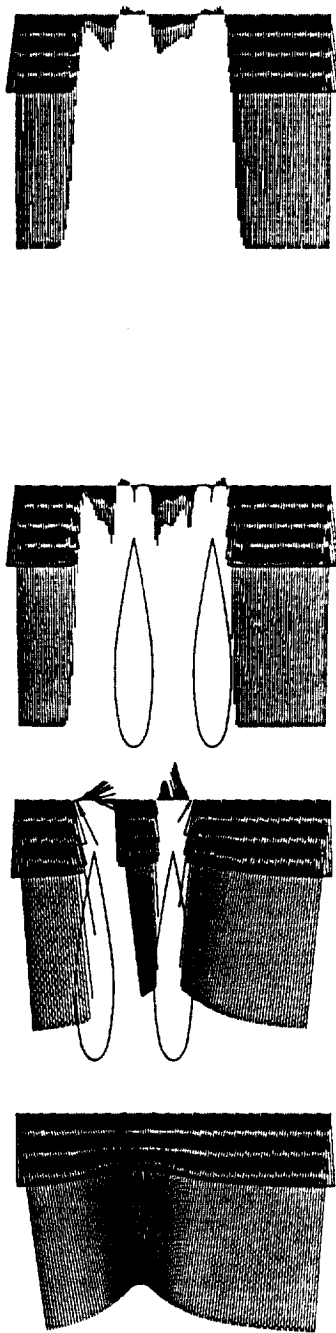


FIGURE 4.35b
NACA-0018 AIRFOILS (RE = 10000; ANGLE = 0)

VELOCITY PROFILES

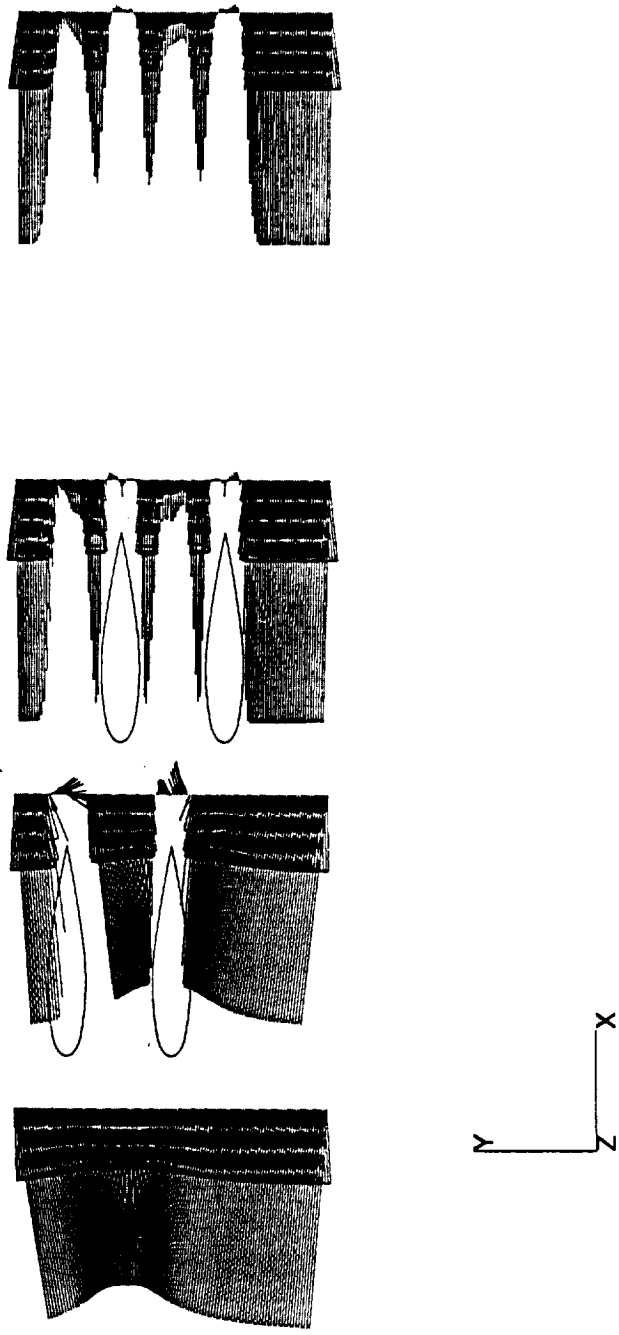


FIGURE 4.35c
NACA-0018 AIRFOILS (RE = 10000; ANGLE = 0)

VELOCITY VECTORS

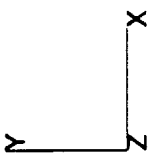
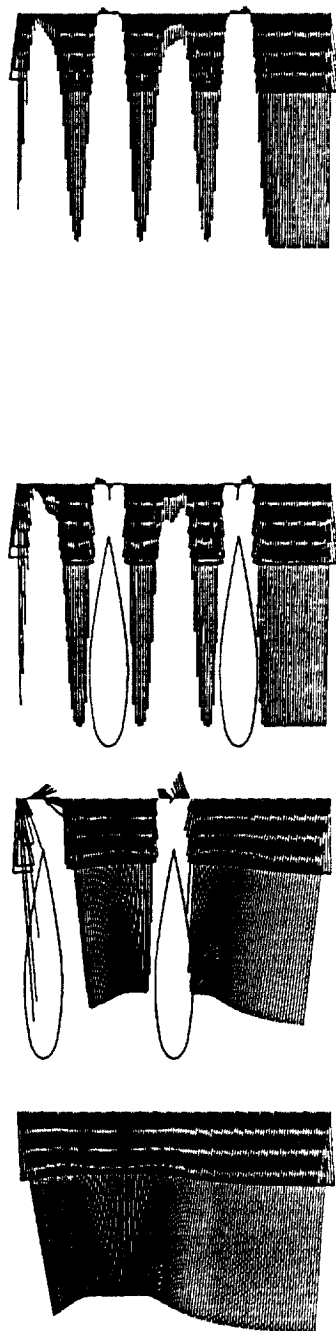


FIGURE 4.36a

NACA-0018 AIRFOILS (RE = 1000000; ANGLE = 0)

VELOCITY PROFILES

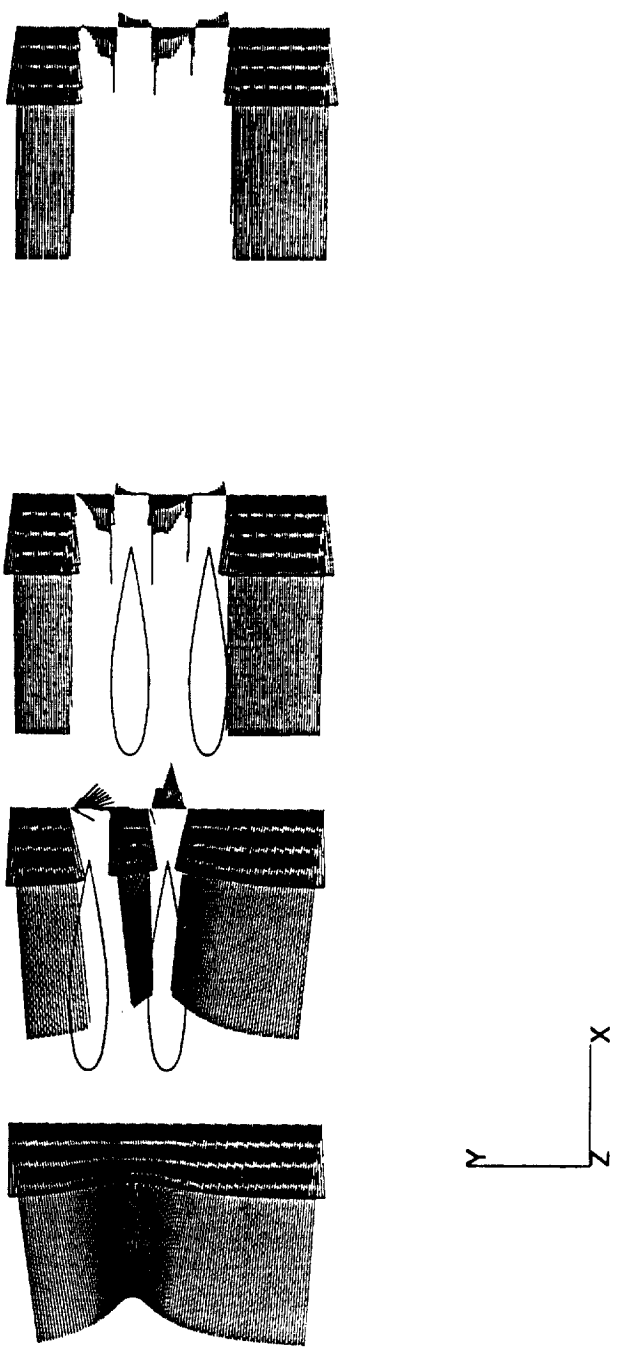


FIGURE 4.36b

NACA-0018 AIRFOILS (RE = 100000, ANGLE = 0)

VELOCITY PROFILES

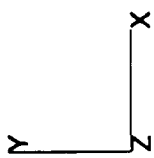
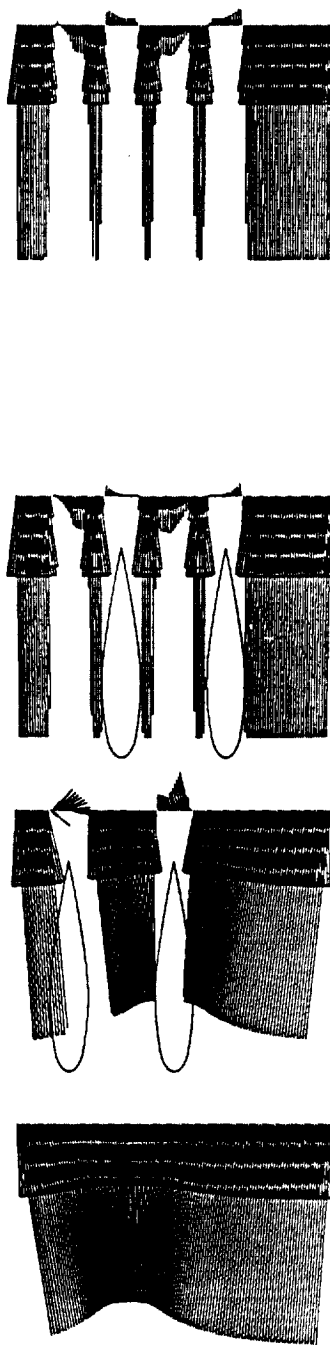


FIGURE 4.36C

NACA-0018 AIRFOILS (RE = 100000; ANGLE = 0)

VELOCITY PROFILES

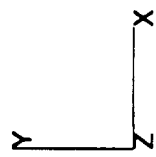
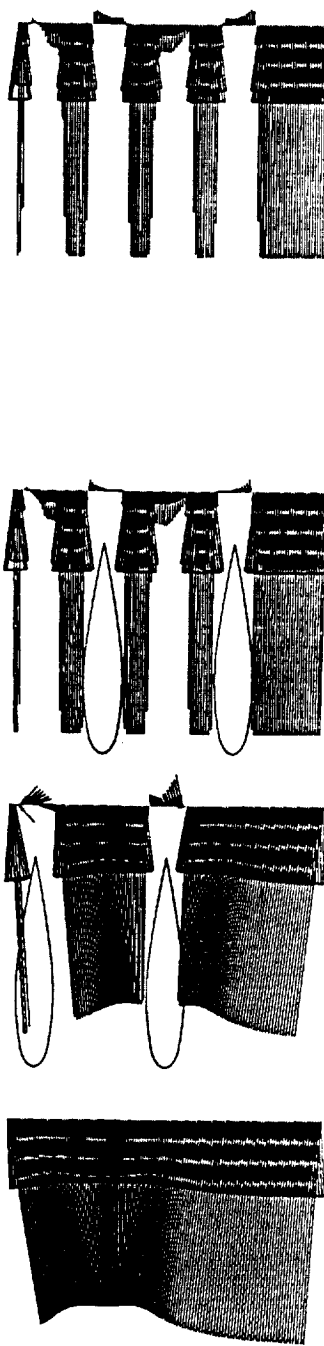


FIGURE 4.37 GRID FOR FUNDAMENTAL SOLUTION CONTOUR PLOTS

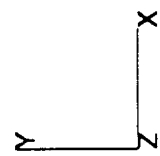
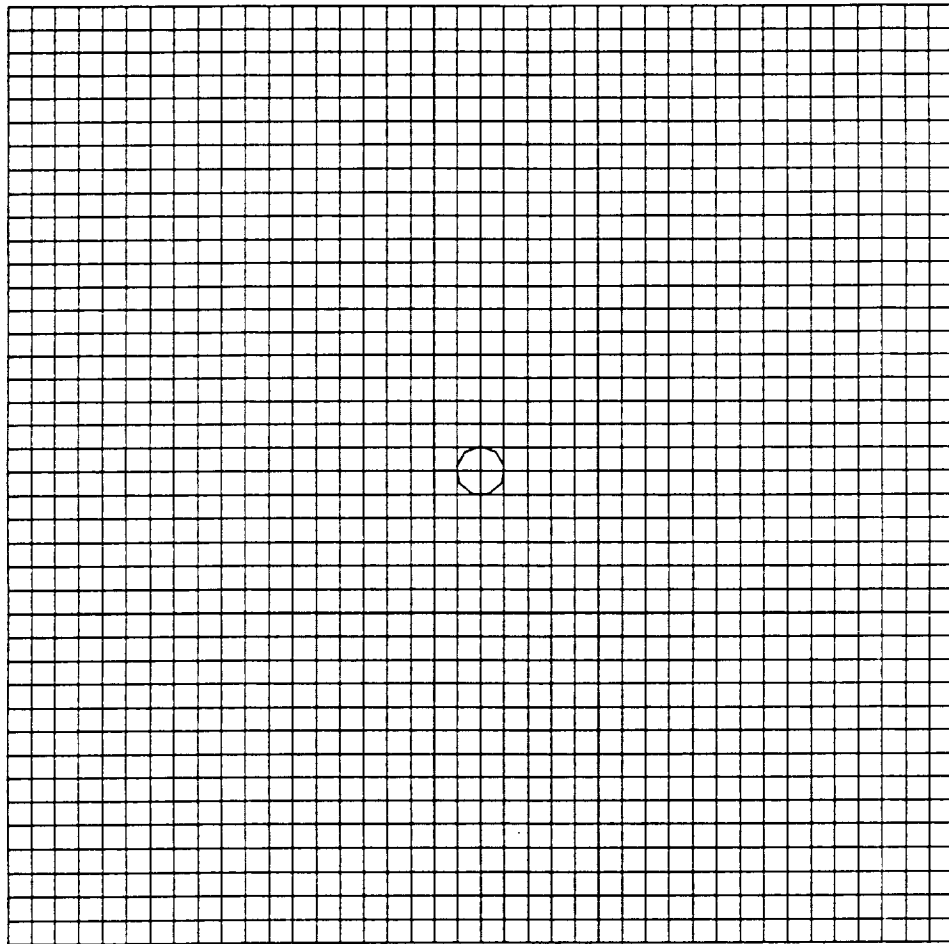


FIGURE 4.38a

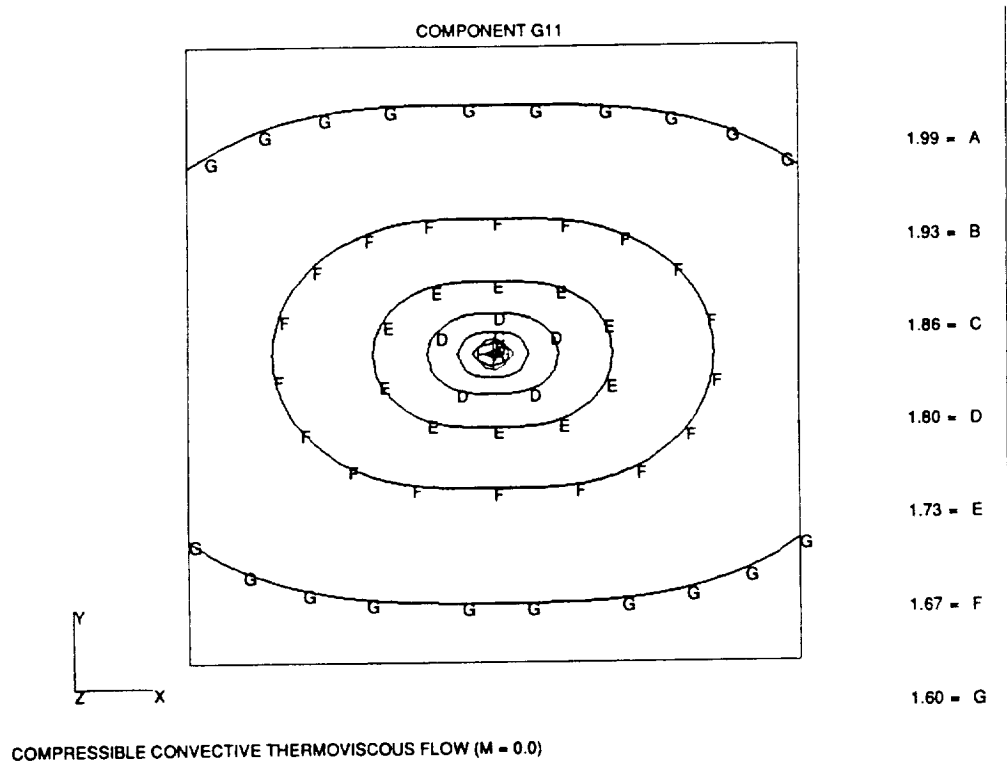


FIGURE 4.38b

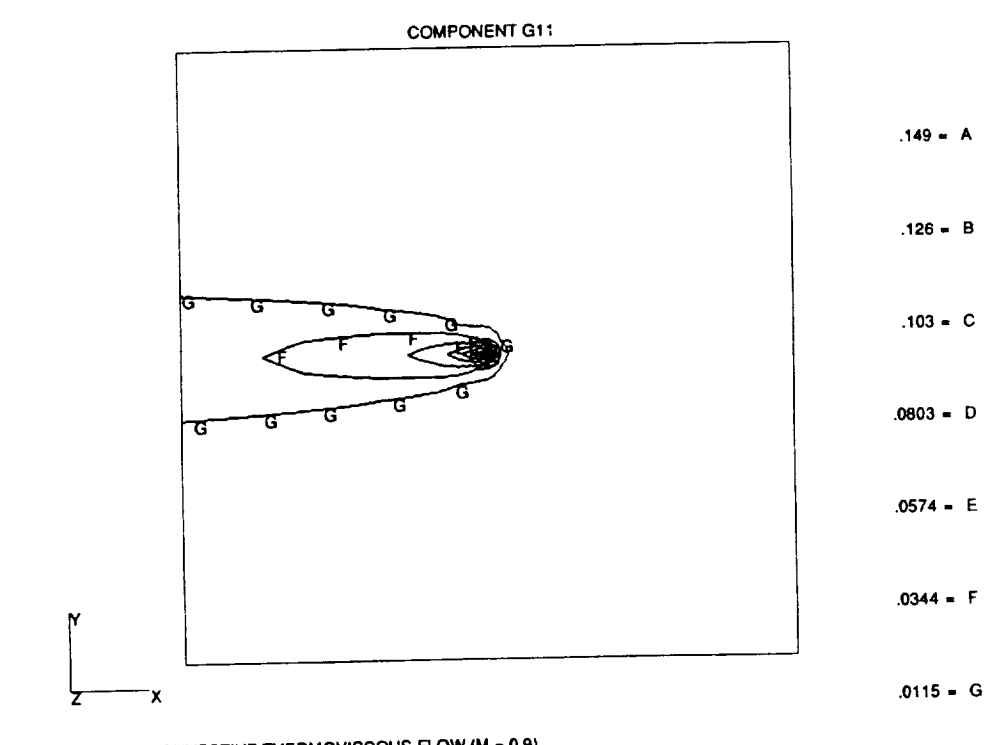


FIGURE 4.38c

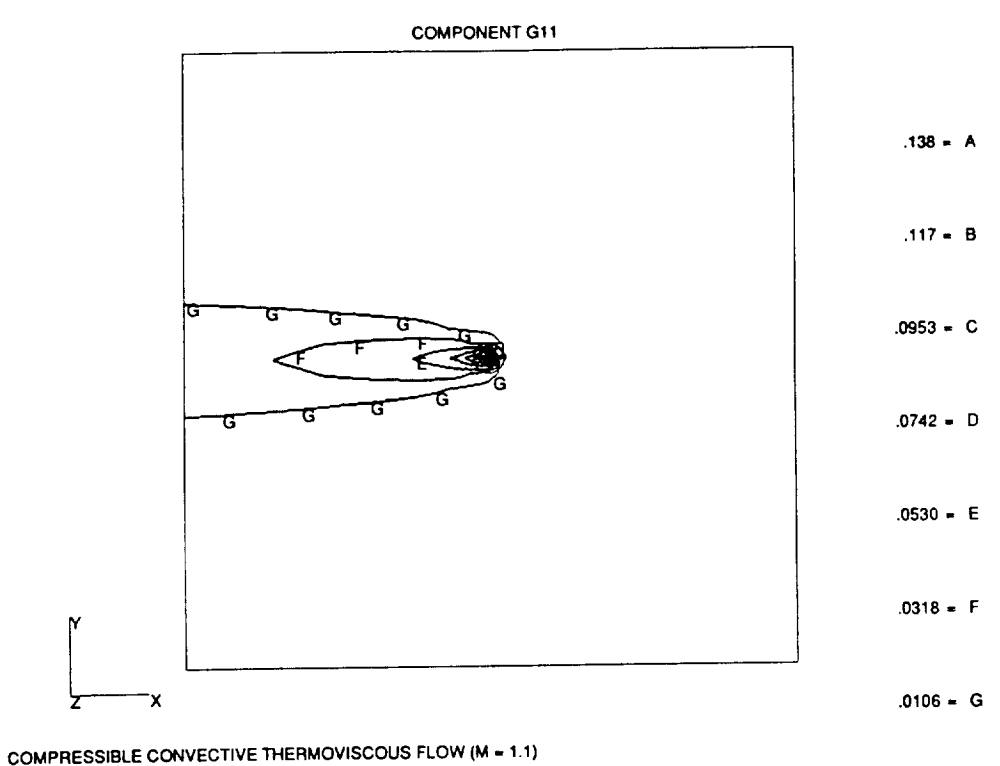


FIGURE 4.38d

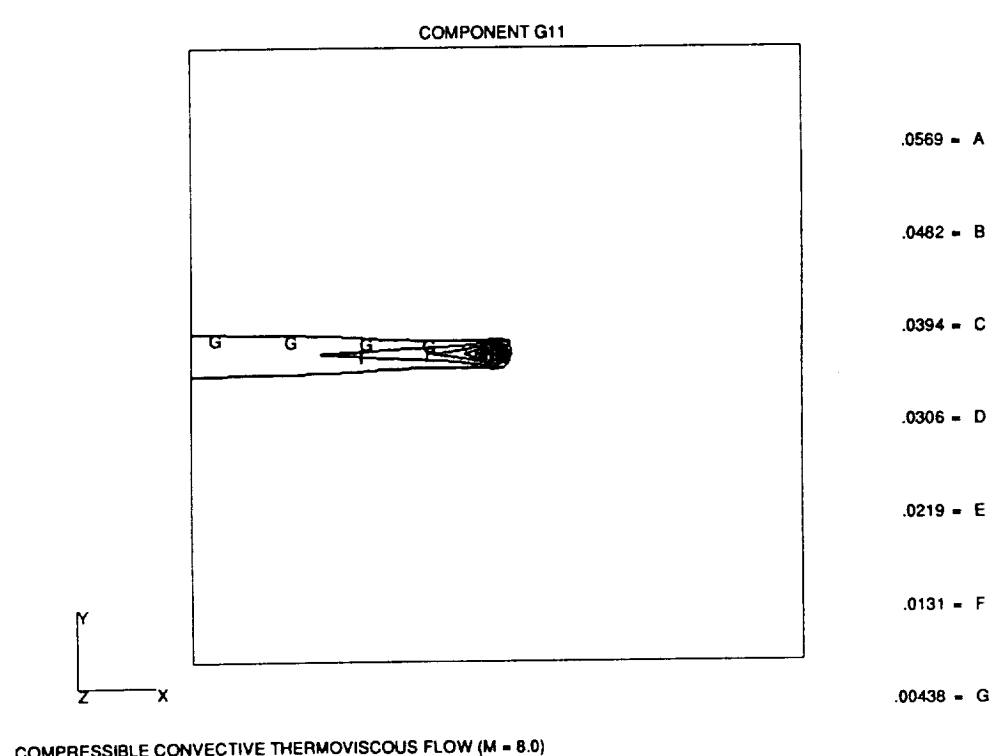


FIGURE 4.39a

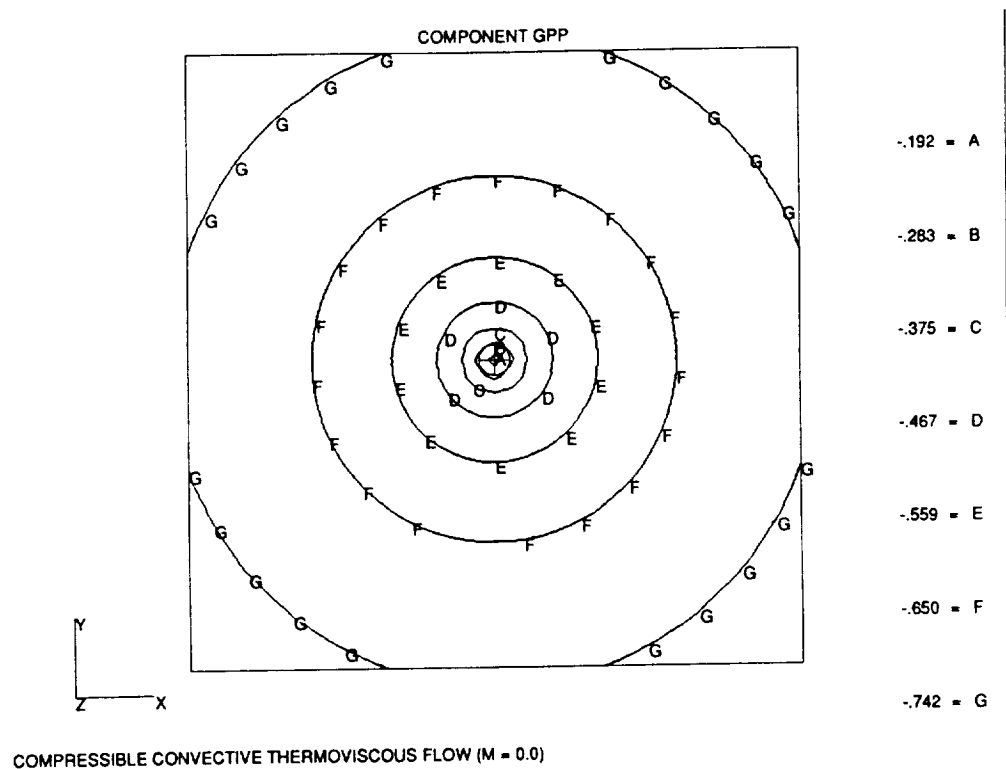


FIGURE 4.39b

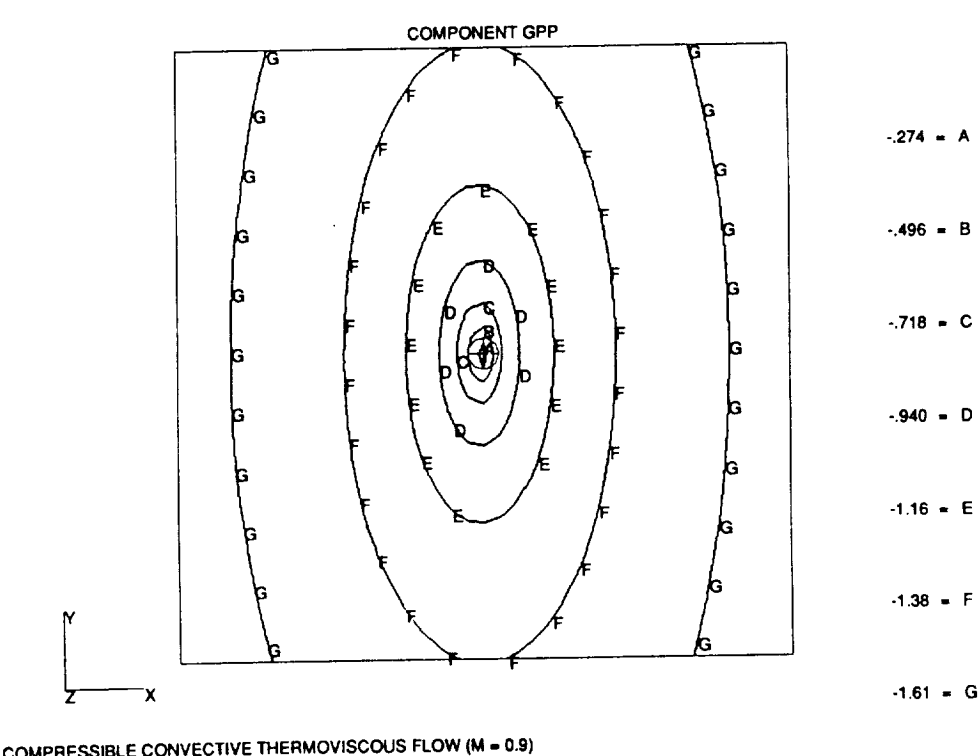


FIGURE 4.39c

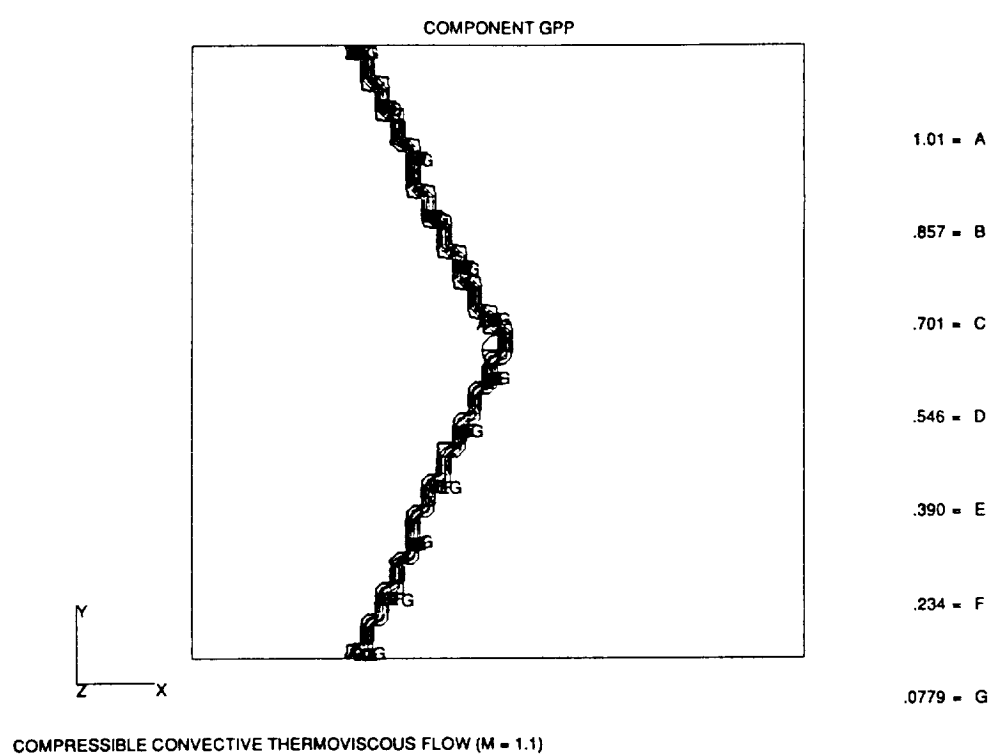


FIGURE 4.39d

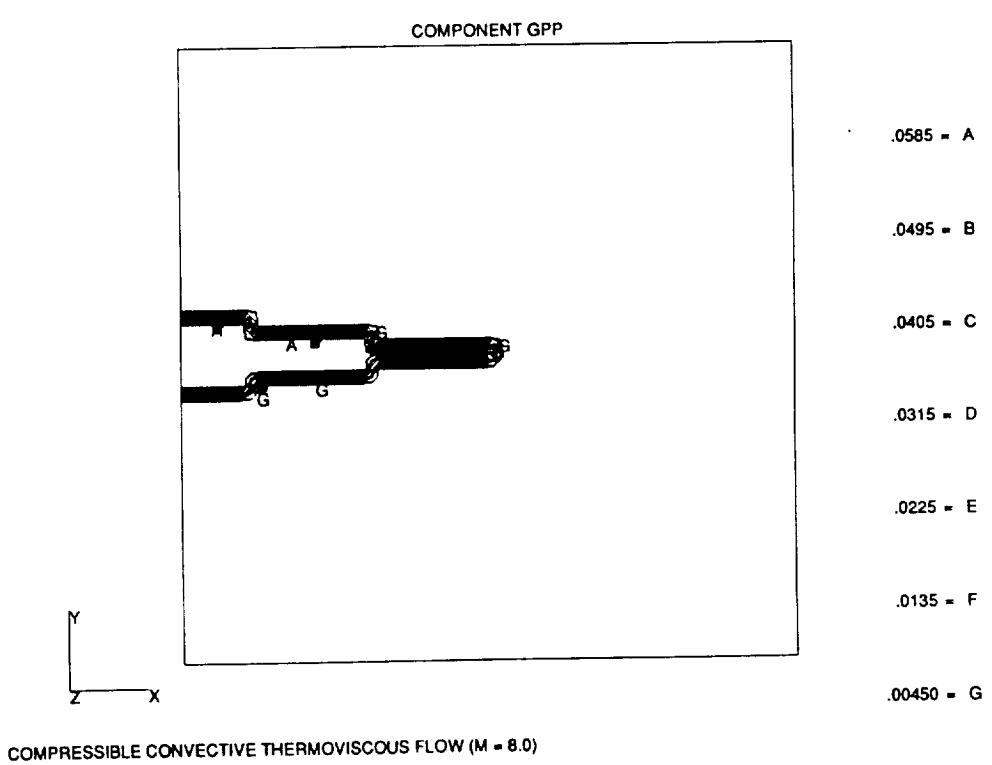


FIGURE 4.40a

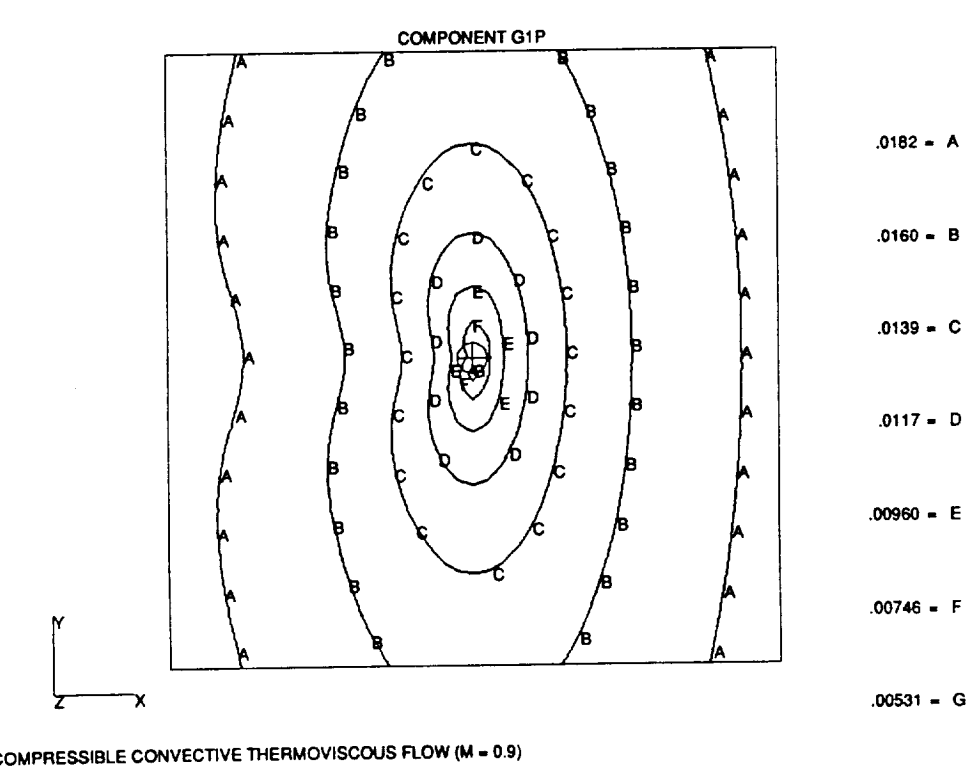


FIGURE 4.40b

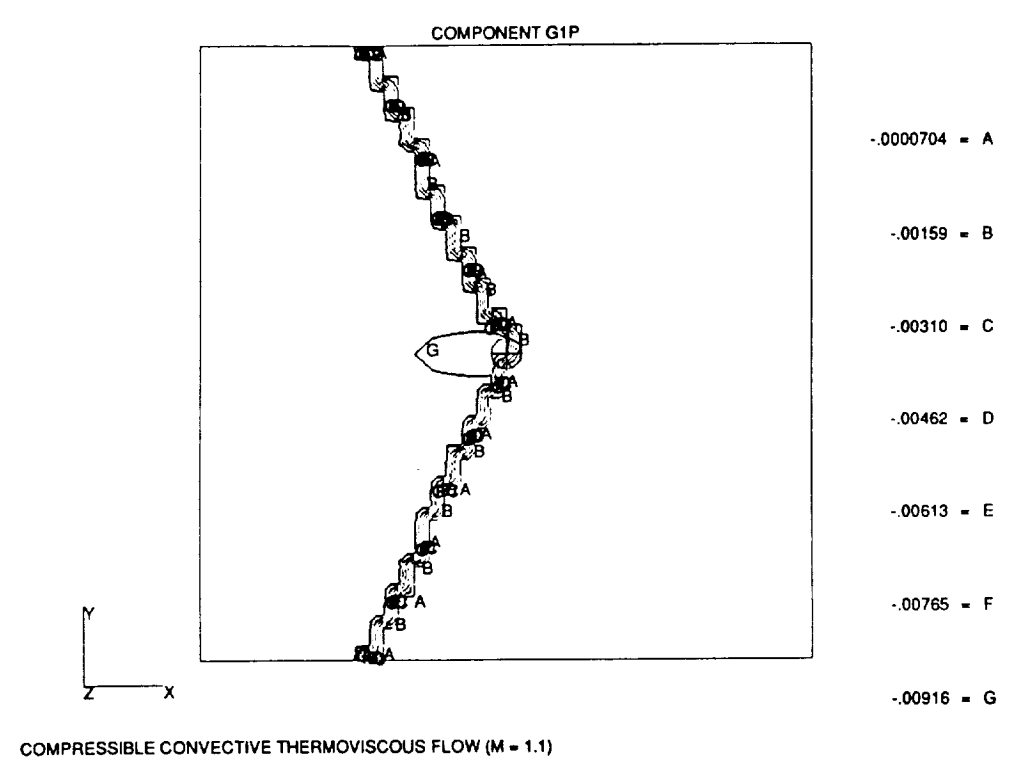
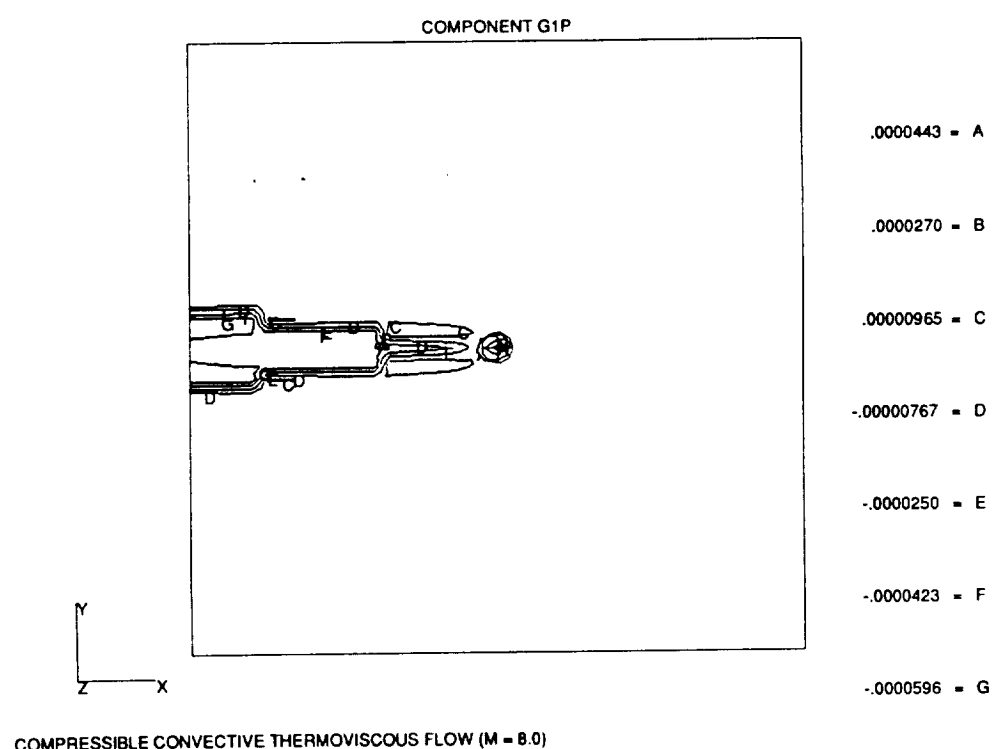


FIGURE 4.40c



5. FLUID-STRUCTURE INTERACTION

5.1 Introduction

In the previous two sections, boundary element formulations have been developed separately for a thermoelastic structural component and for a thermoviscous fluid. However, the ultimate goal of this ongoing grant is to develop a single computer program to determine the temperatures, deformation and stresses of a component exposed to a hot gas flow path, without the need for experimentally determined ambient fluid temperatures and film coefficients. While further work is still required for the fluid phase, sufficient progress has been made to demonstrate the utility of the overall concept. Consequently, in this section, problems of fluid-structure interaction will be examined.

5.2 Formulation

The Geometric Modeling Region (GMR) provides the vehicle for achieving interaction between the solid and fluid. Recall that in Section 4 different fluid formulations were employed in different GMRs. Now, some of the regions will use the thermoelastic solid boundary element model, while others utilize one of the thermoviscous fluid formulations. Compatibility must be enforced across all GMR interfaces, no matter which model is used for adjoining regions. A boundary element approach is ideal for these problems, since the integral equations are written directly on the interfacial surfaces.

For demonstration purposes, consider the problem of flow past a blade as sketched in Figure 5.1. The blade itself is labeled GMR1, and is modeled as a thermoelastic solid. A boundary mesh is all that is required for this structure. Surrounding the blade is a thin layer of cells. This is a nonlinear thermoviscous fluid region, named GMR2, in which the complete Navier-Stokes equations are solved. GMR2 is enclosed by inner and outer surfaces composed of boundary elements. The mesh utilized for the inner surface of GMR2 matches that employed for the blade in GMR1. Finally, the outer region GMR3, which extends to infinity, employs the convective Oseen kernels. The boundary element model

for GMR3 consists merely of the surface elements required to describe the interface to GMR2. Since no cells are present, the nonlinear volume and surface integrals are ignored. Thus, an approximation is introduced. However, as mentioned previously, outside of the boundary layer and wake these nonlinear contributions are negligible. (Recall that each region is the counterpart of a substructure or superelement commonly used in the finite element technology, however GMR1 and GMR3 do not require any volume discretization.)

The interface between GMR2 and GMR3 poses no particular problem. Total velocity and temperature from both regions are equated at each interface node, while the tractions and flux must be equal in magnitude but of opposite direction. The latter conditions for the compatibility of traction and flux are also true for the solid-fluid interface between GMR1 and GMR2. Total temperature must, of course, be equal on this interface as well. However, the solid integral formulations of Section 3 are written in terms of displacement, while those for fluids use velocity. Consequently, a change in variable must be introduced to ensure complete interface compatibility. For that purpose, consider the following matrix form of the integral equation for a thermoviscous fluid:

$$\begin{bmatrix} c_{ij} & 0 \\ 0 & c_{\theta\theta} \end{bmatrix}^T \begin{Bmatrix} v_i \\ \theta \end{Bmatrix} = \begin{bmatrix} G_{ij} & 0 \\ 0 & G_{\theta\theta} \end{bmatrix}^T \begin{Bmatrix} t_i \\ q \end{Bmatrix} - \begin{bmatrix} F_{ij} & 0 \\ 0 & F_{\theta\theta} \end{bmatrix}^T \begin{Bmatrix} v_i \\ \theta \end{Bmatrix} + \begin{Bmatrix} R_j \\ R_\theta \end{Bmatrix}. \quad (5.1)$$

The contributions from nonlinearities and past time steps are all contained in R_θ , as are any terms associated with the translation from perturbed velocity to total velocity v_i . Meanwhile, a similar expression written for a thermoelastic solid becomes

$$\begin{bmatrix} c_{ij} & 0 \\ 0 & c_{\theta\theta} \end{bmatrix}^T \begin{Bmatrix} u_i \\ \theta \end{Bmatrix} = \begin{bmatrix} G_{ij} & 0 \\ G_{\theta j} & G_{\theta\theta} \end{bmatrix}^T \begin{Bmatrix} t_i \\ q \end{Bmatrix} - \begin{bmatrix} F_{ij} & 0 \\ F_{\theta j} & F_{\theta\theta} \end{bmatrix}^T \begin{Bmatrix} u_i \\ \theta \end{Bmatrix} + \begin{Bmatrix} R_j \\ R_\theta \end{Bmatrix}, \quad (5.2)$$

where u_i is the total displacement. This must be rewritten in terms of total velocity v_i , where

$$v_i = \frac{\partial u_i}{\partial \tau}. \quad (5.3)$$

After invoking properties of the convolution integrals that are present in the original integral equation (3.2), the appropriate representation for the solid can be written

$$\begin{bmatrix} c_{ij} & 0 \\ 0 & c_{\theta\theta} \end{bmatrix}^T \begin{Bmatrix} v_i \\ \theta \end{Bmatrix} = \begin{bmatrix} \hat{G}_{ij} & 0 \\ \hat{G}_{\theta j} & G_{\theta\theta} \end{bmatrix}^T \begin{Bmatrix} t_i \\ q \end{Bmatrix} - \begin{bmatrix} F_{ij} & 0 \\ \hat{F}_{\theta j} & F_{\theta\theta} \end{bmatrix}^T \begin{Bmatrix} v_i \\ \theta \end{Bmatrix} + \begin{Bmatrix} \hat{R}_j \\ \hat{R}_\theta \end{Bmatrix}, \quad (5.4)$$

in which \hat{G}_{ij} , $\hat{G}_{\theta j}$ and $\hat{F}_{\theta j}$ are now modified kernel functions and \hat{R}_β is the corresponding right-hand-side contribution. However, at this point, the fluid formulation (5.1) and the solid formulation (5.4) are completely compatible, and are in an ideal form to solve quite general interaction problems.

5.3 Numerical Implementation

The boundary element code, GPBEST, was generalized so that any combination of solid and fluid regions could be accommodated. Also, the modified thermoelastic kernels of equation (5.4) were implemented. The entire GPBEST input is free format and keyword driven. Output is provided on a region-by-region basis, and thus contains only information pertinent to the region type. Displacements, temperatures, stresses and strains are detailed for solid GMRs, while velocities, temperatures, stresses, pressures, strain rates and vorticities are output for fluid regions. In all cases, a complete PATRAN interface is available, so that any quantities can be plotted.

5.4 Numerical Examples

5.4.1 Introduction

In this subsection a couple of examples will be presented to highlight the attractiveness of the present coupled boundary element approach. Flow past a thick-walled cylinder and an airfoil are considered. Both steady and transient conditions are examined, and a number of additional features of the GP-BEST implementation are explored.

5.4.2 Steady Response of a Thick Cylinder

For the first example, a thick-walled stainless steel cylinder rests under plane strain conditions in a stream of hot gas. The cylinder has an outer diameter of 1.0 in. and a thickness of 0.125 in. The inner surface of the cylinder is maintained at a temperature of 0°F, while the gas temperature in the free stream is 1000°F. The following thermoelastic properties are assumed for the solid cylinder

$$E = 29. \times 10^6 \text{ psi},$$

$$\nu = 0.30$$

$$\alpha = 9.6 \times 10^{-6} \text{ in./in.}^{\circ}\text{F}$$

$$k = 6.48 \text{ in.lb./sec.in.}^{\circ}\text{F}$$

$$\rho = 7.34 \times 10^{-4} \text{ lb.sec.}^2/\text{in.}^4 \quad c_e = 3.83 \times 10^5 \text{ in.lb.in./lb.sec.}^2\text{F.}$$

Additionally, the thermoviscous properties of the hot gas are taken as

$$\mu = 5.30 \times 10^{-9} \text{ lb.sec/in.}^2$$

$$k = 7.28 \times 10^{-3} \text{ in.lb./sec.in.}^{\circ}\text{F}$$

$$\rho = 3.69 \times 10^{-8} \text{ lb.sec.}^2/\text{in.}^4 \quad c_p = 9.49 \times 10^5 \text{ in.lb.in./lb.sec.}^2\text{F.}$$

Fluid velocities of 144 in./sec., 1440 in./sec. and 14400 in./sec., corresponding to Reynolds Numbers of 10^3 , 10^4 and 10^5 , are examined. In all cases, the hot gas flows from left to right, and only the steady response is considered.

At $Re = 1000$, the maximum temperature in the cylinder is only 98°F , and the peak compressive axial stress is 36 ksi. However, when the fluid velocity is increased to attain an $Re = 10,000$ a much more significant response is obtained. The temperature contours are shown in Figure 5.2a, the deformed shape is depicted in Figure 5.2b, and Figure 5.2c illustrates the axial stress distribution. It should be noted that in Figure 5.2b the deformation has been scaled by a factor of 100. The effects of convection are quite evident in all three diagrams. With Reynolds number increased to 100,000 these effects become even more pronounced, as seen in Figures 5.3. Now the peak metal temperature has reached 918°F .

5.4.3 Airfoil Exposed to Hot Gas Flowpath

In this final example, an NACA0018 airfoil with an internal cooling passage is exposed to the flow of a hot gas. The boundary element model for the airfoil is shown in Figure 5.4. Each dash represents an individual quadratic surface element. Throughout this problem, the outer gaseous region is modeled as a linear steady convective domain. Thus, a boundary-only exterior GMR is employed for the fluid. The hot gas at 1000°F flows

from left to right, while the inner surface of the airfoil is maintained at 200°F. Material properties from the previous example are once again used to characterize both the solid and fluid.

For the first set of investigations, the behavior of the airfoil is determined under steady-state conditions. Figure 5.5a displays the deformed shape at a Reynolds number of 1000 (based upon chord length). The solid line represents the final deformed shape, except that displacements have been scaled by a factor of twenty-five. Meanwhile, Figures 5.5b and c present the profiles of temperature and axial stress, respectively, along the upper surface of the airfoil. At this relatively slow speed flow, the airfoil is only effected near its leading edge. More significant response is shown in Figures 5.6a-c for $Re = 10,000$ and Figures 5.7a-c for $Re = 100,000$. In the latter case, the temperature at the stagnation point is nearly that of the free stream. All three cases considered so far have assumed an angle of attack of 0° with respect to the x-axis. Consequently, the response of the upper and lower surfaces is identical. Next, the angle of attack (α) is modified to 5° and 10°. Results for these cases are shown in Figures 5.8 and 5.9, respectively. Considerable asymmetry between upper and lower surfaces is now evident, although peak values of temperature and stress are essentially unaffected.

Thermal barrier coatings are often employed to reduce the metal temperatures and stresses in hot section components. The benefit of such coatings can easily be evaluated with the present boundary element formulation. Consider, for example, a coating material with thermal conductivity $k = 0.50$ in.lb./sec.in.°F sprayed to a thickness of .0095in. This is equivalent to an interfacial thermal resistance of .021 sec.in.°F/in.lb., which can be specified on the fluid-to-solid GMR interface. Results are displayed in Figure 5.10 for $Re = 100,000$ at $\alpha = 10^\circ$. Peak airfoil temperature is reduced from 976°F to 738°F by introducing this particular thermal barrier coating.

Finally, it is of considerable interest to examine the transient response of the airfoil. At time zero, the airfoil is in thermal equilibrium at a temperature of 200°F. Suddenly,

it is subjected to the hot gas stream with $Re = 100,000$ and $\alpha = 10^\circ$. The response of the upper surface at 1 msec., 2 msec., 5 msec., and 10 msec. is shown in Figures 5.11-5.14. For this transient case, the peak stress occurs slightly offset from the tip of the airfoil. Additionally, the stress σ_{yy} reaches a maximum at approximately 2 msec., while σ_{zz} and the temperature continue to climb to their steady-state values. This is true of the axial stress only because of the assumption of plane strain. In a full three-dimensional analysis, σ_{zz} would also have a higher peak during transient state.

FIGURE 5.1 - FLUID-STRUCTURE INTERACTION CONCEPTUAL MODEL

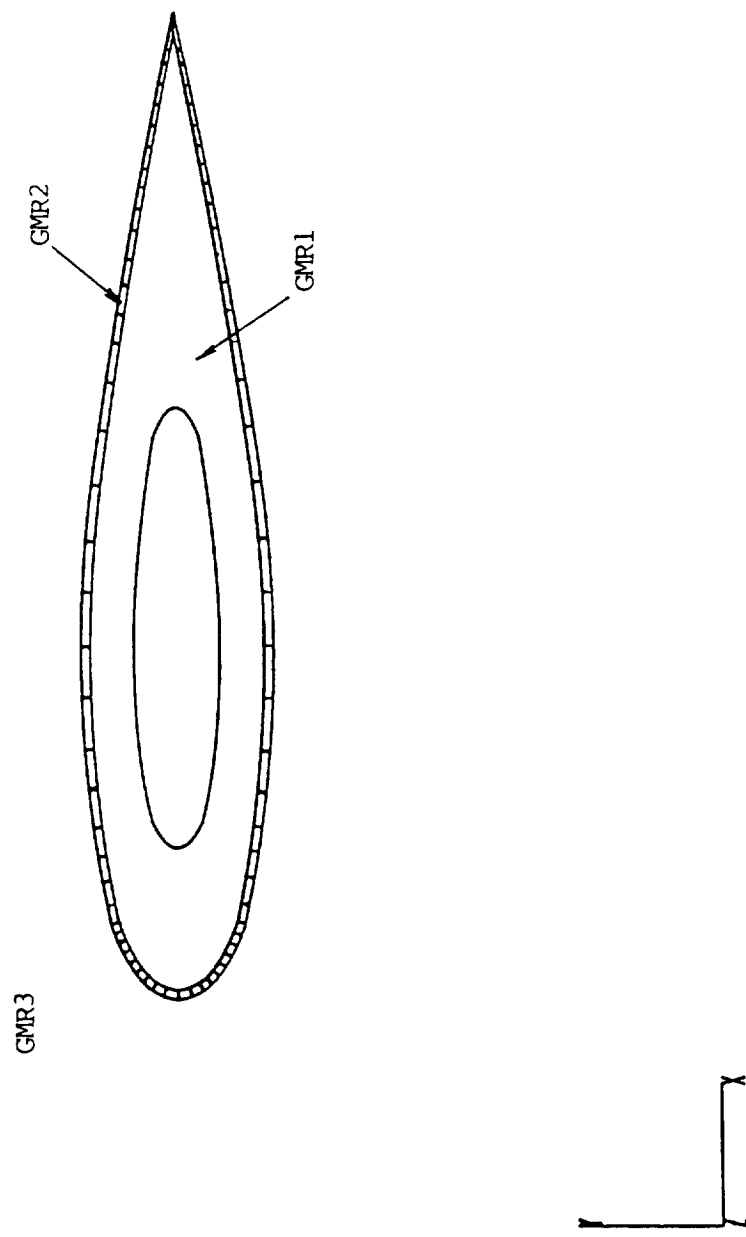
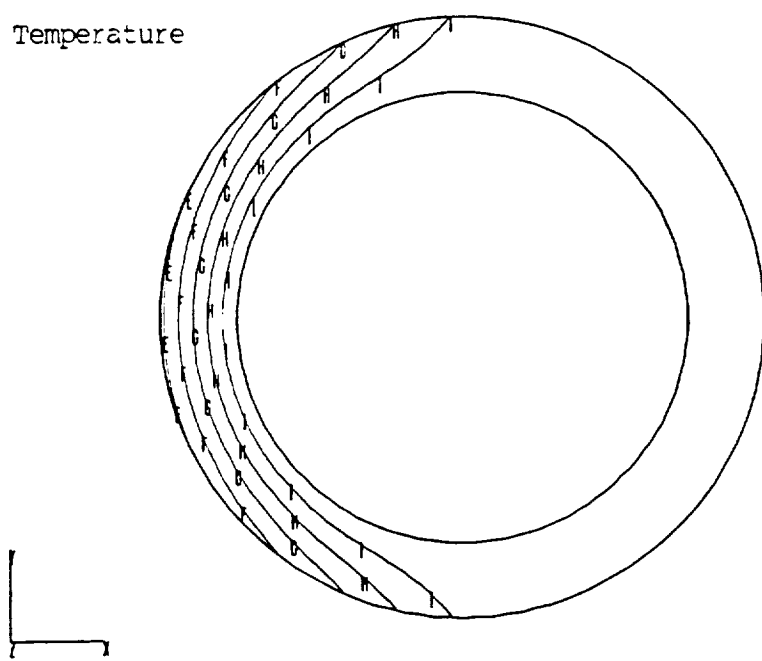


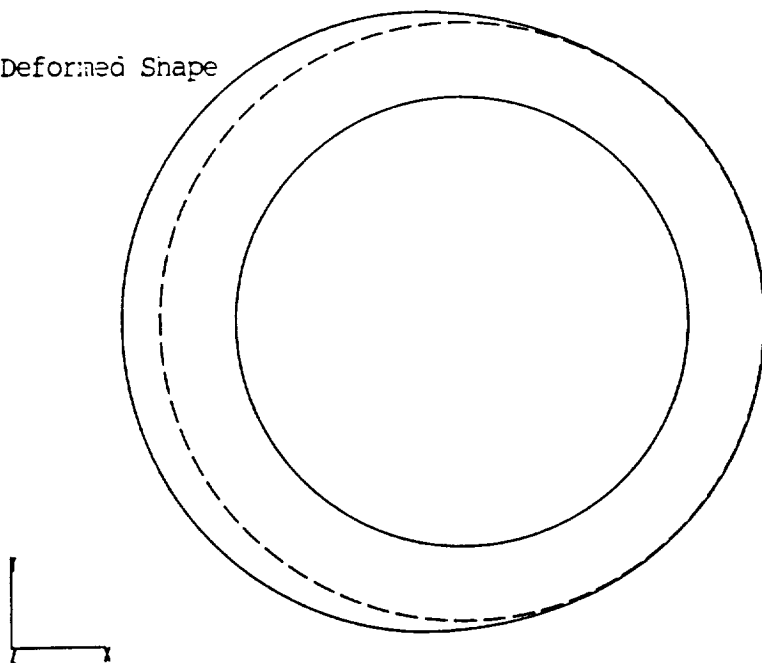
FIGURE 5.2 - STEADY RESPONSE OF A THICK CYLINDER (Re = 10,000)

a) Temperature



0SEEN FLOW AROUND A THICK CYLINDER (RE = 10000.00 - LINEAR)

b) Deformed Shape



0SEEN FLOW AROUND A THICK CYLINDER (RE = 10000.00 - LINEAR)

FIGURE 5.2 - STEADY RESPONSE OF A THICK CYLINDER ($Re = 10,000$)

c) Axial Stress

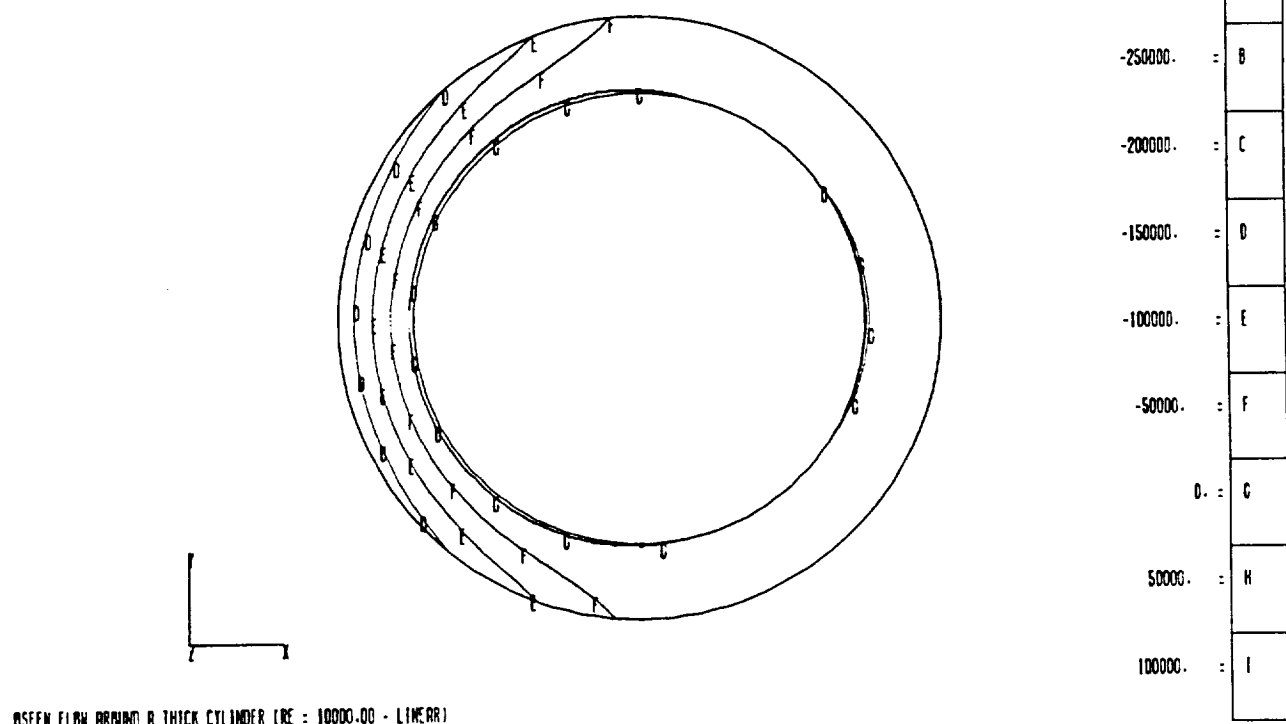
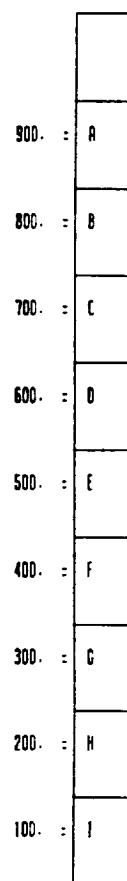
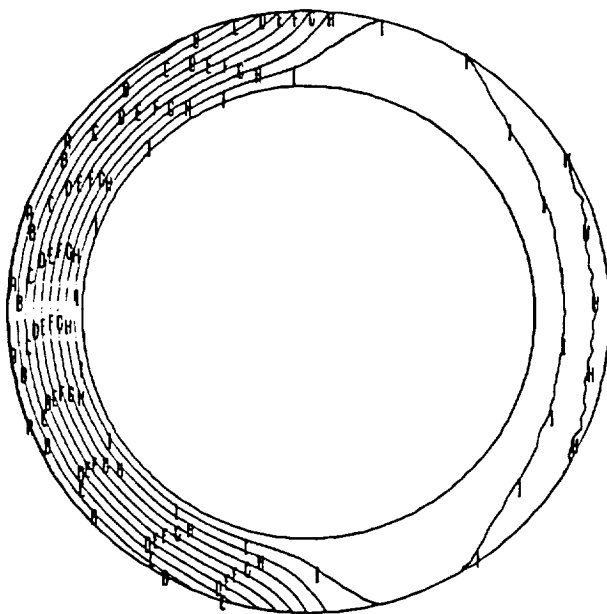


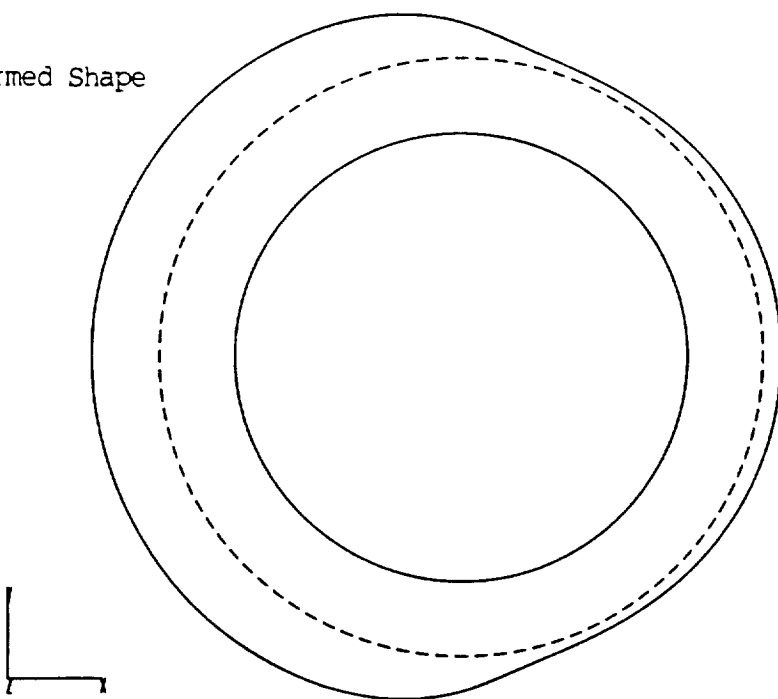
FIGURE 5.3 - STEADY RESPONSE OF A THICK CYLINDER ($Re = 100,000$)

a) Temperature



BLSEEN FLOW AROUND A THICK CYLINDER (RE = 100000.00 - LINEAR)

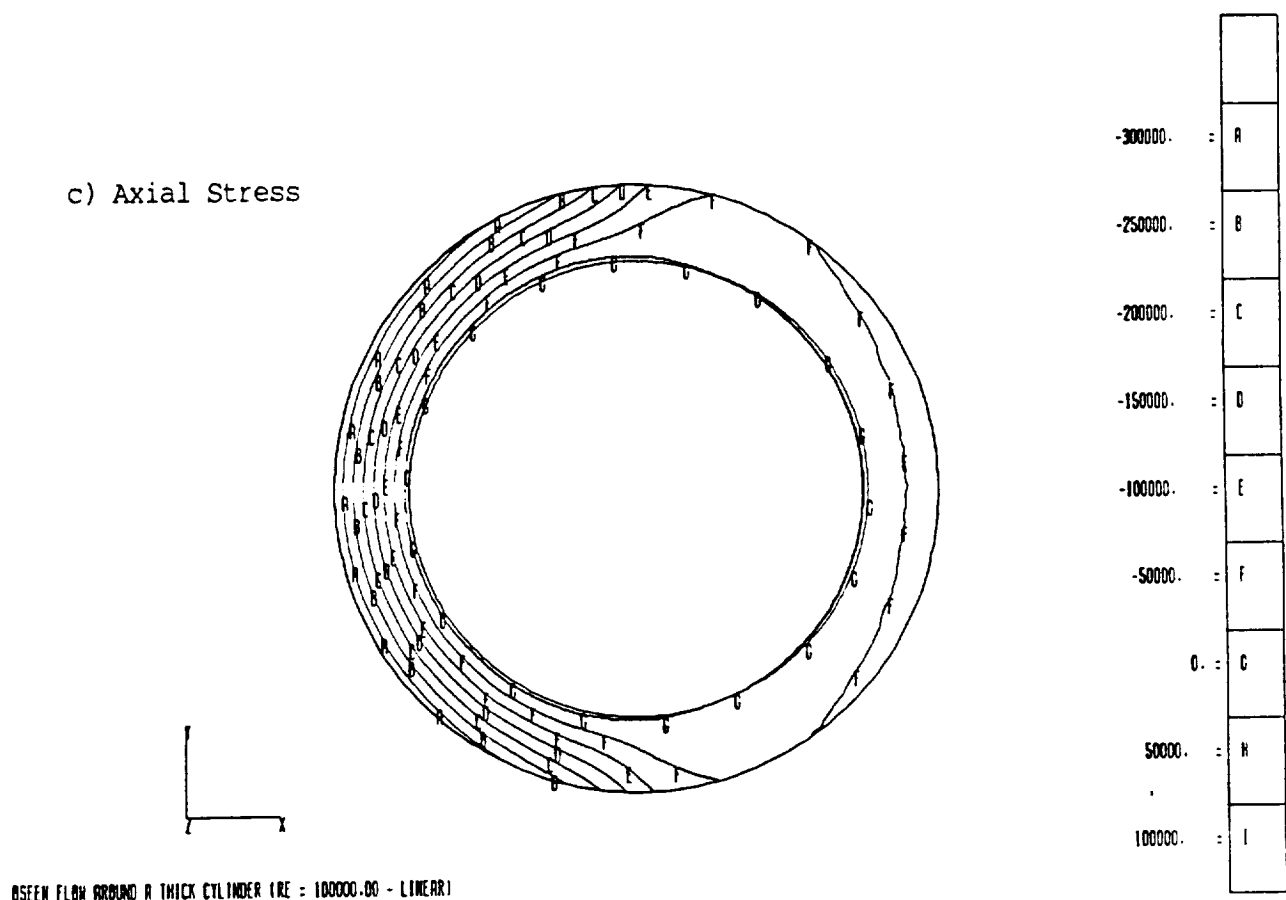
b) Deformed Shape



BLSEEN FLOW AROUND A THICK CYLINDER (RE = 100000.00 - LINEAR)

FIGURE 5.3 - STEADY RESPONSE OF A THICK CYLINDER (Re = 100,000)

c) Axial Stress



0SEEN FLOW AROUND A THICK CYLINDER (RE = 100000.00 - LINEAR)

FIGURE 5.4

AIRFOIL - BOUNDARY ELEMENT MODEL

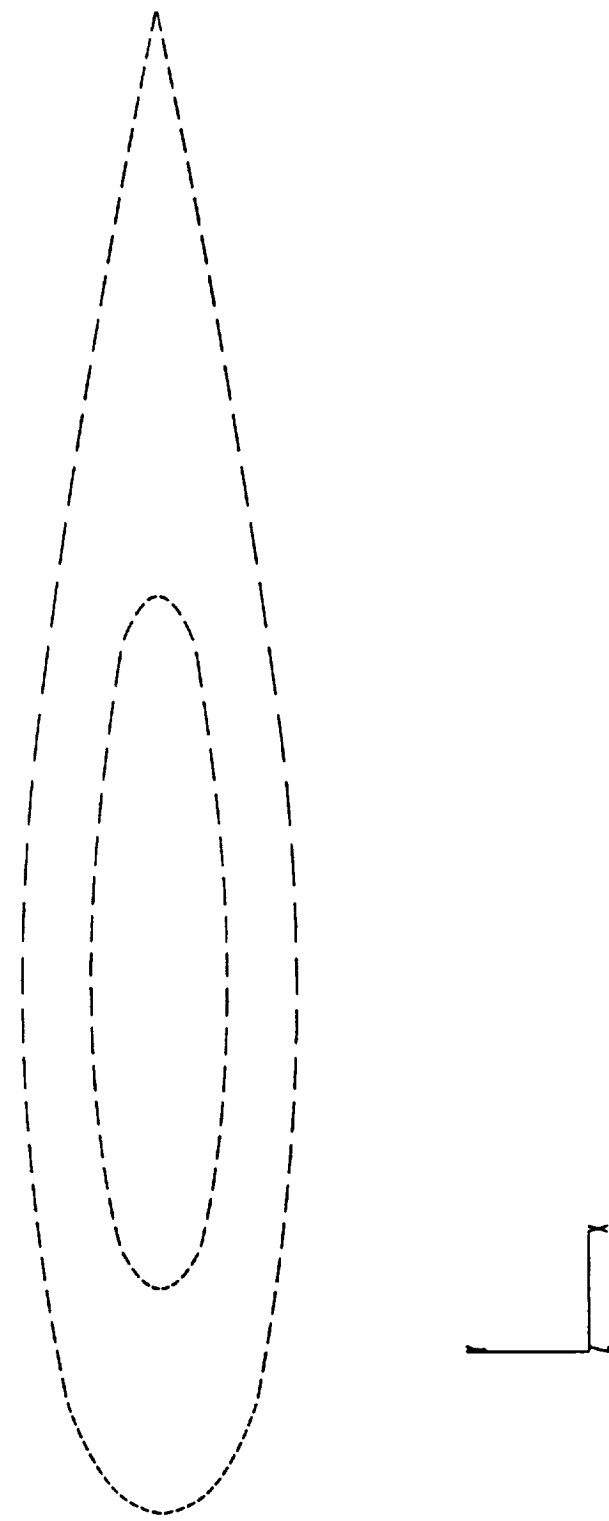
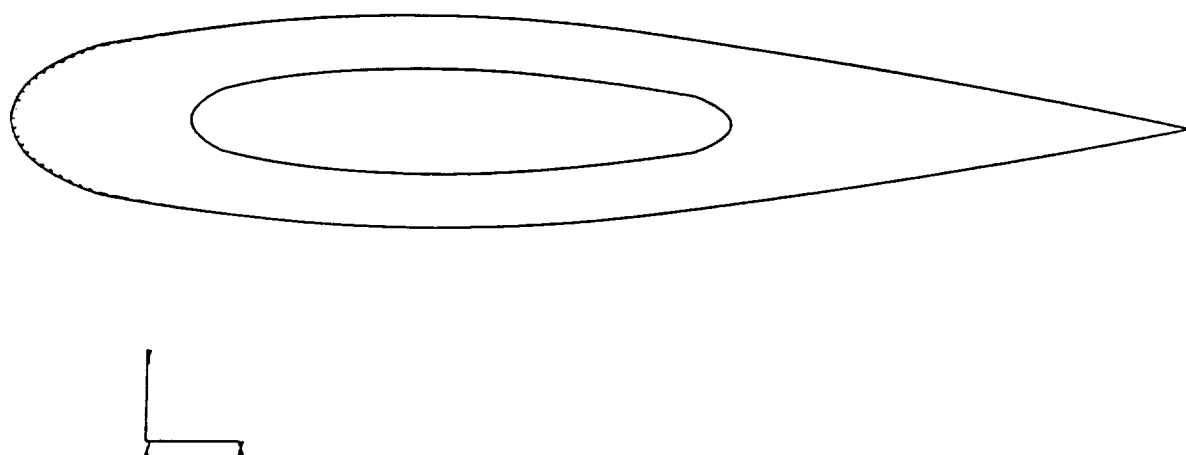


FIGURE 5.5 - AIRFOIL (STEADY; $Re = 1000$; $\alpha = 0^\circ$)



INTERNAL-COOLED NACA-0018 AIRFOIL ($Re = 1000$; ANGLE = 0)

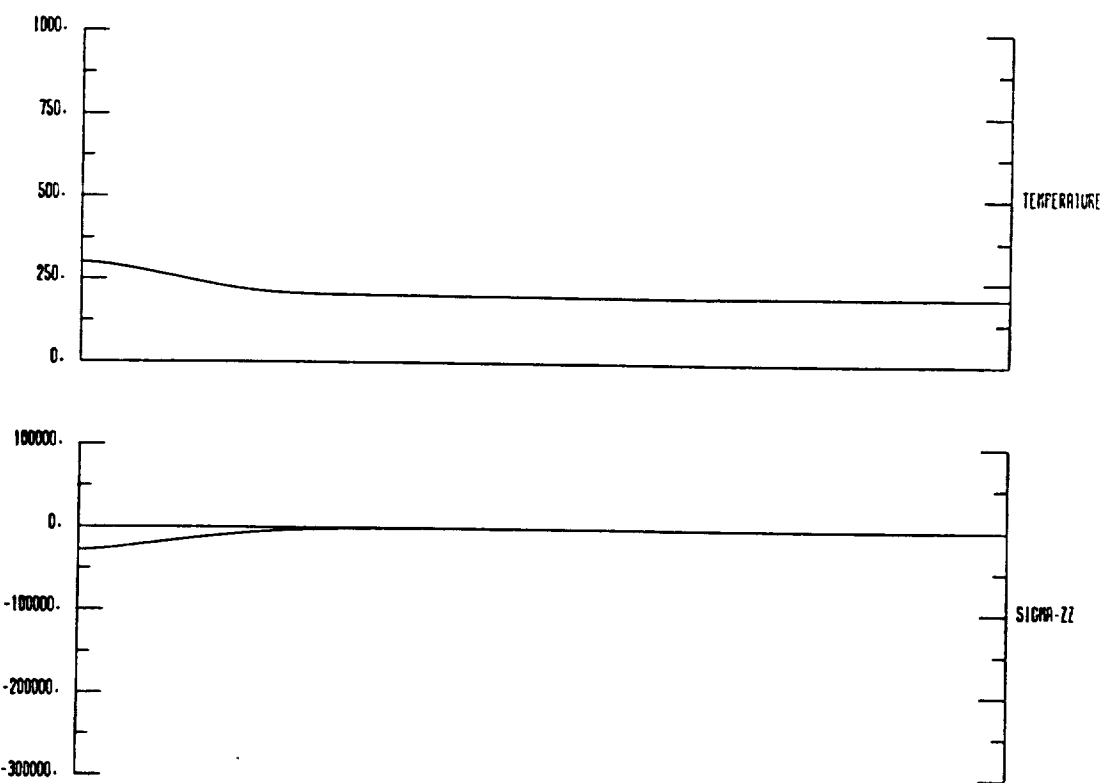
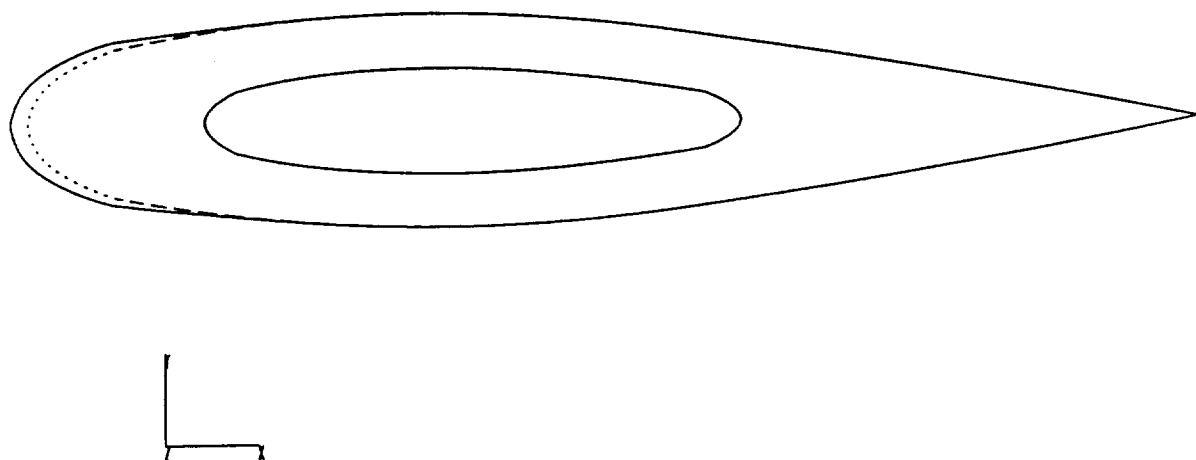


FIGURE 5.6 - AIRFOIL (STEADY; $Re = 10,000$; $\alpha = 0^\circ$)



INTERNAL-COOLED NACA-0018 AIRFOIL $Re = 10000$; ANGLE = 0

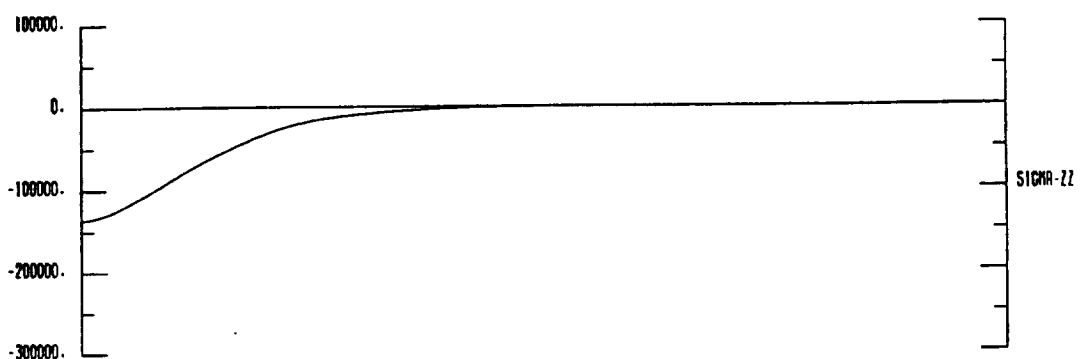
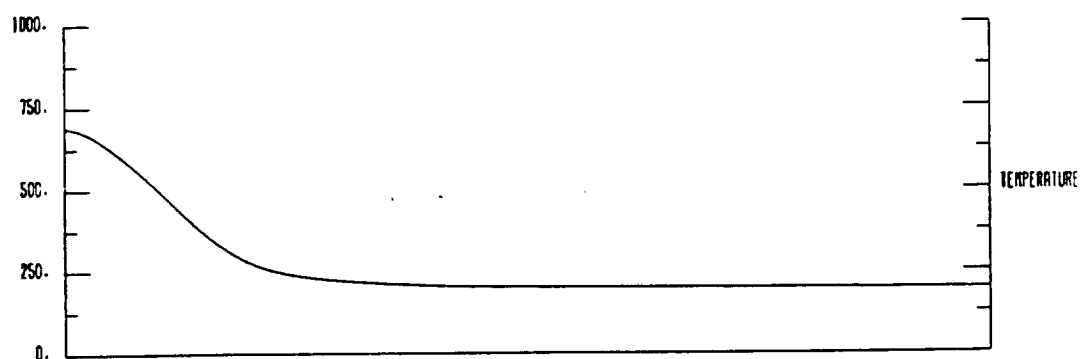
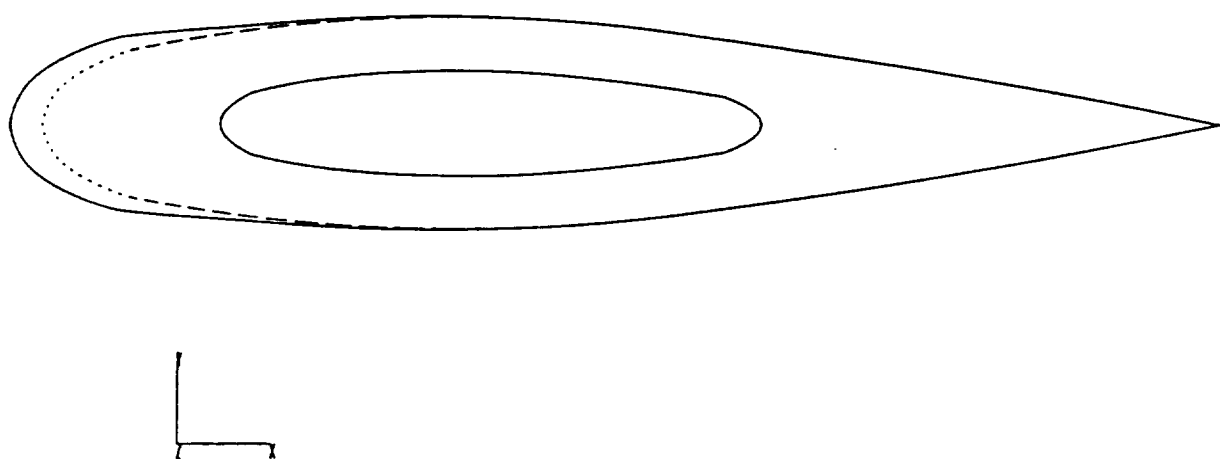


figure 5.7 - AIRFOIL (STEADY; $Re = 100,000$; $\alpha = 0^\circ$)



INTERNAL-COOLED NASA-0018 AIRFOIL (RE = 100000; ANGLE = 0)

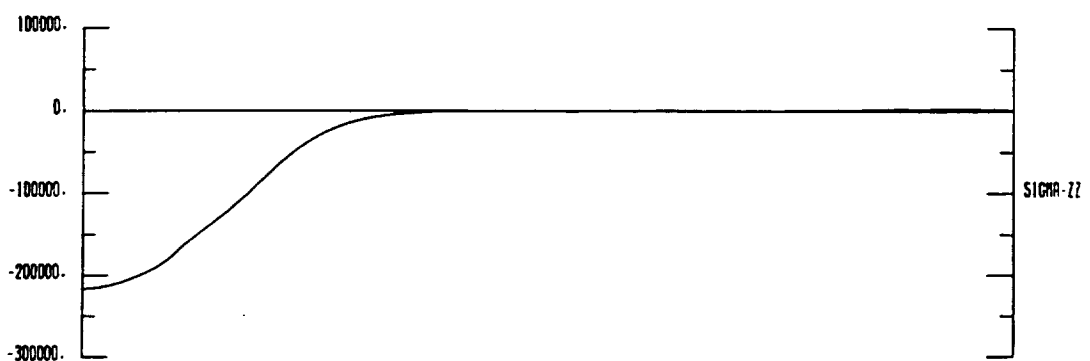
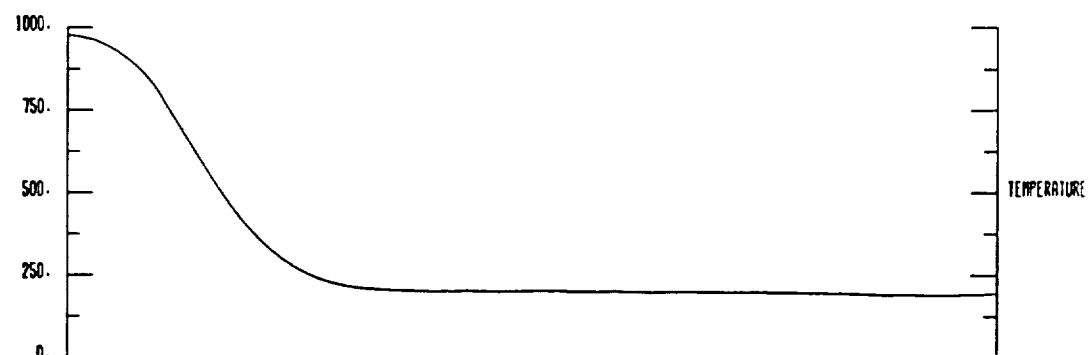
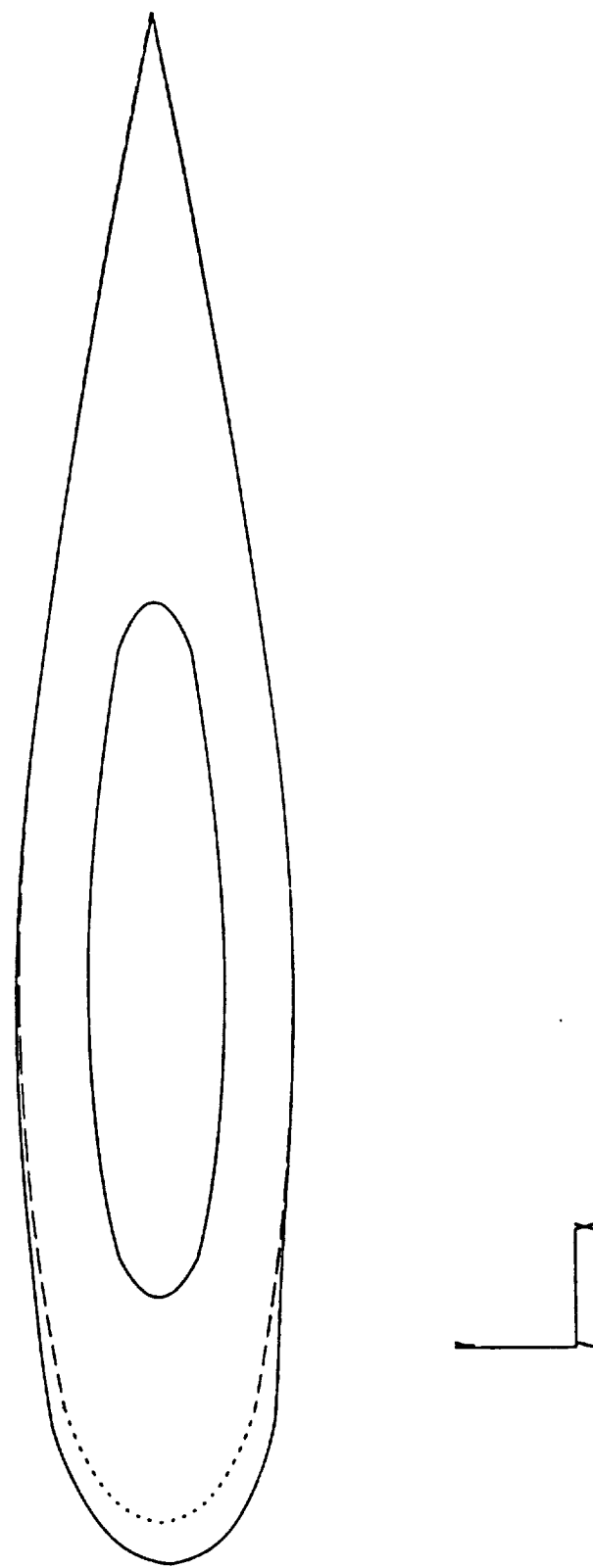


FIGURE 5.8a - AIRFOIL (STEADY; $Re = 100,000$; $\alpha = 5^\circ$)



INTERNALY-COOLED MACH-0018 AIRFOIL ($Re = 100000$; ANGLE : 5)

FIGURE 5.8b-e - AIRFOIL (STEADY; $Re = 100,000$; $\alpha = 5^\circ$)

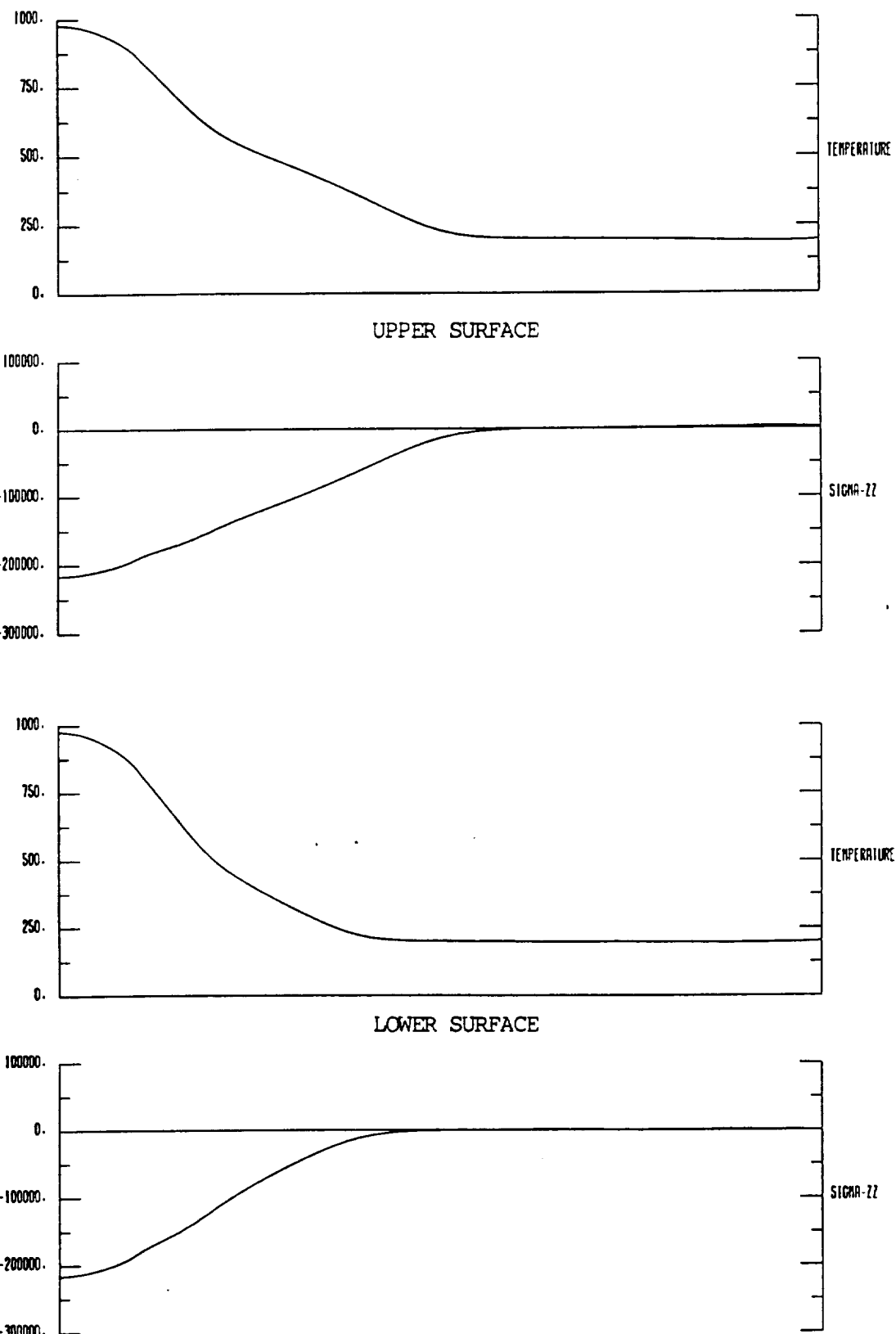
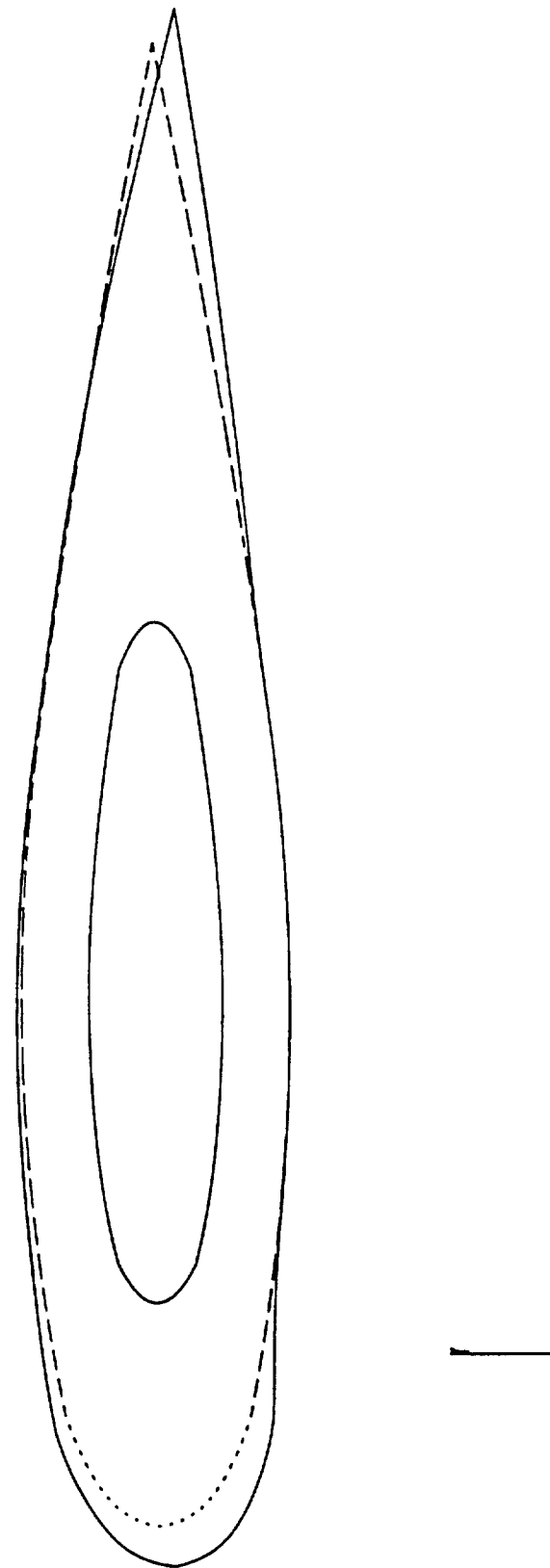


Figure 5.9a - AIRFOIL (STEADY; $Re = 100,000$; $\alpha = 10^\circ$)



INTERNALY-COULED NACA-0018 AIRFOIL ($Re = 100000$; $ANGLE = 10$)

FIGURE 5.9b-e - AIRFOIL (STEADY: $Re = 100,000$; $\alpha = 10^0$)

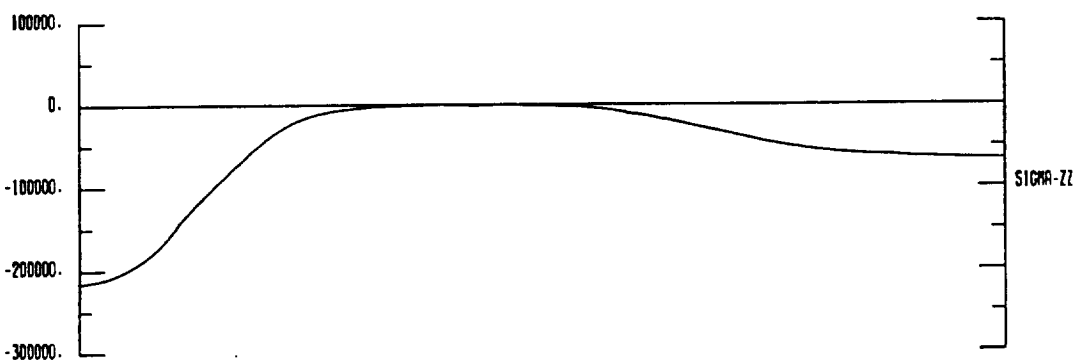
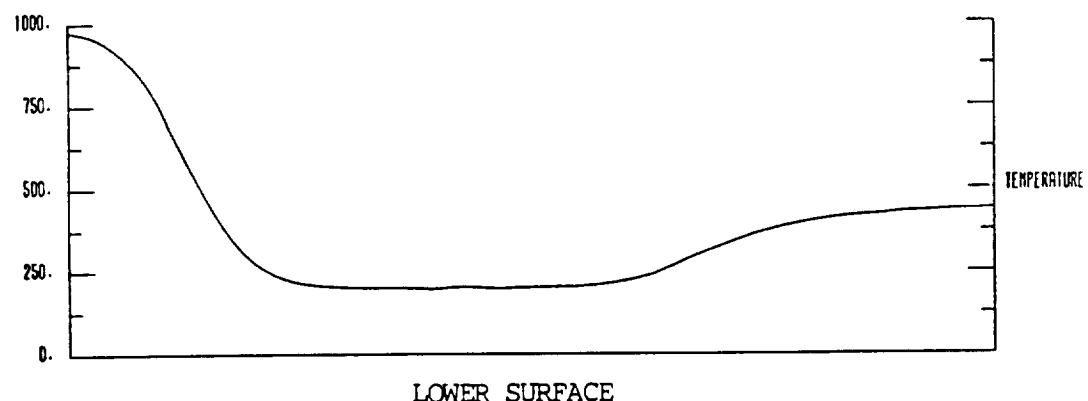
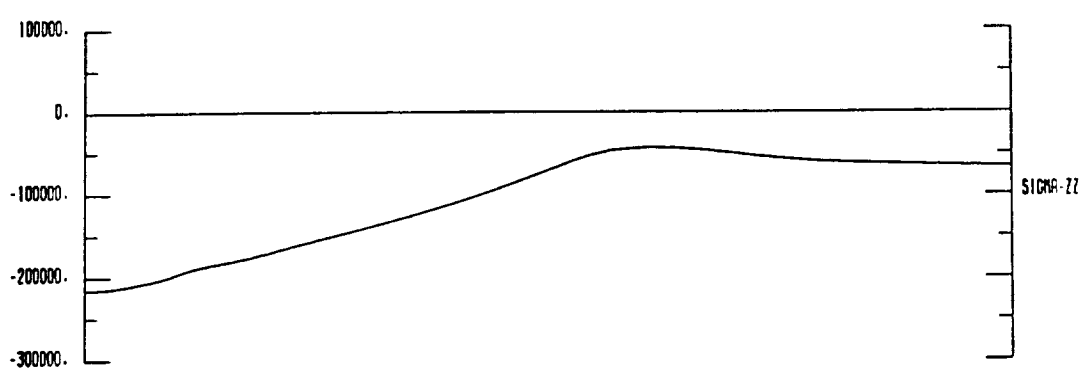
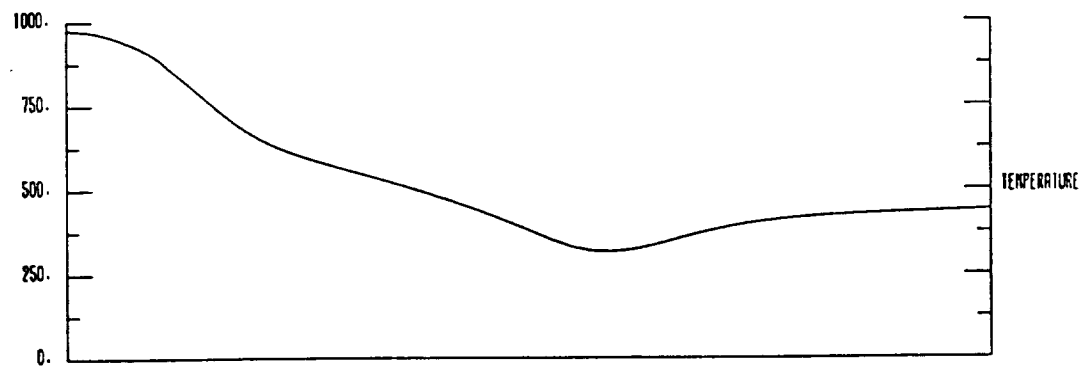


figure 5.10 - AIRFOIL WITH COATING (STEADY; $Re = 100,000$; $\alpha = 10^0$)

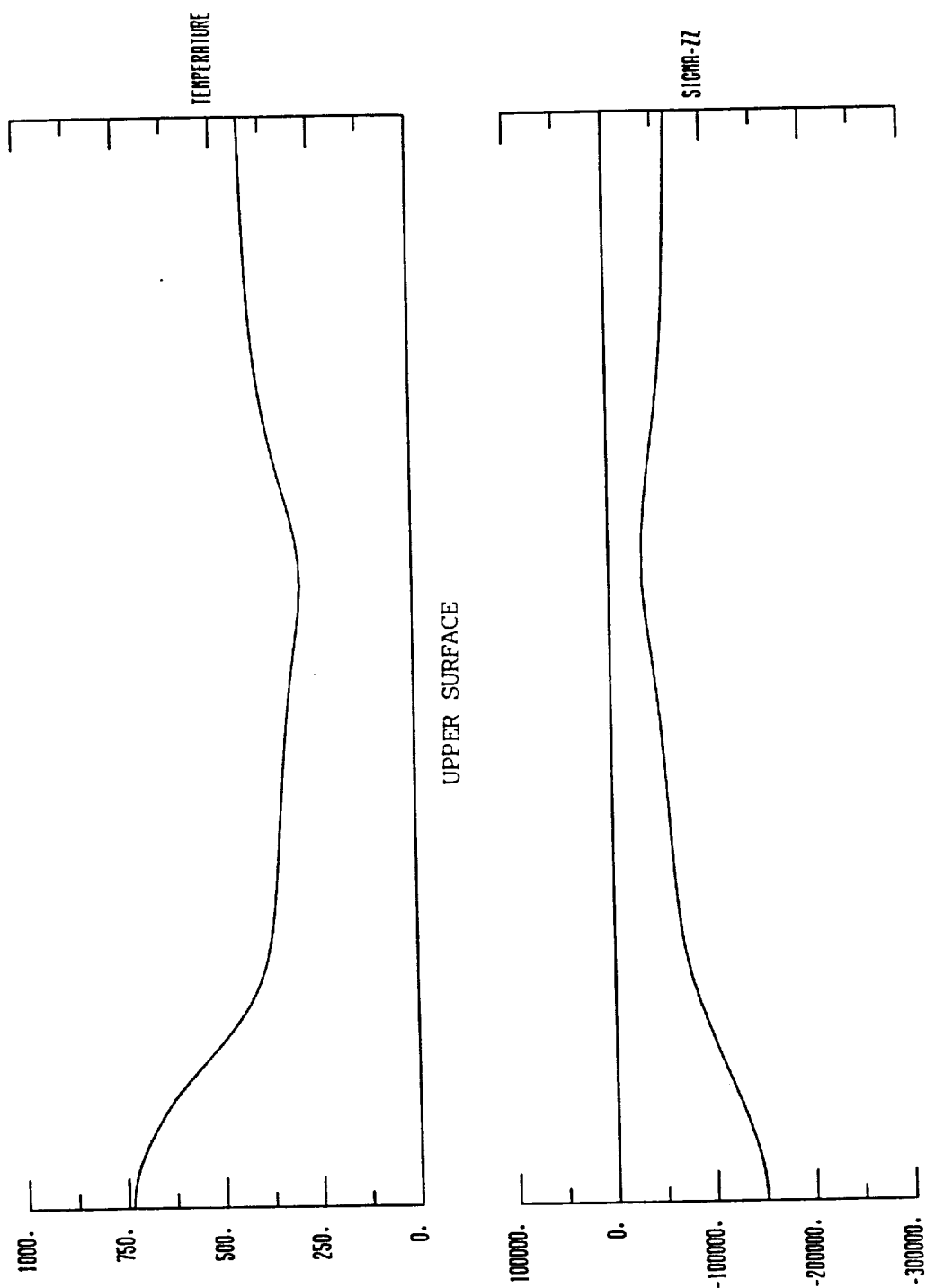


FIGURE 5.11 - AIRFOIL (TRANSIENT @ 1 msec; $Re = 100,000$; $\alpha = 10^\circ$)

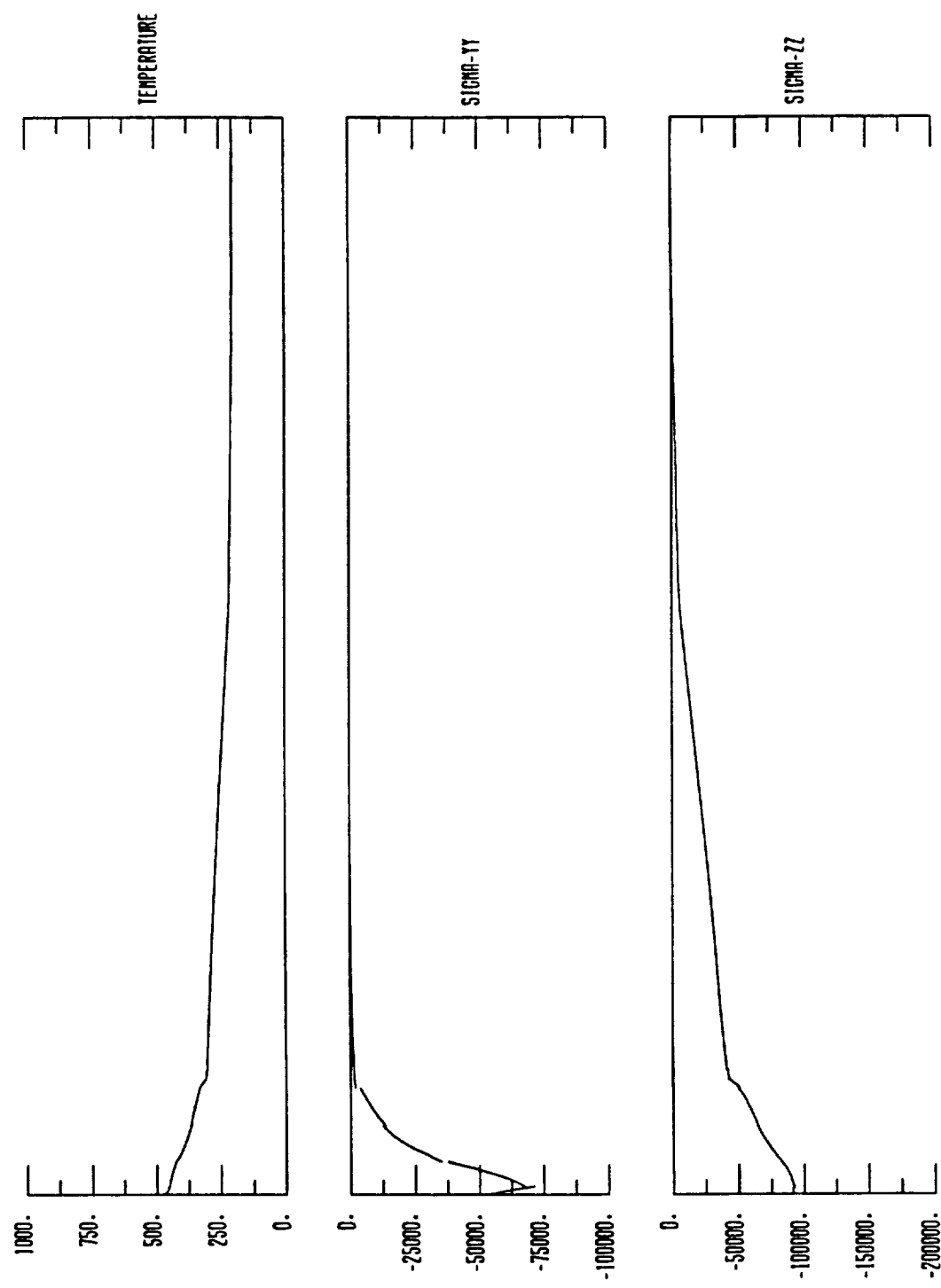


figure 5.12 - AIRFOIL (TRANSIENT @ 2 msec; $Re = 100,000$; $\alpha = 10^\circ$)

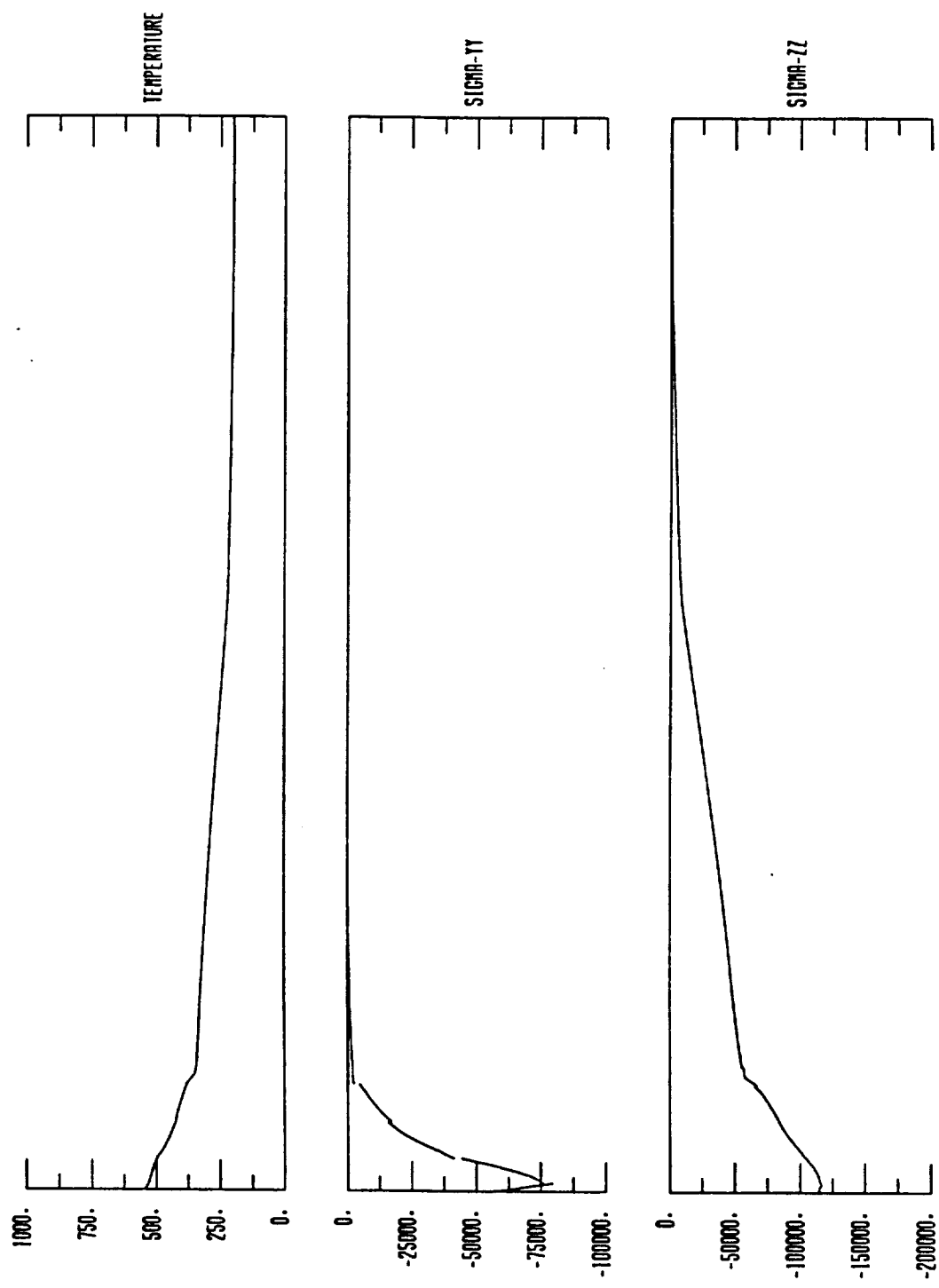
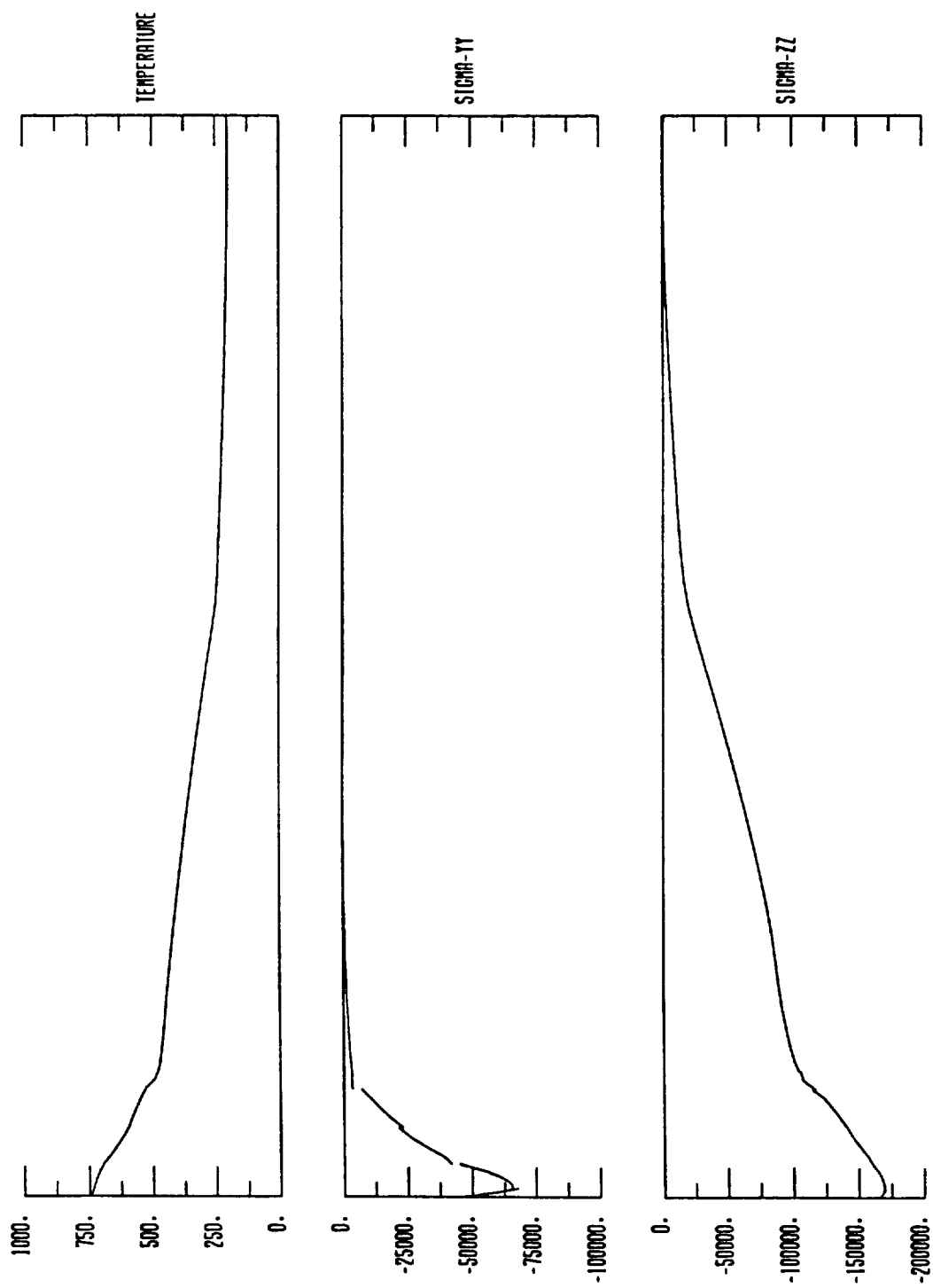


FIGURE 5.13 - AIRFOIL (TRANSIENT @ 5 msec; $Re = 100,000$; $\alpha = 10^0$)



FIGURE 5.14 - AIRFOIL (TRANSIENT @ 10msec; Re = 100,000; $\alpha = 10^0$)



6. BEM FOR RELATED PHYSICAL PHENOMENA

During the course of the investigation of the hot fluid-structure problem, a number of related technologies have been opened to analysis by the boundary element method. In this section, several of these potential applications are discussed. Most of the advancements depend upon the development of new fundamental solutions. For each case, a systematic procedure can be applied to obtain the required fundamental solution. This same procedure was developed and refined during the derivation of all of the kernel functions presented in Sections 3 and 4.

Perhaps the most interesting of these applications involve either moving sources or moving media. An example of the former kind is the determination of residual stresses in welds. As part of the NASA/HOST program, the boundary element code BEST3D was developed for the inelastic analysis of structures. Included in that code are a number of elastoplastic and viscoplastic material models that would be suitable for the weld problem. However, the temperature in the weld and adjoining structure is not known *a priori*, and a transient heat conduction analysis is required which accounts for the speed of the weld. The desired integral formulation for this thermal analysis is quite similar to that discussed for convective flow in Section 4. In addition, the fundamental solution that is needed for moving heat sources has already been derived as part of the present work. The other major advancement in boundary element technology that is required to solve the weld problem involves the development of more sophisticated nonlinear solution algorithms. It is envisioned that the modified Newton-Raphson schemes, employed for thermoviscous fluids, will provide the basis for that development. It should be noted that similar problems, such as frictional heating, grinding, and machining could also be studied utilizing the moving heat source approach.

The hot viscous fluid formulations presented in Section 4 are quite general, and consequently, applicable to a wide range of physical processes. For example, the incompressible

integral equations could be used to solve the flow problem in injection molds, or the convective formulations could be applied to investigate the cooling of electronic components. Furthermore, some relatively minor extensions would provide significant benefits. The inclusion of a buoyancy term based upon the Boussinesq approximation, would permit the examination of the thermally-induced flow in lakes or the slow heating of a room. The addition of an extra equation involving the concentration of a diffusing substance provides the opportunity to investigate the spread of pollutants in a convective environment.

As mentioned previously, once the techniques for obtaining fundamental solutions have been mastered, a wide range of physical phenomena can be analyzed via boundary element approach. Recent work by Kaynia and Banerjee (1990) has focused on the development of fundamental solutions for dynamic poroelasticity. These solutions will be utilized in a BEM (Chen, 1991) for the analysis of soil-structure interaction under seismic loading. The analogous problem of dynamic thermoelasticity, which includes the important case of thermal shock, can also be solved with the same formulation.

The coupling approach discussed in Section 5 can be used not only to solve the thermoviscous fluid-structure problem, but also to investigate flutter. In this case, frequency-dependent formulation solutions are required. The infinite space solution for periodic elastodynamics of solids is well-known (Banerjee and Butterfield, 1981), while that for a linearized Oseen fluid could be derived. The frequency domain BEM analysis would be an extension of the work done for the NASA/HOST program and contained in BEST3D.

There currently exists no satisfactory numerical nor analytical techniques to effectively deal with all of the physical phenomena mentioned in the preceding paragraphs. However, as an indirect result of the present hot fluid-structure grant, boundary element formulations and implementations are now possible for each case.

7. SUMMARY

A new methodology has been developed for hot fluid structure interaction based upon an integrated boundary element approach. As a part of this effort, significant advances have been in the analysis of both the solid and the surrounding fluid.

Section 3 detailed a boundary-only, time domain formulation for the analysis of thermoelastic solids. Not only does this approach eliminate the need for volume discretization, it also permits the accurate determination of surface temperatures and stresses which are of primary interest in hot section components. Thus, this boundary element method is a suitable substitute for finite elements for this entire class of problems. The two-dimensional formulation was presented here, however three-dimensional and axisymmetric methods have also been developed.

As mentioned previously, most of the effort expended during this research program has been directed toward the development of appropriate boundary element methods for thermoviscous fluids. This was necessary because only rudimentary formulations were available in the literature. For slow creeping flows a boundary-only method was developed for both steady-state and transient problems. In these flows, the nonlinear convective terms are negligible. As the fluid velocity is increased to moderate levels, these convective effects can no longer be ignored. Consequently, volume discretization is required and the boundary element approach based upon Stokes fundamental solutions becomes less attractive primarily due to the cost of cell integration. However, it should be noted that the resulting boundary element solutions are typically very accurate.

At higher speeds, when the convective effects dominate the entire problem, it no longer makes sense to use the viscous-based Stokes kernels. Instead, Oseen convective fundamental solutions are employed. As demonstrated in Section 4.3, those new kernels embody more of the physics of high Reynolds number flows. In fact much of the character of the problem can be captured with a linear boundary-only analysis. However, if more accuracy

is desired, volume cells can be added to the nonlinear portions of the flow field; namely, the thin boundary layer and the wake. These cells basically are used only to correct the linear solution. It is generally not necessary to capture all of the minute details of the flow in order to obtain the desired surface information, although, for example, there is no reason that turbulence models could not be introduced within the nonlinear regions.

For compressible flows, the corresponding fundamental solutions do not appear in the published literature, and, consequently, had to be developed. A new set of kernel functions, derived during this past year, were presented in Section 4.4. As shown in the diagrams, these kernels explicitly contain the hyperbolic nature of shock. Consequently, the boundary element formulations, based upon these Green's functions, will be able to model the shock front without the need for a discretization pattern. This will provide a significant advantage for the boundary element approach over any of the existing numerical techniques.

Finally, in Section 5, the boundary formulations for a thermoelastic solid were combined with those of a thermoviscous fluid to create a novel hot fluid structure interaction capability. Since integral equations are written directly on the fluid-structure interface, the BEM approach is ideally suited for this class of problems. A couple of examples were included to demonstrate the attractiveness of this method in terms of model generation and results interpretation. Additionally, it should be emphasized that all of the numerical solutions included in this report were obtained on a standard desktop SUN SPARCstation 1.

In light of all of the above developments, it must be concluded that an effective new approach has been identified for computational fluid dynamics and hot fluid-structure interaction. However, much additional effort is needed. Some of the required tasks are outlined in the next section, which defines the future direction of our research effort.

8. FUTURE DIRECTION

Despite the progress that has been made during the course of this research program, the present boundary element approach for hot fluid-structure interaction is still primarily limited by the ability to properly model and efficiently calculate the response of the surrounding fluid. The boundary element formulations for fluids are particularly attractive at the two extremes of low and high speed flows. At low velocities, the extensive boundary element technology developed for solids is directly applicable since the problems are primarily elliptic. In the intermediate range, it is quite appropriate to consider the combination of methods, with finite element or finite difference methods employed in the nonlinear regions and boundary elements for the outer linear portions of the flow field. Some attention will be given to this approach in the coming year.

However, for high speed flows, the character of the response changes. Nonlinearities are confined to the vicinity of the structure and the behavior becomes more hyperbolic. Consequently, a purely boundary element approach once again becomes most attractive. However, the necessary integration, assembly, and solver technologies have never been developed for this type of system. Instead of the standard family of volume cells, decay functions should be introduced to effectively reduce the volume integration to a surface-based computation. Furthermore, during all integration, the banded nature of the fundamental solutions should be recognized. Similarly, efficiencies can be introduced during assembly, where currently many zeroes are processed. In the solver, advantage must be taken of the nearly-sequential structure of the system equations. The implementation of these ideas would result in a very efficient method for high Reynolds number flows, particularly in a massively parallel computing environment. In fact, the fluid dynamics boundary element algorithm, including the features outlined above, is ideally suited for that environment, since it involves a large number of computationally-intensive independent processes.

Additionally, further work is needed on the implementation of the convective compress-

ible fundamental solutions, and the corresponding three-dimensional formulations must be developed. A number of planned research activities for the coming years are listed below, primarily in chronological order. Of course, the amount of progress that can be achieved in 1991 will be largely dependent on the level of funding.

Research Plan

- Development of a nonlinear boundary layer representation in terms of decay functions.
- Implementation of the new convective compressible formulation.
- Development of revamped convective integration algorithms based upon the nature of the kernels.
- Investigation of several more realistic problems of hot fluid-structure interaction.
- Incorporation of a nonlinear finite element region.
- Restructuring of the assembly routines for convective flows.
- Development and implementation of three dimensional formulations for fluid-structure interaction.
- Development of a nearly-sequential banded solver.
- Development of massively parallel computing algorithms.

APPENDIX A - References

Ahmad, S. and Banerjee, P.K. (1988), 'Transient Elastodynamic Analysis of Three Dimensional Problems by BEM,' *Int. Jour. Numerical Methods in Engineering*, Vol. 26, No. 8, pp. 1560-1580.

Banerjee, P.K., Ahmad, S. and Manolis, G.D. (1986), 'Transient Elastodynamic Analysis of Three-dimensional Problems by Boundary Element Method,' *Earthquake Engineering and Structural Dynamics*, Vol. 14, pp. 933-949.

Banerjee, P.K. and Butterfield, R. (1981), 'Boundary Element Methods in Engineering Science,' McGraw-Hill, London.

Banerjee, P.K. and Morino, L. (1990), *Boundary Element Methods in Nonlinear Fluid Dynamics, Developments in Boundary Element Methods-6*, Elsevier Applied Science, England.

Banerjee, P.K. and Raveendra, S.T. (1987), 'A New Boundary Element Formulation for Two-dimensional Elastoplastic Analysis,' *Jour. of Engrg. Mech., ASCE*, V113, No. 2, pp. 252-265.

Banerjee, P.K., Wilson, R.B. and Miller, N (1985), 'Development of a Large BEM System for Three-dimensional Inelastic Analysis,' in *Advanced Topics in Boundary Element Analysis*, ed. T.A. Cruse, A.B. Pifko and H. Armen, AMD-V72, ASME, New York.

Banerjee, P.K., Wilson, R.B. and Miller, N. (1988), 'Advanced Elastic and Inelastic Three-dimensional Analysis of Gas Turbine Engine Structures by BEM,' *Int. J. Num. Meth. Engrg.*, V26, pp. 393-411.

Banerjee, P.K., Wilson, R.B. and Raveendra, S.T. (1987), 'Advanced Applications of BEM to Three-dimensional Problems of Monotonic and Cyclic Plasticity,' *Int. Jour. Mech. Sciences*, V29, No. 9, pp. 637-653.

Batchelor, G.K. (1967), *An Introduction to Fluid Dynamics*, Cambridge University Press, Cambridge, U.K.

Boley, B.A. and Weiner, J.H. (1960), 'Theory of Thermal Stresses,' John Wiley and Sons, New York.

Burggraf, O.R. (1966), 'Analytical and Numerical Studies of the Structure of Steady Separated Flows,' *J. Fluid Mech.*, V24, Part 1, pp. 113-151.

Carslaw, H.S. and Jaeger, J.C. (1959), *Conduction of Heat in Solids*, Clarendon Press, Oxford.

Chaudouet, A. (1987), 'Three-dimensional Transient Thermoelastic Analysis by the BIE Method,' *Int. J. Num. Meth. Engrg.*, V24, pp. 25-45.

Chen, J. (1991), *Dynamic Poroelasticity Via the Boundary Element Method*, forthcoming Ph.D. Dissertation, State University of New York at Buffalo.

Cruse, T.A. (1974), 'An Improved Boundary Integral Equation Method for Three Dimensional Elastic Stress Analysis,' *Comp. and Struct.*, V4, pp. 741-754.

Cruse, T.A. and VanBuren, W. (1971), 'Three-dimensional Elastic Stress Analysis of a Fracture Specimen with an Edge Crack,' *Int. J. Fract. Mech.*, V7, pp. 1-16.

Cruse, T.A., Snow, D.W. and Wilson, R.B. (1977), 'Numerical Solutions in Axisymmetric Elasticity,' *Comp. and Struct.*, V7, pp. 445-451.

Dargush, G.F. (1987), BEM for the Analogous Problems of Thermoelasticity and Soil Consolidation, Ph.D. Dissertation, State University of New York at Buffalo.

Dargush, G.F. and Banerjee, P.K. (1988), 'Development of an Integrated BEM for Hot Fluid-Structure Interaction,' Advanced Earth-to-Orbit Propulsion Technology Conference, NASA CP-3012, Huntsville, May 1988.

Dargush, G.F. and Banerjee, P.K. (1989a), 'Development of an Integrated BEM for Hot Fluid-Structure Interaction,' International Gas Turbine and Aeroengine Congress and Exposition, ASME, Paper 89-GT-128, Toronto; also in *J. Eng. Gas Turbines and Power*, V112, pp. 243-250.

Dargush, G.F. and Banerjee, P.K. (1989b), 'Development of a Boundary Element Method for Time-dependent Planar Thermoelasticity,' *Int. J. Solids Struct.*, V25, pp. 999-1021.

Dargush, G.F. and Banerjee, P.K. (1989c), Development of an Integrated BEM Approach for Hot Fluid Structure Interaction, NASA Annual Report, Grant NAG3-712.

Dargush, G.F. and Banerjee, P.K. (1990a), 'Boundary Element Methods in Three Dimensional Thermoelasticity,' *Int. J. Solids Struct.*, V26, pp. 199-216.

Dargush, G.F. and Banerjee, P.K. (1990b), 'Time Dependent Axisymmetric Thermoelastic Boundary Element Analysis,' submitted to *Int. J. Num. Meth. Eng.*

Dargush, G.F. and Banerjee, P.K. (1990c), 'Advanced Boundary Element Methods for Steady Incompressible Thermoviscous Flow,' in *Developments in BEM-6*, ed. P.K. Banerjee and L. Morino, Elsevier Applied Science Publishers.

Dargush, G.F. and Banerjee, P.K. (1990d), 'A Time-dependent Incompressible Viscous BEM for Moderate Reynolds Number,' in *Developments in BEM-6*, ed. P.K. Banerjee and L. Morino, Elsevier Applied Science Publishers.

Dargush, G.F. and Banerjee, P.K. (1991a), 'A Boundary Element Method for Steady Incompressible Thermoviscous Flow,' to appear in *Int. J. Num. Meth. Eng.*

Dargush, G.F. and Banerjee, P.K. (1991b), 'A Time Dependent Incompressible Viscous BEM for Moderate Reynolds Numbers,' to appear in *Int. J. Num. Meth. Eng.*

Dargush, G.F., Banerjee, P.K. and Dunn, M.G. (1987), Development of an Integrated BEM Approach for Hot Fluid Structure Interaction, NASA Annual Report, Grant NAG3-712.

Dargush, G.F., Banerjee, P.K. and Honkala, K.A. (1988), Development of an Integrated BEM Approach for Hot Fluid Structure Interaction, NASA Annual Report, Grant NAG3-712.

Deb, A. and Banerjee, P.K. (1989), 'A Comparison Between Isoparametric Lagrangian Elements in 2D BEM,' *Int. J. Num. Meth. Eng.*, V28, pp. 1539-1555.

Dongarra, J.J. et al (1979), Linpak User's Guide, SIAM, Philadelphia.

Gartling, D.K., Nickell, R.E., Tanner, R.E. (1977), 'A Finite Element Convergence Study for Accelerating Flow Problems,' Int. J. Num. Methods Eng., V11, pp. 1155-1174.

Ghia, U., Ghia, K.N. and Shin, C.T. (1982), 'High-Re Solutions for Incompressible Flow Using the Navier-Stokes Equations and a Multigrid Method,' J. Comp. Physics, V48, pp. 387-411.

Gladden, H.J. (1989), 'Aerothennal Loads on Actively Cooled Components: Analyses and Experiment,' HITEMP Review, NASA Conference Publication 10039, Cleveland, Ohio, Oct. 31-Nov. 2, pp. 68.1-68.12.

Gunn, M.J. and Britto, A.M. (1984), CRISP User's and Programmer's Guide, Engineering Department, Cambridge University.

Henry, D.P. and Banerjee, P.K. (1988), 'A Variable Stiffness Type Boundary Element Formulation for Axisymmetric Elastoplastic Media,' Int. Jour. for Num. Methods in Engrg., V25, pp. 1005-1027.

Honkala, K.A. and Dargush, G.F. (1990), 'Transient Problems of Incompressible Thermo-viscous Flow via BEM,' submitted to Jour. Comp. Physics.

Kaynia, A.M. and Banerjee, P.K. (1990), 'Fundamental Solutions of Biot's Equation of Dynamic Poroelasticity,' submitted to J. Appl. Mech.

Latchat, J.C. and Watson, J.O. (1976), 'Effective Numerical Treatment of Boundary Integral Equations: A Formulation for Three-dimensional Elastostatics,' Int. J. Num. Meth. Engrg., V10, pp. 991-1005.

Millsaps, K. and Pohlhausen, K. (1953), 'Thermal Distributions in Jeffery-Hamel Flows Between Nonparallel Plane Walls,' Journal of the Aeronautical Sciences, March, pp. 187-196.

Mustoe, G.G.W. (1984), 'Advanced Integration Schemes Over Boundary Elements and Volume Cells for Two- and Three-dimensional Nonlinear Analysis,' in Developments in Boundary Element Methods - III, ed. P.K. Banerjee and S. Mukherjee, Applied Science Publishers, England.

Oseen, C.W. (1911), Über die Stokes'sche Formel und über eine verwandte Aufgabe in der Hydrodynamik II, Ark. f. mat., astr. och fysik, V7.

Oseen, C.W. (1927), Neuere Methoden und Ergebnisse in der Hydrodynamik, Akad. Verlagsellschaft, Leipzig.

Panton, R.L. (1984), Incompressible Flow, John Wiley and Sons, New York.

Piva, R. and Morino, L. (1987), 'Vector Green's Function Method for Unsteady Navier-Stokes Equations,' Meccanica, Vol. 22, pp. 76-85.

Piva, R. Graziani, G. and Morino, L. (1987) 'Boundary Integral Equation Method for Unsteady Viscous and Inviscid Flows,' IUTAM Symposium on Advanced Boundary Element Method, San Antonio, Texas.

Rizzo, F.J. and Shippy, D.J. (1977), 'An Advanced Boundary Integral Equation Method for Three-dimensional Thermoelasticity,' *Int. J. Num. Meth. Eng.* V11, pp. 1753-1768.

Schlichting, H. (1955), *Boundary Layer Theory*, McGraw-Hill, New York.

Sharp, S. and Crouch, S.L. (1986), 'Boundary Integral Methods for Thermoelasticity Problems,' *J. Appl. Mech.*, V53, pp. 298-302.

Shi, Y. (1991), *Boundary Element Methods for Compressible and Incompressible Viscous Flow*, forthcoming Ph.D. Dissertation, State University of New York at Buffalo.

Stroud, A.H. and Secrest, D. (1966), *Gaussian Quadrature Formulas*, Prentice Hall, New York.

Telles, J.C.F. (1987), 'A Self-Adaptive Co-ordinate Transformation for Efficient Numerical Evaluation of General Boundary Element Integrals,' *Int. J. Num. Meth. Engrg.*, V24, pp. 959-973.

Timoshenko, S.P. and Goodier, J.N. (1970), *Theory of Elasticity*, McGraw-Hill, New York.

Tosaka, N. and Kakuda, K. (1986), 'Numerical Solutions of Steady Incompressible Viscous Flow Problems by Integral Equation Method,' pp. 211-222 in R.P. Shaw et al, eds. *Proc. 4th Intl. Symp. Innov. Num. Methods Engrg.*, Springer, Berlin.

Tosaka, N. and Kakuda, K. (1987), 'Numerical Simulations of Laminar and Turbulent Flows by Using an Integral Equation,' *Boundary Element IX*, eds. Brebbia, Wendland and Kuhn, pp. 489-502.

Tosaka, N. and Onishi, K. (1986), 'Boundary Integral Equation Formulations for Unsteady Incompressible Viscous Fluid Flow by Time-differencing,' *Engineering Analysis*, V3, No. 2, pp. 101-104.

APPENDIX B.1 -

Kernels for Thermoelasticity

This appendix contains the detailed presentations of all the kernel functions utilized in the formulations contained in Section 3. Two-dimensional (plane strain) kernels are provided, based upon continuous source and force fundamental solutions. For time-dependent uncoupled quasistatic thermoelasticity the following relationships must be used to determine the proper form of the functions required in the boundary element discretization.

That is,

$$G_{\alpha\beta}^n(X - \xi) = G_{\alpha\beta}(X - \xi, n\Delta t) \quad \text{for } n = 1$$

$$G_{\alpha\beta}^n(x - \xi) = G_{\alpha\beta}(X - \xi, n\Delta t) - G_{\alpha\beta}(X - \xi, (n-1)\Delta t) \quad \text{for } n > 1,$$

with similar expressions holding for all the remaining kernels. In the specification of these kernels below, the arguments $(X - \xi, t)$ are assumed. The indices

i, j, k, l vary from 1 to d

α, β vary from 1 to $(d+1)$

θ equals $d+1$

where d is the dimensionality of the problem. Additionally,

x_i coordinates of integration point

ξ_i coordinates of field point

$$y_i = x_i - \xi_i \quad r^2 = y_i y_i.$$

For the displacement kernel,

$$G_{ij} = \frac{1}{8\pi} \frac{1}{\mu(1-\nu)} \left[\left(\frac{y_i y_j}{r^2} \right) - (\delta_{ij})(3-4\nu) \ln r \right]$$

$$G_{i\theta} = 0$$

$$G_{\theta j} = \frac{r}{2\pi} \left(\frac{\beta}{k(\lambda+2\mu)} \right) \left[\left(\frac{y_j}{r} \right) \bar{g}_4(\eta) \right]$$

$$G_{\theta\theta} = \frac{1}{2\pi} \left(\frac{1}{k} \right) [\bar{g}_5(\eta)]$$

whereas, for the traction kernel,

$$F_{ij} = \frac{1}{4\pi r} \frac{1}{(1-\nu)} \left[-\left(\frac{2y_i y_j y_k n_k}{r^3} \right) - \left(\frac{\delta_{ij} y_k n_k + y_i n_j}{r} \right) (1-2\nu) + \left(\frac{y_j n_i}{r} \right) (1-2\nu) \right]$$

$$F_{i\theta} = 0$$

$$F_{\theta j} = \frac{1}{4\pi} \left(\frac{\beta}{\lambda + 2\mu} \right) \left[\left(\frac{y_j y_k n_k}{r^2} \right) \bar{f}_6(\eta) - (n_j) \bar{f}_7(\eta) \right]$$

$$F_{\theta\theta} = \frac{1}{2\pi r} \left[\left(\frac{y_k n_k}{r} \right) \bar{f}_8(\eta) \right].$$

In the above,

$$\eta = \frac{r}{(ct)^{1/2}}$$

$$c = \frac{k}{\rho c_\epsilon}$$

$$E_1(z) = \int_z^\infty \frac{e^{-x}}{x} dx$$

$$\bar{h}_1(\eta) = \frac{4}{\eta^2} \left(1 - e^{-\eta^2/4} \right)$$

$$\bar{g}_4(\eta) = \frac{\bar{h}_1(\eta)}{2} + \frac{E_1\left(\frac{\eta^2}{4}\right)}{2}$$

$$\bar{g}_5(\eta) = \frac{E_1\left(\frac{\eta^2}{4}\right)}{2}$$

$$\bar{f}_6(\eta) = \bar{h}_1(\eta)$$

$$\bar{f}_7(\eta) = \frac{\bar{h}_1(\eta)}{2} + \frac{E_1\left(\frac{\eta^2}{4}\right)}{2}$$

$$\bar{f}_i(\eta) = e^{-\eta^2/4}.$$

For the interior stress kernels,

$$E_{\beta ij} = \frac{2\mu\nu}{1-2\nu} \delta_{ij} \frac{\partial G_{\beta l}}{\partial \xi_l} + \mu \left(\frac{\partial G_{\beta i}}{\partial \xi_j} + \frac{\partial G_{\beta j}}{\partial \xi_i} \right) - \beta \delta_{ij} G_{\beta\theta}$$

$$D_{\beta ij} = \frac{2\mu\nu}{1-2\nu} \delta_{ij} \frac{\partial F_{\beta l}}{\partial \xi_l} + \mu \left(\frac{\partial F_{\beta i}}{\partial \xi_j} + \frac{\partial F_{\beta j}}{\partial \xi_i} \right) - \beta \delta_{ij} F_{\beta\theta}$$

where

$$\frac{\partial G_{ij}}{\partial \xi_k} = \frac{1}{8\pi r} \frac{1}{\mu(1-\nu)} \left[\left(\frac{2y_i y_k y_k}{r^3} - \frac{\delta_{jk} y_i}{r} - \frac{\delta_{ik} y_j}{r} \right) + \left(\frac{\delta_{ij} y_k}{r} \right) (3-4\nu) \right]$$

$$\begin{aligned}
\frac{\partial G_{\theta j}}{\partial \xi_k} &= \frac{1}{4\pi} \left(\frac{\beta}{k(\lambda + 2\mu)} \right) \left[\left(\frac{y_j y_k}{r^2} \right) \{\bar{h}_1\} - (\delta_{jk}) \left\{ \frac{\bar{h}_1}{2} + \frac{E_1}{2} \right\} \right] \\
\frac{\partial F_{ij}}{\partial \xi_k} &= \frac{1}{4\pi r^2} \frac{1}{(1-\nu)} \left[- \left(\frac{4y_i y_j y_k y_l n_l}{r^4} - \frac{y_i y_j n_k}{r^2} - \frac{\delta_{jk} y_i y_l n_l}{r^2} \right. \right. \\
&\quad \left. \left. - \frac{\delta_{ik} y_j y_l n_l}{r^2} \right) \bar{f}_1(\eta) - \left(\frac{2\delta_{ij} y_k y_l n_l}{r^2} - \delta_{ij} n_k + \frac{2y_i y_k n_j}{r^2} - \delta_{ik} n_j \right) \bar{f}_2(\eta) \right. \\
&\quad \left. + \left(\frac{2y_j y_k n_i}{r^2} - \delta_{jk} n_i \right) \bar{f}_3(\eta) \right] \\
\frac{\partial F_{\theta j}}{\partial \xi_k} &= \frac{1}{4\pi r} \left(\frac{\beta}{\lambda + 2\mu} \right) \left[\left(\frac{2y_j y_k y_l n_l}{r^3} \right) \{2\bar{h}_1 - e^{-\eta^2/4}\} - \left(\frac{y_k n_j}{r} + \frac{y_j n_k}{r} + \frac{\delta_{jk} y_l n_l}{r} \right) \{\bar{h}_1\} \right].
\end{aligned}$$

$$\bar{f}_1(\eta) = 2$$

$$\bar{f}_2(\eta) = 1 - 2\nu$$

$$\bar{f}_3(\eta) = 1 - 2\nu$$

APPENDIX B.2 -

Kernels for Steady Incompressible Thermoviscous Flow

$$G_{ij} = \frac{1}{4\pi\mu} \left[\frac{y_i y_j}{r^2} - \delta_{ij} \ln r \right]$$

$$F_{ij} = -\frac{1}{2\pi r} \left[\frac{2y_i y_j y_k n_k}{r^3} \right]$$

$$\frac{\partial G_{ij}}{\partial x_k} = \frac{1}{4\pi\mu r} \left[\frac{\delta_{jk} y_i}{r} + \frac{\delta_{ik} y_j}{r} - \frac{\delta_{ij} y_k}{r} - \frac{2y_i y_j y_k}{r^3} \right]$$

$$G_{\theta\theta} = \frac{1}{2\pi k} [\ln r]$$

$$F_{\theta\theta} = \frac{1}{2\pi r} \left[\frac{y_k n_k}{r} \right]$$

$$\frac{\partial G_{\theta\theta}}{\partial x_k} = \frac{1}{2\pi k r} \left[\frac{y_k}{r} \right]$$

$$y_i = x_i - \xi_i$$

$$r^2 = y_i y_i$$

APPENDIX B.3 -

Kernels for Unsteady Incompressible Viscous Flow

$$G_{ij}(\xi - X, t) = \frac{1}{4\pi\mu} \left[\frac{y_i y_j}{r^2} \{s_1(\eta)\} - \delta_{ij} \left\{ \frac{s_1(\eta)}{2} - \frac{E_1(\frac{\eta^2}{4})}{2} \right\} \right]$$

$$F_{ij}(\xi - X, t) = \frac{1}{2\pi r} \left\{ \frac{y_j n_i}{r} \{s_1(\eta) - e^{-\eta^2/4}\} + \frac{y_i n_j}{r} \{s_1(\eta) - H(t)\} + \frac{\delta_{ij} y_k n_k}{r} \{s_1(\eta) - e^{-\eta^2/4}\} \right. \\ \left. - \frac{2y_i y_j y_k n_k}{r^3} \{2s_1(\eta) - e^{-\eta^2/4}\} \right]$$

$$\frac{\partial G_{ij}}{\partial x_k}(\xi - X, t) = \frac{1}{4\pi\mu r} \left[\frac{\delta_{jk} y_i}{r} \{s_1(\eta)\} + \frac{\delta_{ik} y_j}{r} \{s_1(\eta)\} - \frac{\delta_{ij} y_k}{r} \{2e^{-\eta^2/4} - s_1(\eta)\} \right. \\ \left. - \frac{2y_i y_j y_k n_k}{r^3} \{2s_1(\eta) - e^{-\eta^2/4}\} \right]$$

where

$$y_i = \xi_i - x_i \quad r^2 = y_i y_i$$

$$\eta = \frac{r}{(ct)^{1/2}} \quad c = \mu/\rho$$

$$s_1(\eta) = \frac{4}{\eta^2} (1 - e^{-\eta^2/4})$$

$$E_1(z) = \int_z^\infty \frac{e^{-u}}{u} du.$$

Then,

$$G_{ij}^n(\xi - X) = G_{ij}(\xi - X, n\Delta\tau) \quad \text{for } n = 1$$

$$G_{ij}^n(\xi - X) = G_{ij}(\xi - X, n\Delta\tau) - G_{ij}(\xi - X, (n-1)\Delta\tau) \quad \text{for } n > 1$$

with similar relationships for $F_{ij}^n(\xi - X)$ and $\frac{\partial G_{ij}^n}{\partial x_k}(\xi - X)$.

APPENDIX B.4 -

Kernels for Steady Convective Incompressible Viscous Flow

$$G_{ij} = \frac{1}{2\pi\mu} \left[\left(\frac{U_i U_j}{U^2} \right) e^{-\beta} K_o(\alpha) - \frac{c}{U} \left(\frac{U_i}{U} \right) \frac{\partial \phi}{\partial x_j} - \frac{c}{U} \left(\frac{U_j}{U} \right) \frac{\partial \phi}{\partial x_i} + \frac{c}{U} \left(\frac{\delta_{ij} U_\ell}{U} \right) \frac{\partial \phi}{\partial x_\ell} \right]$$

$$G_{pj} = -\frac{1}{2\pi} \left(\frac{1}{r} \right) \left(\frac{y_j}{r} \right)$$

$$F_{ij} = \mu \left(\frac{\partial G_{kj}}{\partial x_i} + \frac{\partial G_{ij}}{\partial x_k} \right) n_k + G_{pj} n_i + \rho U_k G_{ij} n_k$$

$$D_{ijk} = \frac{\partial G_{ij}}{\partial x_k} = \frac{1}{2\pi\mu} \left[- \left(\frac{U_i U_j U_k}{2c U^2} \right) e^{-\beta} K_o(\alpha) - \left(\frac{U}{2c} \right) \left(\frac{U_i U_j y_k}{U^2 r} \right) e^{-\beta} K_1(\alpha) - \left(\frac{c}{U} \right) \left(\frac{U_i}{U} \right) \frac{\partial^2 \phi}{\partial x_j \partial x_k} \right. \\ \left. - \left(\frac{c}{U} \right) \left(\frac{U_j}{U} \right) \frac{\partial^2 \phi}{\partial x_i \partial x_k} + \left(\frac{c}{U} \right) \left(\frac{\delta_{ij} U_\ell}{U} \right) \frac{\partial^2 \phi}{\partial x_\ell \partial x_k} \right]$$

where

$$y_i = x_i - \xi_i, \quad r^2 = y_i y_i$$

$$c = \frac{\mu}{\rho} \quad U^2 = U_i U_i$$

$$\beta = U_k y_k / 2c$$

$$\alpha = U r / 2c$$

$$\phi = -\ln(\alpha) - e^{-\beta} K_o(\alpha)$$

$$\frac{\partial \phi}{\partial x_i} = - \left(\frac{y_i}{r} \right) \left(\frac{1}{r} \right) + \left(\frac{U}{2c} \right) \left(\frac{y_i}{r} \right) e^{-\beta} K_1(\alpha) + \left(\frac{U_i}{2c} \right) e^{-\beta} K_o(\alpha)$$

$$\frac{\partial^2 \phi}{\partial x_i \partial x_j} = - \left(\frac{\delta_{ij}}{r^2} \right) + \left(\frac{2y_i y_j}{r^2} \right) + \left(\frac{U}{2c} \right) \left(\frac{\delta_{ij}}{r} - \frac{2y_i y_j}{r^2} - \frac{U_j y_i}{2cr} \right) e^{-\beta} K_1(\alpha) - \left(\frac{U}{2c} \right) \left(\frac{U y_i y_j}{2cr^2} \right) e^{-\beta} K_o(\alpha) \\ - \left(\frac{U_i U_j}{4c^2} \right) e^{-\beta} K_o(\alpha) - \left(\frac{U U_i}{4c^2} \right) \left(\frac{y_j}{r} \right) e^{-\beta} K_1(\alpha)$$

APPENDIX B.5 -

Kernels for Steady Convective Compressible Thermoviscous Flow

$$G_{ij} = \frac{1}{4\pi(\lambda + 2\mu)} \left\{ \delta_{ij} e^{U_k y_k / 2\eta} K_o \left(\frac{Ur}{2\eta} \right) - \frac{1}{Ur} (\delta_{ij} U_k y_k - U_i y_j - U_j y_i) \left[\frac{2\eta}{Ur} - e^{U_k y_k / 2\eta} K_1 \left(\frac{Ur}{2\eta} \right) \right] \right\} \\ + \frac{1}{4\pi\mu} \left\{ \delta_{ij} e^{U_k y_k / 2\nu} K_o \left(\frac{Ur}{2\nu} \right) + \frac{1}{Ur} (\delta_{ij} U_k y_k - U_j y_i - U_j y_i) \left[\frac{2\nu}{Ur} - e^{U_k y_k / 2\nu} K_1 \left(\frac{Ur}{2\nu} \right) \right] \right\}$$

$$G_{ip} = G_{ip}^1 + G_{ip}^2$$

$$G_{1p}^1 = -\frac{H(c-U)}{2\pi\rho_o U^2} \left[\frac{c}{v} U_1 \ln \sqrt{(U_k y_k)^2 + v^2 r^2} - U_2 \tan^{-1} \left(\frac{c U_k y_k}{v(U_1 y_2 - U_2 y_1)} \right) \right] \\ + \frac{H(U-c)}{2\rho_o U^2} \frac{c}{v} U_1 H(U_k y_k - vr)$$

$$G_{2p}^1 = -\frac{H(c-U)}{2\pi\rho_o U^2} \left[\frac{c}{v} U_2 \ln \sqrt{(U_k y_k)^2 + v^2 r^2} - U_1 \tan^{-1} \left(\frac{c U_k y_k}{v(U_1 y_1 - U_2 y_2)} \right) \right] \\ + \frac{H(U-c)}{2\rho_o U^2} \frac{c}{v} U_2 H(U_k y_k - vr)$$

$$G_{ip}^2 = -\frac{1}{2\pi\rho_o U^2} \left[U_i e^{U_k y_k / 2\eta} K_o \left(\frac{Ur}{2\eta} \right) + \frac{1}{Ur} (U_i y_k y_k - U^2 y_i) \int_{Ur/2\eta}^{\infty} e^{U_k y_k \xi / Ur} K_o(\xi) d\xi \right]$$

$$G_{pp} = \frac{H(c-U)}{2\pi} \left[\frac{c}{v} \ln \sqrt{(U_k y_k)^2 + v^2 r^2} - \eta \frac{U_k y_k}{(U_k y_k)^2 + v^2 r^2} \right] - \frac{1}{2} H(U-c) \frac{c}{v} H(U_k y_k - vr)$$

$$G_{\theta\theta} = \frac{1}{2\pi k} e^{U_k y_k / 2\kappa} K_o \left(\frac{Ur}{2\kappa} \right)$$

$$\eta = (\lambda + 2\mu)/\rho_o, \quad \nu = \mu/\rho_o, \quad \kappa = k/\rho_o c_v$$

$$v^2 = |c^2 - U^2|$$